Surface structure enhanced microchannel flow boiling of low surface tension fluids

by

Jay Sircar

Submitted to the
Department of Mechanical Engineering
in Partial Fulfillment of the Requirements for the Degree of

Doctor of Philosophy in Mechanical Engineering

at the

Massachusetts Institute of Technology

June 2021

Signature of Author: _____

<div align="right">

Department of Mechanical Engineering
May 14, 2021

</div>

Certified by: _____

<div align="right">

Evelyn N. Wang
Department Head; Gail E. Kendall Professor
Thesis Supervisor

</div>

Accepted by: _____

<div align="right">

Nicolas Hadjiconstantinou
Professor of Mechanical Engineering
Graduate Officer

</div>

Surface structure enhanced microchannel flow boiling of low surface tension fluids

by

Jay D. Sircar

Abstract

Microchannel flow boiling can meet the thermal management requirements of high power and high frequency integrated circuits, but the technology has been limited by the instabilities unique to their length scales. During microchannel flow boiling of water, many of these instabilities have been successfully mitigated by the addition of surface microstructures. Thermohydraulic performance in terms of critical heat flux (CHF) and heat transfer coefficient (HTC) have also benefited from surface modification, without significantly adding to the overall flow pressure drop. For some microelectronic applications, water may not be the ideal fluid for microchannel flow boiling, such as in aerospace engineering where thermal management solutions must operate over a wide range of temperatures from subzero Celsius to optimal semiconductor temperatures. Alternatives to water as a working fluid include methanol, which has one of the largest ranges of operating temperatures suitable for electronics cooling, and hydrofluoroether (HFE) 7000, an environmentally friendly dielectric fluid. Though there are benefits to using these alternative working fluids, several of their thermophysical properties involved in generating capillary flows are significantly less than that of water—most notably their surface tensions. Prior studies have shown that the level of enhancement to the critical heat flux during the flow boiling of water, was positively correlated with the capillary-limited thin-film dryout heat flux. The same semi-analytical model suggested that thin-film dryout would occur at approximately one and two orders of magnitude smaller heat fluxes when switching from water to methanol and HFE 7000, respectively.

In this thesis, thermohydraulic changes from surface microstructures during intrachip flow boiling of lower surface tension working fluids, primarily methanol, was investigated. We fabricated microchannels on the heated bottom wall of silicon test samples, with/without micropillars of two different heights (25 and 75 µm) and two different cylindrical pillar solid fractions (~ 5% and 20%). For methanol, a maximum CHF of 494 W/cm^2 was achieved with a structured surface, a 61% enhancement compared to smooth surface. At higher heat fluxes, the maximum HTC increased by as much as 71%, to 271 kW/m^{2}K, for the taller, sparser micropillar wicked channels compared to smooth microchannels. The presence of micropillars reduced the HTC or resulted in no significant change at lower exit quality conditions. The CHF enhancement among different geometries of wicks did not fully agree with the fluid wicking model, suggesting that capillarity may not be the dominant factor contributing to the enhanced performance. Annular films of methanol within smooth microchannels near CHF abruptly dewet from bulk of the heated wall, and resulted in inverted annular (film) flow boiling or transition boiling. High speed imaging coupled with hydraulic and thermal measurements, showed that the taller micropillars prevented this liquid film rupture. The importance of hydrodynamic effects resulting from the micropillar wick arrays was supported by force scaling analysis and finite element analysis. Observed experimental flow boiling behaviors near CHF for water, methanol, and HFE 7000, revealed that as surface tension decreased, the effectiveness of micropillar wicks in preventing the rupture and removal of annular films dwindled. Heat dissipation approaching 0.5 kW/cm^2 at a calculated wall superheat of less than 20 K during flow boiling of methanol in microstructured channels was achieved, suggesting that this can be a promising cooling strategy for high power-density electronic systems operating in challenging environments. Insights gained from this work will lead to the development of new design principles that will allow for even lower surface tension fluids, *e.g.* fluorinated dielectrics, to be used as working fluids and maximize their potential during flow boiling.

Acknowledgements

I would like to thank my wonderful adviser Prof. Evelyn Wang for her advice, guidance, and for being a great mentor. I could not have achieved what I have without her help and support. I would like to thank my excellent thesis committee members Prof. Jacopo Buongiorno, Prof. Rohit Karnik and Prof. Sameer R. Rao. They provided invaluable advice, asked insightful questions that made me think outside the box, and helped me reach this milestone. I would like to thank the entire Device Research Lab - graduate students, post-docs, alumni, and collaborators who were tremendously helpful in stimulating my development as an engineer and a researcher. In particular, I am grateful to Dr. Daniel Hanks, a great friend who provided valuable guidance. He set me on my path of thermal management research back when I was an undergraduate researcher (UROP). His encouragement, support, ingenuity, and dedication helped me in my work. I would also like to thank my friend Dr. Dion Antao for his helpful and insightful suggestions. The excellent staff of the Microsystems Technology Laboratories offered valuable technical guidance and training for this project. Thanks are also due to Dennis Ward, Kurt Broderick, Donal Jamieson, Jorg Scholvin, Jim Daly, Robert Bicchieri, Eric Lim, Kristofor Payer, and Dr. Vicky Diadiuk for their immense patience and suggestions when technical challenges arose during the fabrication process. I wish to acknowledge the Office of Naval Research for funding this research project - Nanoengineered Surfaces for High Flux Thin Film Evaporation (N000140-91-10-0-0) and Dr. Mark Specter, the Program Manager. Thanks to all the life-long friends I made while at MIT. My heartfelt thanks go to my sister Monica, for being there for me every step of the way - quietly leaving food for me at the front desk when no visitors were allowed inside the dorm building, helping with grocery shopping, and all the fun things we did before the pandemic hit. Finally, thank you to my parents for everything that helped me to get to where I am today. I wish to dedicate this thesis to the person who would have been proudest of my achievement - my grandmother the late Mrs. Anjali Bose Roy Chowdhury, whom I miss dearly.

Contents

List of Figures

Chapter 5

Chapter 6

List of Tables

Nomenclature

A	area, cm^2		**Greek symbols**	
P	pressure, MPa		α	permeability, 1/m^2
T	temperature, ℃ or K		γ	scaling factor, -
c_p	specific heat, J/kg·K		η_f	fin efficiency, -
d	diameter, μm		μ	viscosity, Pa·s
h	heat transfer coefficient, W/cm^{2}K		ϕ	porosity, -
k	thermal conductivity, W/m·K			
l	length, μm		**Subscript**	
m	mass flow rate, kg/s		c	capillary
q''	heat flux, W/m^2		i	interface
r	radius, nm		l	liquid
t	thickness, μm		l	liquid channel
w	width, μm		m	membrane
			p	pore
			r	Ridge
			rc	ridge channel
			v	vapor
			∞	far-field, bulk

Chapter 1- Introduction

1.1   Thermal Management Bottleneck for Electronics

Over the past several decades, electronic devices have undergone incredible miniaturization with increased power density, and in keeping pace with this development, has been the necessity to keep them cool. Keeping electronic devices cool to maintain their longevity and long-term reliability, has been the focus of intense investigation [1]. Cutting edge and next generation integrated circuits (ICs) have increased power densities and temperature gradients necessitating thermal management solutions that are radically innovative.

Wide band-gap semiconductors, smaller linewidths features, thinner substrates, and higher dimensional architectures have allowed for continued device compaction as well as enhanced energy generation density [1], [2]. Semiconductors, such as silicon carbide (SiC) and gallium nitride (GaN), have increased thermal conductivity, higher breakdown voltages, and lower on-state resistances [3]. Devices on these semiconductors can sustainably operate at higher temperatures and voltages. Improved material properties, like those of GaN components in high electron mobility transistors (HEMT), allow for higher operating efficiencies. For high frequency/high power applications, including wireless communications and radar, GaN devices have improved performance—faster clock speed and increased sensitivity, while being smaller and requiring up to 90% less power [4].

Moore's Law which quite accurately predicted the exponential increase in transistor packing for four decades, has resulted in increased computational power [2]. Having nearly reached the limits of resolvable linewidths for components, recent computational performance improvements have taken advantage of multiple cores for parallel processing and architectures that integrate discrete semiconductor devices into a single system-on-chip. Next generation improvements will go even further with three-dimensional (3D) architectures that shorten interconnect lengths through vertical integration in order to increase computation

speeds and power efficiencies. Compaction at this scale can quickly increase the power densities by several orders of magnitude and magnify thermal gradients across devices, as overall power efficiencies improve [4]. 3D stacked devices heat volumetrically and require novel cooling strategies [2].

The miniaturization and integration of disparate electronic components also amplify the non-uniformities in heat generation. Submillimeter regions at transistor junctions can reach fluxes as high as $5 \ \mathrm{kW/cm^2}$, significantly more than the background heat flux, and the resulting temperatures such as those adjacent to transistor gates, can exceed 300°C [5], [6]. Large thermal gradients across devices can cause further performance degradation and/or device failure. Leakage currents within a hot spot can create positive feedback in temperature, and cause thermal runaway and device burnout [7]. Mismatches in coefficients of thermal expansion can lead to mechanical failure. Advanced ICs that operate at high frequencies can also fail to operate properly due to thermally induced-clock skew caused by local temperature changes reducing clock speeds at different rates [1].

Background heat fluxes of high power, high frequency electronics can now surpass $1 \ \mathrm{kW/cm^2}$, with hot spot heat fluxes of over $5 \ \mathrm{kW/cm^2}$ [2,3]. Widely used fin-fan thermal management strategies, that use numerous thermal conduction resistances placed in series, cannot dissipate these ultrahigh fluxes while maintaining chip junction temperatures within their recommended operating conditions.

1.2 Thermal Management Literature Review

Traditional strategies for cooling electronics have relied on conducting heat away from the transistor junction, through the substrate, across thermal-interface materials and to a heat spreader, where it is ultimately dissipated by a remote working fluid in an ambient environment, as shown in Figure 1(a) [8].
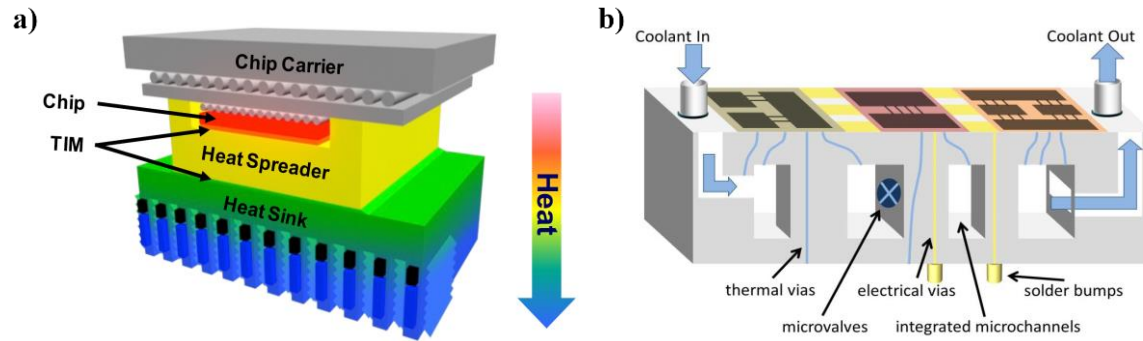
Figure 1-1 Cooling paradigms for integrated circuit. a) Traditional remote cooling: heat generated in the chip conducts and spreads through multiple materials and interfaces before being removed by a remote working fluid. Adapted from "Thermal Packaging - The Inward Migration," by A. Bar-Cohen in *Technical Symposium on Thermal Management*, 2012. b) Embedded cooling: heat generated in the chip conducts directly into the working fluid that is integrated into the substrate of the IC (or in between substrates, for 3D stacked IC's). Adapted from "Micro and Nano Technologies for Enhanced Thermal Management of Electronic Components," Bar-Cohen, K. Matin, and J. Maurer, *Micro/Nano Manuf. Work.* - Michigan, 2013.

Advancements in microtechnologies have helped in the development of novel flow and heat transfer paradigms that have pushed single-phase gas convection to its limits. Some geometrical innovations that have shown promise include disruptive wall structures (ribs, cavities, dimples, protrusions), and secondary channels along smooth-walled channels with curved flow passages. Structures such as cavity and ribs, fins, vortex generator, converging-diverging side walls and curved axis, disrupt flow and thereby enhance heat transfer. These innovations have resulted in greater heat transfer capabilities for the same pumping power, *i.e*., have higher thermal enhancement factor, compared to straight-axis, smooth wall channel configuration. Disruptions in wall structures increase heat transfer by reducing boundary layer growth and augment shed vortices as well as secondary channel flow. Also, flow curvature enhances the formation of secondary rolls, and at higher Reynolds number, morph into chaotic advection. The sinusoidal channel, an example of curved axis, creates maximum secondary vortices or dean vortices that result in greater heat transfer with less pressure drop.

Chip-level embedded cooling, shown in Figure 1b, removes many of the interface and conduction resistances of the conventional heat rejection pathway mentioned above, and offers a way to reduce the size, weight, and power (SWaP) of the thermal management solution. Heat conducts directly into the working fluid which flows within the substrate of the ICs, or in the case of a stacked, vertically integrated device, flows around individual device layers.

Single-phase and two-phase microfluidic cooling have been researched and implemented in embedded cooling approaches [1], [10], [11]. Adham et al. (2013) reviewed the flow of various coolants - air and gasses (helium, nitrogen, argon), and fluids (water, deionized water, nanofluids) through microchannels. They concluded that for high power-density thermal management needs, liquid coolants were superior to air/gas coolants because of the generally higher specific heat of liquids.

In 1981, Tucker and Pease reported that compared to single-channel sink of similar flow volume, water (used as the coolant) flowing through an arrangement of straight and parallel rectangular microchannels on a silicon wafer, exhibited enhanced heat transfer by increasing surface areas of intermediate side walls in the microchannel sinks.   But increase in wall area also enhances the friction factor. Both heat transfer (Nusselt number, Nu) and pressure drop (friction factor, f) are increased. The ratio of increased heat transfer coefficient achieved with identical pumping power of modified channel to that of corresponding basic channel with smooth wall and straight axis, has been defined by Webb (1981) as the thermal enhancement factor (TEF). As TEF number goes beyond unity, heat transfer overrides negative effects of pressure drop (thermal performance). Thermal performance changes with different geometric configurations of smooth and straight channels. For channels of similar diameters, the average flow velocity and discharge are proportional to the Reynolds number (Re). Nu corresponding to the same pumping power, indicates different Re for the basic and modified channels. Innovations in microchannel systems have focused on achieving high Nu with reasonable f by modifying smooth and straight channels. For similar pumping power, multichannel systems are more efficient than single-channel system [10]. Microchannels of smaller

hydraulic diameters need higher pumping power, which can cause leakage in microsink; the latter can disrupt proper functioning of electronic devices.

Liquid to vapor phase change heat transfer is a promising cooling strategy because of the associated latent heat of vaporization, which is usually an order of magnitude higher than the specific heat capacity of the same fluid convecting in a single phase. Microchannel flow boiling is one such approach capable of meeting the thermal management requirements of high heat flux integrated circuits. But it is limited by dynamic flow instabilities [4,5]. Mass flow rate fluctuations can result from differences in densities of the two phases. In order to maintain a constant average mass flux, generated vapor must accelerate. This can result in periodic wetting, bubble expansion, flow reversal, and dryout [6].

Phase-change cooling has received significant interest in addressing the heat flux requirements of high ($\sim 10^3 \, \text{W/cm}^2$) and ultra-high ($\sim 10^4 \, \text{W/cm}^2$) performance systems because of significant reduction in SWaP [11]. Specifically, flow boiling in microchannels has become an active area of research [7], [12]–[15]. Using water, heat fluxes, q'', of around 200 W/cm^2, with heat transfer coefficients, h, of $\sim 5 \, \text{W/cm}^2\text{K}$, and exit qualities of up to 90%, have been reported [16]–[18]. Two-phase flows experience higher pressure drops and this may necessitate higher power requirements and lower coefficient of performance (CoP, defined as the ratio of the heat removal rate to the rate of work entering the system, being the required pumping power).

Evaporation for high flux heat dissipation has been studied theoretically and experimentally [19], [20]. The heat transfer coefficient of a two-phase system with efficient vapor transport depends largely on the heat conduction characteristics between the substrate and the liquid-vapor interface. The thin film region found between the absorbed liquid on the substrate and the bulk meniscus, seen in [21] exists beyond the effects of adhesion forces. This area provides the maximum interface curvature, has the smallest thermal resistance, and accounts for as much as half of the interfacial flux from a macro-sized liquid menisci [20]. High heat transfer coefficients and ultra-high heat fluxes can be sustained across the entire interface area by

5

evaporating liquid from pores that are smaller in diameter rather than by changing the thickness of the thin film region (~0.5 µm).
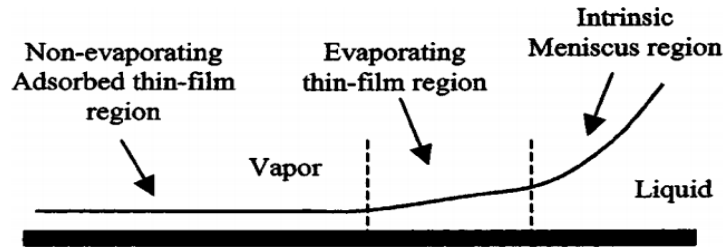
Figure 1-2 Regions of an evaporating extended meniscus. Adapted from "Characteristics of an evaporating thin film in a microchannel," by H. Wang, S. V. Garimella, and J. Y. Murthy, Heat Mass Transf., vol. 50, no. 19–20, pp. 3933–3942, 2007.

Annular flow, when a thin liquid film coats the channel wall, with a large vapor core is typically observed at the tail section of the device. Due to low conduction resistance, the thin liquid film promotes high rates of evaporation into the vapor flow at the center of the channel. Critical heat flux (CHF) occurs when the liquid film in the annulus of the channel is no longer stable. At a flux above CHF, dryout occurs and a drastic increase in channel wall temperature is needed to dissipate that same flux due to the higher thermal resistance of single-phase, gas convection. Therefore, delaying CHF is necessary for high heat thermal management. There is a need to dissipate heat efficiently; measured as the ratio between the heat flux and the temperature difference between the channel wall and the saturation temperature, known as the heat transfer coefficient (HTC). When limited to a finite temperature difference budget, being able to dissipate more heat is advantageous. Maximizing the HTC value is also required for thermal management to remain within temperature limits for IC devices.

Water has excellent heat dissipation for flow boiling in microchannels due to its high latent heat of vaporization, high thermal conductivity and high specific heat. But it is not an ideal solvent for all thermal management applications such as in aerospace, where the thermal management solution must operate over

a wide range of temperatures from subzero Celsius to optimal semiconductor temperatures. Methanol and other low surface tension liquids have the potential to operate in this temperature range.

1.3   Scope and Organization of Thesis

The focus of this thesis is two-fold. First, to investigate the thermohydraulic performance changes by the addition of micropillar wicks during microchannel flow boiling, using working fluids other than water. And second, to test, validate—qualitatively and/or semi-analytically, and come up with mechanistic underpinnings to explain the experimental observations and empirical data trends. Therefore, the structure of the dissertation is as follows: Chapter 1 introduces the necessity for improved cooling strategies for electronics, particularly embedded cooling strategies leveraging phase-change, and challenges that have prevented the widespread adoption of these strategies. In Chapter 2, the concept of microchannel heat sinks with micropillars on the heated surface is presented. Conceptual design considerations, performance using water as the working fluid from earlier reports, and selection of working fluids other than water are discussed. In Chapter 3, experimental methodologies used to characterize the thermohydraulic performance are described, including sample fabrication, experimental test setup, and data processing. In Chapter 4, flow boiling experimental results for methanol across a wide parametric range, are presented and their significance discussed. In Chapter 5, results from using different working fluids—water, methanol, and HFE 7000 are compared. Also, included in this chapter are some mechanistic understandings derived from this work, and some situational optimization strategies have been suggested. Chapter 6 summarizes the thesis and posits future research directions based upon information obtained from the work presented in previous chapters.

Chapter 2- Surface Structure Enhanced Microchannel Flow Boiling

2.1 Microstructure microchannel flow boiling

Flow boiling cooling in micro/minichannels has been improved by altering surface wettability using: surface modification, nanoparticle fluid mixtures [22]–[24], enhancing vapor removal, and/or intensifying bubble nucleation. Mitigating flow instabilities in order to delay critical heat flux is a continuous battle against large enhancements of cooling rates [18], [25], [26]. Flow boiling studies in microchannels have shown that microstructures can suppress the instabilities that lead to dryout, and thereby increase CHF [5], [27][5], [28]. Zhu et. al. (2016) reported that microstructures offered a 57% CHF and HTC enhancement with flow boiling water [29]. Microstructures are integrated only on the bottom heated surface where the wall temperature and the heat flux are the highest. Capillary pressure-driven flow created by the menisci formed between hydrophilic pillars, sustained a liquid film at higher heat fluxes [29]

Two-phase microchannel heat sinks can address the challenges of high-flux heat dissipation and maintain a more uniform temperature control in various electronic devices because of latent heat of vaporization and isothermal nature of phase change. Microchannel heat sinks are an attractive thermal management strategy for two reasons: (a) the large surface to volume ratio offers lower thermal resistances than its macroscale counterparts, and (b) its small footprint can be used to tailor thermal management design for cooling small electronic devices with footprint <1 cm^2. However, the main challenges with these microchannel devices are associated with flow instabilities [30], [31], and the need to increase the Critical Heat Flux (CHF) [32], [33]; the former issue arises from the dominance of surface tension at the small length scales (*i.e.*, much lower than the capillary length). The rapid expansion of vapor bubbles occupying the cross-section and length of the microchannel before bubble departure leads to large pressure fluctuations in the flow channels (*i.e.* instabilities) and liquid dryout during boiling. This dryout significantly limits the heat removal capability of microchannel heat sink systems and results in spiking of surface temperatures due to the

presence of transient vapor films. Therefore, recent studies have used various techniques to mitigate the flow instability and enhance heat transfer by including inlet restrictors [34], expanding cross-section microchannels [35]–[38], nucleation sites [39], [40], reentrant cavities [41], [42], microbreathers [43], [44], and nanowire-coated surfaces [27], [45]–[48] integrated into the microchannel.

Passive capillary-pumped thermal ground planes take advantage of phase-change cooling, with near unity exit vapor qualities and high heat flux dissipation. These systems operate on capillary pressures, P_c, generated by surface tension at the liquid-vapor interface at the end of small passages of a wick, and is governed by the Young-Laplace Equation:

$$P_c = \frac{2\sigma \cos \theta}{d_p}$$

where d_p is the pore diameter, σ is the surface tension, and θ is the contract angle between the liquid and the solid wick. Examples include micro/nano-structures such as sintered copper mesh coated with carbon nanotubes [49], titanium nanopillars [50], silicon micropillars [51], and oxidized copper microposts [52].

Values of $q^{''} \cong 500$ W/cm^2 and $h = {\sim}12$ W/cm^{2}K have been reported for heated areas of 5×5 mm^2, however in many cases they represent mixed mode evaporation and boiling. The capillary pressure generated at the liquid-vapor interface competes with the viscous pressure drop of the liquid transport through the wick. Once viscous losses exceed the capillary pressure budget in these systems, the meniscus of the working fluid recedes, drying out of the wick ensues, and the device temperature spikes. Hierarchical fluid supply networks aim to reduce viscous losses which limits performance while preserving the driving capillarity. Flow architectures such as supply arteries [53], bi-porosity [54]–[56], and fractal-like biomimetic networks [57], [58], have been able to reach thermal dissipation around $q^{''} = 990$ W/cm^2 with $h = 6.7$ W/cm^2 K [59].

2.2   Flow Boiling Instabilities

Formation of instabilities is an inherent characteristic of two-phase flow boiling in microchannels (Prajapati and Bhandari, 2017).   Figure 2-1 summarizes the major causes for flow boiling instabilities in microchannels. Microchannels have relatively large ratio of surface area to volume, and this causes high heat transfer rate. But at the same time, because of their small hydraulic diameters there is higher frictional pressure drop within the channels. In microchannels, phase change from liquid to vapor can occur from heat application or from reduction in pressure or both. In two-phase flow, total pressure drop increases significantly from both acceleration pressure drop as well as frictional pressure drop. During flow boiling, higher heat transfer rate is achieved using relatively small amounts of coolant, and since cooling takes place at constant temperature there is less chances of hot-spot formation. At high heat flux, large amounts of vapor are generated, and this causes rapid bubble growth—in both upstream and downstream sections, leading to flow instabilities. Flow instabilities can also be due to uneven distribution of coolant between channels, pressure and temperature fluctuations and intermittent flow reversal resulting in local dryout. Instabilities during flow boiling at the macro level can be (i) static (associated with steady state laws) such as Ledinegg instability as well as (ii) dynamic. Static instability is affected by system pressure, since increasing pressure can reverse instability within the microchannel. Increasing the number of parallel channels with smaller length to diameter ratio, also improves static stability. Dynamic instabilities in macro passages arise from oscillations in pressure drop, temperature and density wave. These oscillations are affected by mass flux, coolant subcooling and heat flux. Flow boiling instabilities in microchannel are sensitive to confined narrower flow passages, and flow boiling in microchannels creates unique bubble dynamics that results in dynamic instability [60]. The unique bubble dynamics, includes bubble clogging, and rapid bubble growth/elongation and flow reversal, is caused by several factors such as inherent confined geometry of the microchannels, operating and flow conditions, properties and quality of dissolved gasses, working fluid, upstream compressibility and design of flow loop. Large inlet subcooling condition also increases two-phase instabilities in microchannels. Instabilities during flow boiling in microchannels

depend upon mass flow rate, flow regimes, bubble dynamics, inlet subcooling, inlet compressibility and coolant properties. Various techniques have been developed to reduce instabilities such as geometrical modifications.
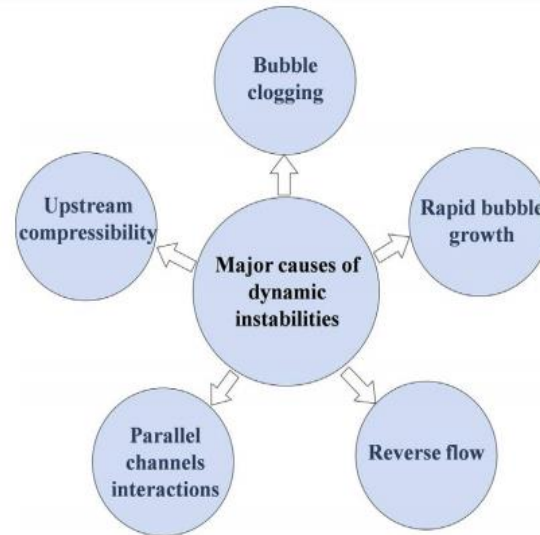
Figure 2-1   Flow boiling instabilities in microchannels. [Reproduced from 59]

Previous studies have attributed the reduction in instabilities to pressure regulation of inlet restrictors [34], tuning nucleation site dimensions to promote bubble formation at lower superheats [39], [40], [46], increase in nucleation density from the reentrant cavities [41], [42], and local venting of generated vapor by a porous hydrophobic membrane (microbreather) [43], [44].   Micro/nanostructure coated surfaces have the advantage of avoiding any additional pressure drop across the inlet restrictors and delaying dryout by capillary wicking. Li et al. [27] reported an enhancement in flow boiling heat transfer performance with silicon nanowire-coated channel surfaces, using water as the operating fluid. Yang et al. [45]–[47] also reported increased CHF and reduced pressure drop with silicon nanowire-coated channel surfaces and water as the coolant. They concluded that the enhancement in CHF was due to the wicking ability of the hydrophilic nanowires which rewet the surface and prevented dryout. This was in addition to the creation of favorable nucleation cavities by the nanowire fabrication procedure. While there is empirical data that indicate that micro and nanostructure coated surfaces in microchannel heat sinks enhance the performance

of these devices, the precise role of capillary-length-scale surface structures on flow instability is not well-understood. The hydrophilic structures generate capillary pressure, but they also create viscous resistance as the liquid rewets the surface [62]. Recent studies [48] have used dielectric solvents and silicon nanowire coated surfaces, similar to those used by others [27], [45], [63]. These studies have reported an increase in the heat transfer coefficient (HTC) but a decrease in CHF for nanowire coated surfaces compared to a flat surface device. The effect of surface structure geometry on viscous resistance, which hinders the rewetting process, has not been thoroughly investigated. Conflicting results have failed to establish any definitive interaction between surface structures and working fluids on heat transfer, and thus this formed the basis for the present research and device concept described below.

2.3 Device features and design objectives

In high heat flux applications, microchannel heat sinks usually operate in the annular flow regime due to the high vapor quality associated with heat dissipation in the confined space. Since evaporation can be a predominant factor in the annular flow regime, Zhu et. al. and others designed structured surfaces to enhance and sustain stable liquid film evaporation [37, 77]. Structures were integrated only on the bottom heated surface where the wall temperature and the heat flux are the highest and suppresses liquid dryout by generating capillary flow in the presence of menisci formation (Figure 2-2). This capillary flow can be created both along the channel direction and from the sidewalls to the center. To promote nucleation, sidewalls had tailored roughness of 1-2 µm. By nucleating the side walls, dryout was less likely to occur on the bottom surface; this typically happens in the case of smooth microchannel walls due to the higher super heat required for nucleation leading to explosive bubble growth.
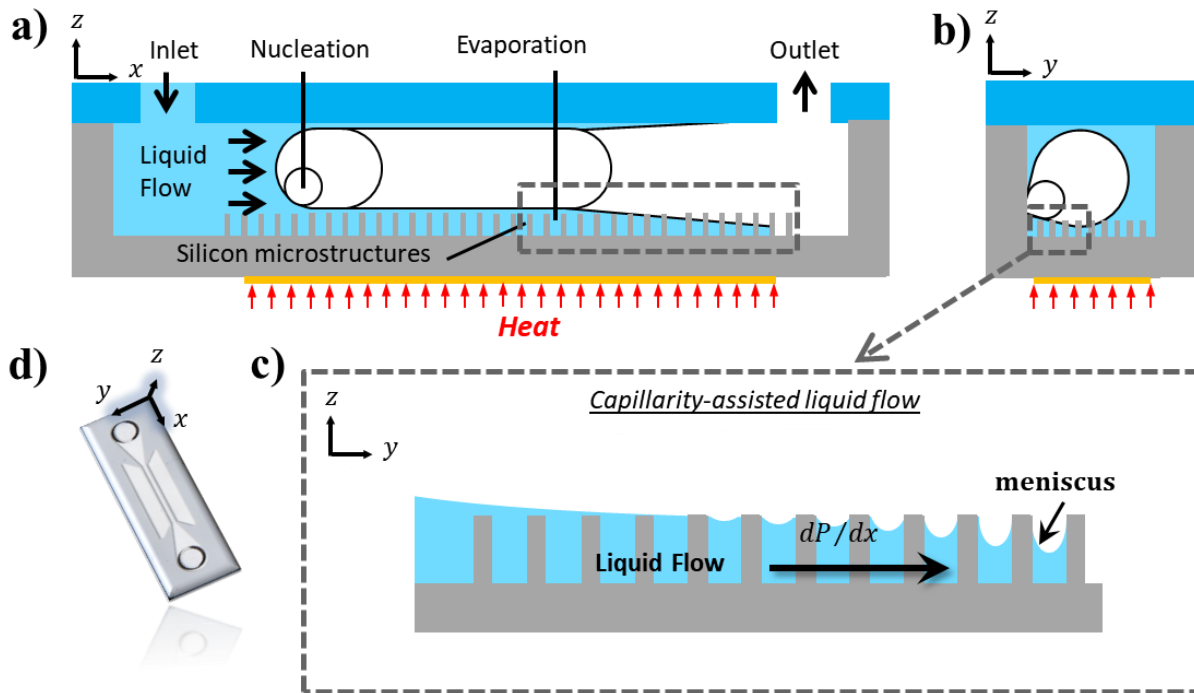
Figure 2-2 Schematic of microchannel heat sink design with micropillars on the heated surface. (a) axial (along the flow direction) cross-section of a single channel device, (b) transverse (normal to the flow direction) cross-section view, with a representative bubble, preferentially nucleating on the side wall of the channel and not on the micropillared channel bottom, (c) magnified view of the micropillars (shown in (b)) with a liquid film and receding menisci at the hottest wall section of the device, which created the capillary pressure gradient, dP/dx, and forced liquid back to any spot in the channel that temporarily dried out, (d) orients the different cross-sections of the device, where the two circles are the fluidic inlet/outlet of the device connected by the single microchannel, flow boiling test section.

Zhu et. al. numerically modeled thin-film evaporation, dryout heat flux from a micropillar wick array [64]. Figure 2-3 shows the modeling strategy. The finite volume simulation, evaluated liquid velocity, pressure, and the meniscus curvature by conservating of mass, momentum, and energy for each unit cell along the wicking direction. The heat flux responsible for causing the menisci furthest from the bulk liquid supply to depin from the tops of the micropillars, was determined to be the dryout heat flux.
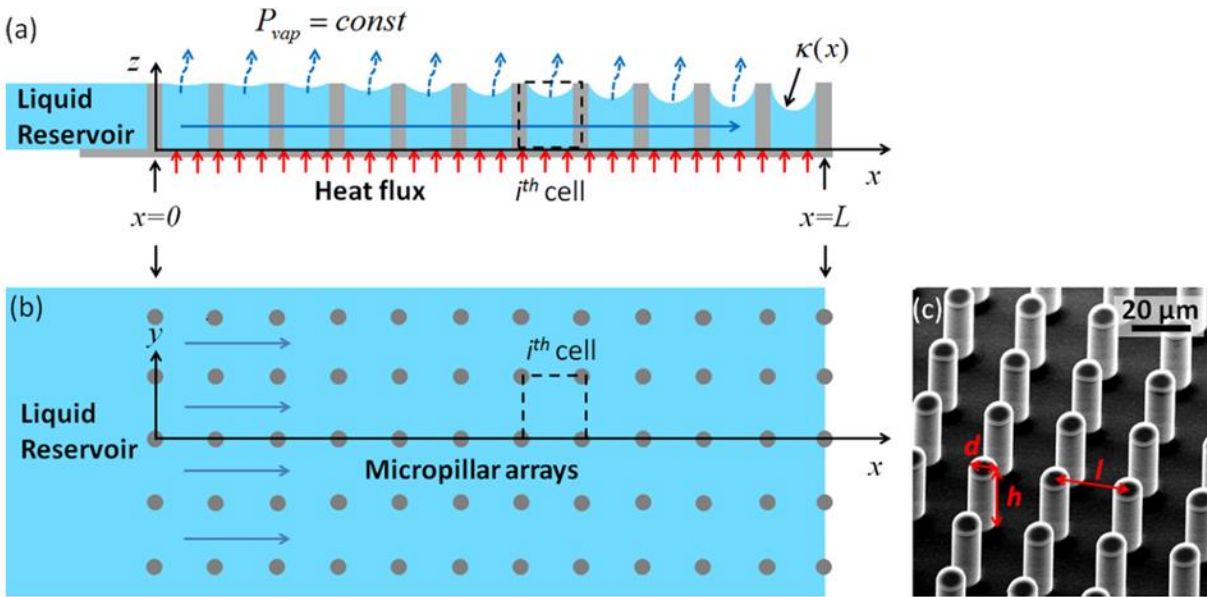
Figure 2-3 Schematic of dry-out from an evaporating micropillar wick. (a) Side view and (b) top view of the physical domain for dry-out heat flux used in Zhu et. al. (2016) model. Capillary-pumped liquid film evaporates on a hydrophilic micropillar array surface of length L, where a uniform heat flux is applied. The vapor pressure, P_v is constant. The spatially varying curvature of the liquid−vapor interface, κ(x), which is greatest at x $=$ L and the surface tension of the liquid, sets the capillary pressure generated to transport the liquid from x $=$ 0. (c) A representative SEM image of a fabricated silicon micropillar array with diameter d, pitch l, and height h. (adapted from [79])

Using this model, a parametric sweep of micropillar wick geometries (pillar diameter, height, pitch) was performed for a range of geometries optimal for thin-film evaporation of water, and test samples were fabricated.

2.4 Flow boiling enhancement of water

Zhu et. al., 2016 experimentally characterized single microchannel flow boiling of deionized water and showed significant heat transfer enhancement from devices with micropillar wicks on the heated bottom wall. Flow visualization confirmed that microstructures stabilized the liquid film at heat fluxes where the smooth sample was mostly dry and only had some droplets of water present (see representative optical images in Figure 2-4, at a heat flux of $430\ W/cm^2$). As expected, the presence of a stable liquid film at

higher heat fluxes for the microstructured samples conferred a number of thermohydraulic benefits. Temporally resolved local temperatures and the pressure drop between the inlet and the outlet of the microchannel, numerically captured these benefits.

The isothermal nature of phase-change contributed to the stability of the locally measured heater temperatures. Conduction across a thin liquid film from which heat can be removed though evaporation- by enthalpy/mass removal, is a very steady process compared to the cyclical nature of boiling, particularly on the smooth surface. Superheating the working fluid sufficiently high enough for nucleation to begin (see Section 5.4.5 for a more detailed section of nucleation, and how it can behave very differently under different operation conditions), can be followed by explosive vapor generation. This can result in flow reversal, because of the presence of significantly superheated liquid being very close to the newly formed liquid vapor interface. Evaporating superheated fluid can quickly remove heat and cool down the device possibly by removing enough heat fast enough that the heat transfer mode goes back to single phase, liquid cooling.

Changes in visualization indicates that microstructures promote capillary wicking and suppress dryout of sample referred to as 'S4' (which had the following silicon pillar geometry: $d = 10 \ \mu m, h = 25 \ \mu m, l = 40 \ \mu m$) by Zhu et. al., 2016. A stable liquid film, not observed for the smooth surface, was seen covering the pillars of the structured surface microchannel ([29], top left, in red). Compared to the smooth surface, dryout on the structured surface occurred less frequently, persisted for shorter durations, and created smaller dry surface area.
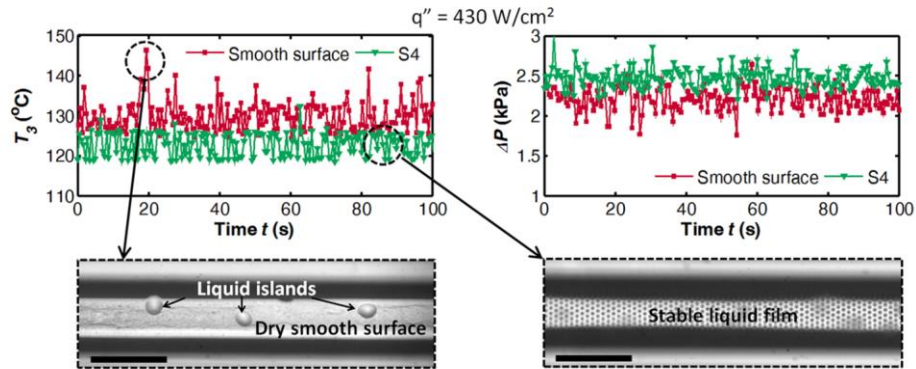
Figure 2-4 Temporally resolved representative data for microchannel flow boiling of water. Local temperature (top left plot) and pressure drop measurements (top right plot) with corresponding flow visualizations of a smooth (bottom left image) and a microstructured (bottom right image) single-microchannels undergoing flow boiling of water with a mass flux of $G = 300 \text{ kg/m}^2\text{s}$, in order to dissipate similar heat fluxes of $q'' \cong 430 \text{ W/cm}^2$. Annotated optical images of bottom channel surfaces have scale bars of 500 μm.

The periodic dryout described above, can result in a lower observed CHF and a higher time-averaged wall temperature rise. The higher average temperature for the same heat flux translates to a lower heat transfer coefficient for the smooth samples. The boiling curves for 4 structured samples and a smooth sample at a moderate mass flux of water at $G = 300 \text{ kg/m}^2\text{s}$, shown in Figure 2-5a, summarize these findings at high heat fluxes. All structured samples showed an increase in CHF and HTC. A maximum heat flux of 969 W/cm^2 was achieved (57% enhancement compared to smooth surface microchannel that had a CHF of 615 W/cm^2). Dissipating 615 W/cm^2, the device temperature of the best performing microstructures sample ('S4,' shown in green) was 19.5 K cooler that the smooth sample (nearly a 100% increase in the HTC, when using the device temperature as the referencing temperature). The pressure drops within structured surface microchannels and smooth-surface microchannels were not significantly different (Figure 2-5b).
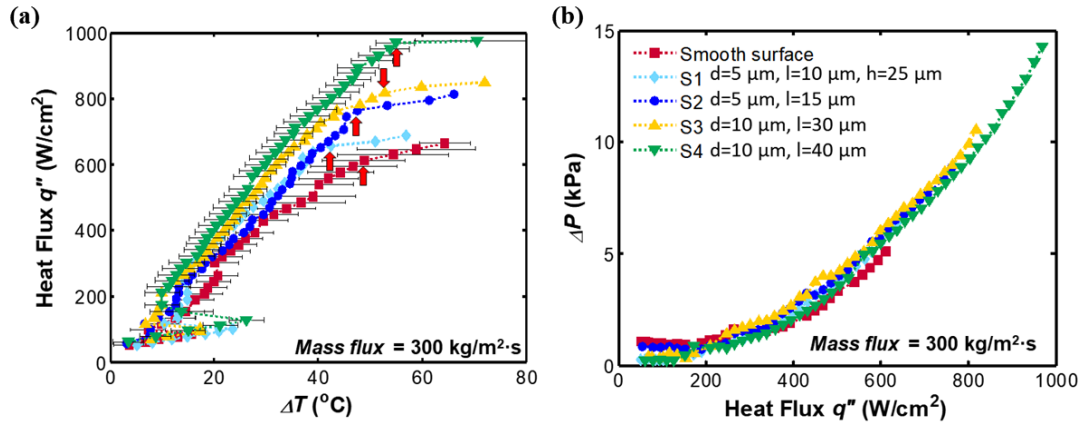
Figure 2-5 Heat transfer performance of single microchannels flow boiling of water. (a) boiling curve (heat flux q'' versus heater temperature rise (ΔT). Arrows indicate CHF. (b) pressure drop across the microchannel as a function of heat flux for the devices investigated. (reproduced with permission [29])

Finally, support for the notion that these enhancements in performance were capillary driven, comes from the relatively good scale agreement between the predicted dryout evaporative heat flux from the micropillar wick geometries and the measured flow boiling CHF.

2.5 Selection of alternative working fluids

The high-fidelity numerical model for dryout heat flux by Zhu et. al. (2016) can be computationally expensive, especially when parametrical sweeping over lots of geometries and when predicting evaporative performance of several different working fluids need to be done. Adera et. al., 2016 [65] solved the same set of conservation partial differential equations and came up with an explicit, analytical expression for the dryout heat flux [65]. This was achieved by imposing the following assumptions that: (i) the flow in the micropillar arrays remain 2-D and laminar, and (ii) a constant pressure gradient is applied from the liquid supply to the initial dryout spot. A detailed derivation of this expression can be found in Adera et. al., 2016 [65].

Solving the governing equations, the dryout heat flux from a thin-film evaporating micropillar array wick, q''_{max}, can be defined as

$$q''_{max} \cong \frac{40}{3} \, \Phi_{wick} \, \psi \, \cos\theta_{rec}$$

where $\Phi_{wick} \equiv \frac{\sigma\rho_l\,h_{fg}}{\mu_l} \, \left[W/_{m^2} \right]$ is the Wicking Figure of Merit (FOM)—a measure of the capillary-limited

maximum heat carrying capacity of the working fluid and has the units of heat flux (W/m^2) [10]. The

Wicking Figure of Merit is a commonly referenced performance metric in the heat pipe industry. Ψ is a

lumped, dimensionless factor that incorporates the different geometric configurations of the micropillar

wick.

$$\psi \propto f\,(h, d, l, K, L_{dry})$$

where, h, d, and l are the micropillar height, diameter, and pitch/spacing, K is the flow permeability, for

which numerically and/or empirically derived expressions based on the pillar array geometries exist (such

as the ones presented by Sangani and Acrivos [66]). Adera et. al., 2016 [65] modified permeability to

account for the influence of the meniscus curvature, that reduces the effective hydraulic diameter through

which the capillary driven working fluid flows. Therefore, ψ has very slight dependence on the receding

contact angle, and thus a material property.

When selecting working fluid alternatives for water that would allow one to probe the flow boiling

thermohydraulic performance and its sensitivity to surface tension and microstructure geometries,

following properties were considered: 1) Wicking Figure of Merit for the fluid, 2) saturation temperature

in comparison to the IC operating temperatures, 3) whether the other desired traits hold true or not at near

atmospheric pressures, and 4) toxicity, hazard level and environmental impact of the fluid.

Adera et. al. (2016) [61] derived and validated an analytical model that highlighted the positive, linear

dependence of thin-film, capillary wicked, dryout heat flux on the Wicking Figure of Merit, and Zhu et. al.

(2016) [60] showed that flow boiling CHF scaled well with predicted dryout heat flux. The first fluid

selection criterion should be to select fluids with higher upper limits to the heat fluxes they can remove

through flow boiling. Secondly, larger the difference between the isothermal, phase-change temperature and the substrate's recommended operating condition, the greater driving potential exists to dissipate heat. The third requirement was safety and global impact considerations. The last consideration was to minimize/eliminate complexity and costs that are associated with maintaining low vacuum or high pressurization.

Plotted in Figure 2-6 are the Wicking Figures of Merit for different working fluids operating near atmospheric pressure. For the same wick geometry, of the fluids selected for study, water (shown in black) clearly has one of the best Wicking FOM (*i.e.* predicted thin-film, dryout heat fluxes). Compared to other common solvents (ethanol and pentane) and currently-used fluorinated refrigerants (R134A and R245FA), methanol has the highest Wicking FOM at the conditions tested, but is predicted to be smaller than that of water by an order of magnitude.

Finally, an engineered solvent from a comparatively new class of fluids, hydroflouroethers (HFEs), was selected for flow boiling characterization. HFEs have very good dielectric properties and are already being adopted for electronic pool boiling applications such as data center cooling. Unfortunately, they have some of the worst thermophysical properties for capillary driven phase change, particularly, they have very low surface tension, and so their predicted dryout heat fluxes are an order of magnitude smaller than that of methanol. Such challenging properties of capillary driven phenomena need to be carefully investigated for a better mechanistic understanding of the process.
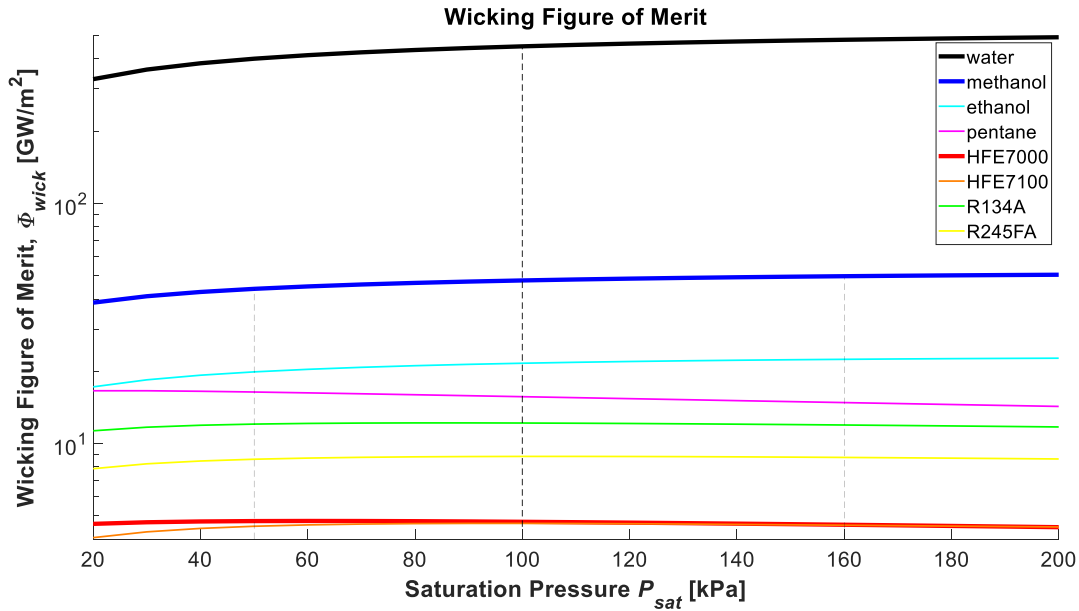
Figure 2-6   Wicking Figure of Merit for select working fluids at near atmospheric pressure conditions.

The wicking FOM, Φ_{wick}, for methanol and HFE 7000 are around one and two orders of magnitude lower than water, respectively. As mentioned above, the dryout heat flux from a thin-film evaporating micropillar array wick scaled directly with that Φ_{wick}, and the microchannel flow boiling critical heat flux, CHF, for microchannels with micropillar array wicks, showed a strong qualitative correlation with the dryout heat flux. Therefore, when using the same pillar arrays, switching to lower surface tension working fluids, a decrease in flow boiling CHF by several orders of magnitude, was predicted. To get better CHFs, the other parameter used to predict dryout heat flux - geometric term ψ, was increased. A second set of micropillar array wick samples were fabricated with the same diameter and pitch but with triple the height (nominally 75 µm). This height was chosen as a comfortable fabrication target. Table 2-1 presents the dryout heat flux for 4 pillar array geometries using the three selected working fluids - water, methanol and HFE700.

Table 2-1 Dry-out evaporative heat flux for micropillar wick arrays 250 µm long

	Max thin-film evaporative flux for wicking 250 µm $\left[{kW}/{cm^2}\right]$		
	Water $\Pi_{1,H_2O} \sim 4.5 \cdot 10^{11}\ {W}/{m^2}$	**Methanol** $\Pi_{1,CH_3OH} \sim 4.7 \cdot 10^{10}\ {W}/{m^2}$	**HFE 7000** $\Pi_{1,HFE} \sim 4.7 \cdot 10^{9}\ {W}/{m^2}$
Short-dense $[d, h, l] = 5, 25, 10\ \mu m$ $\psi_{sh.dn.} \sim 2.6 \cdot 10^{-5}$	16.3	1.67	0.17
Short-sparse $[d, h, l] = 10, 25, 40\ \mu m$ $\psi_{sh.sp.} \sim 1.2 \cdot 10^{-5}$	12.7	0.76	0.074
Tall-dense $[d, h, l] = 5, 75, 10\ \mu m$ $\psi_{tl.dn.} \sim 1.0 \cdot 10^{-4}$	61.4	6.59	0.65
Tall-sparse $[d, h, l] = 10, 75, 40\ \mu m$ $\psi_{tl.sp.} \sim 3.0 \cdot 10^{-4}$	19.7	19.2	1.89
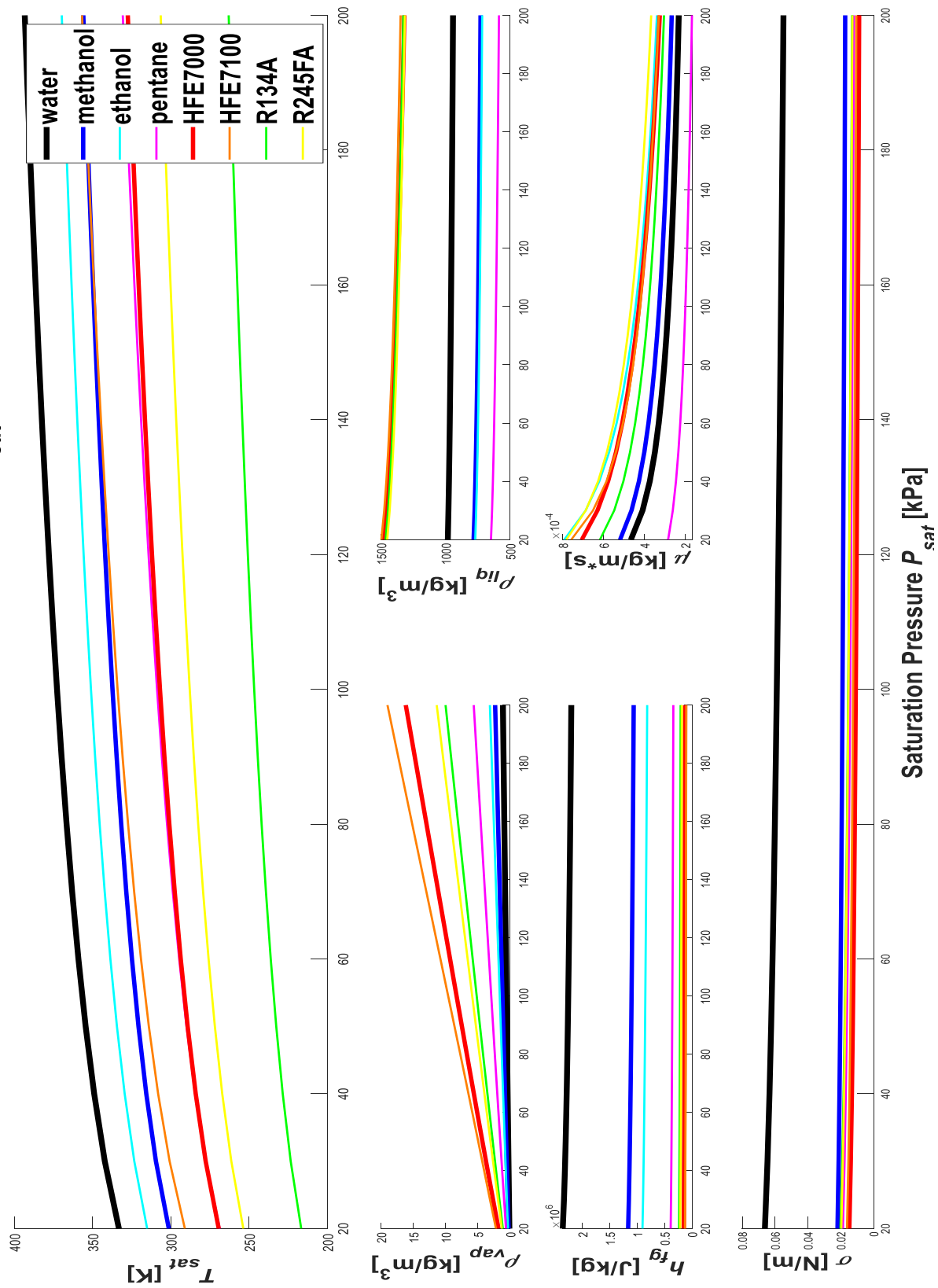
Figure 2-7 Saturated thermophysical properties of water, methanol, ethanol, pentane, HFE 7000, HFE 7100, R134A, and R245FA as a function of saturation pressures ranging from 20 to 200 kPa. (Clockwise starting from the top in landscape) boiling point $\equiv T_{sat}$ [K], liquid density $\equiv \rho_{liq}$ [kg/m^3], dynamic viscosity $\equiv \mu$ [kg/$m \cdot s$], surface tension $\equiv \sigma$ [N/m], enthalpy of vaporization $\equiv h_{fg}$ [J/kg], and vapor density $\equiv \rho_{vap}$ [kg/m^3].

22
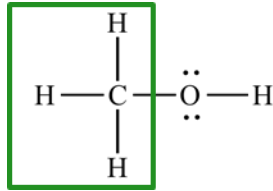
2.5.1   Methanol

Figure 2-8 Chemical structure for methanol, CH₃OH. Highlighted in green is the alkane portion of the molecule. The remaining hydroxyl group, induces a polarity on the molecule.

At atmospheric pressure, methanol has a saturation temperature of 65°C, significantly below that of water. This allows for a larger temperature differential between channel walls and the bulk vapor. Although methanol in nature readily degrades to carbon dioxide, it has a slightly smaller global warming potential than CO_2, and has no Ozone Depleting Potential. Unlike water, methanol and other low surface tension working fluids have poor thermophysical properties for capillary pumped evaporative phase change. For the same mass flow rate, methanol can remove less heat through sensible cooling and evaporation/boiling. Lower surface tension along with comparable viscosities result in methanol generating lower maximum capillary pressures before the meniscus starts to recede. Also, the highly wetting nature of methanol requires higher superheats before the onset of bubble nucleation. Due to these thermophysical limitations, boiling enhancement from the microstructures may not be as notable for low surface tension fluids as it is for water.

2.5.2   HFE 7000

Hydrofluoroethers (HFE) are a class of organic solvents developed to replace ozone-depleting chemicals CFCs, HFCs, HCFCs, and PFCs. HFE 7000, also known as RE347mcc, in the ASHRAE designated R-system of refrigerants and sold under the tradename of Novec 7000 (3M®, Maplewood, MN), is methyl perfluoropropyl ether (methoxyperfluoropropane) and has a chemical formula of $CF_3CF_2CF_2OCH_3$ (chemical structure shown below):
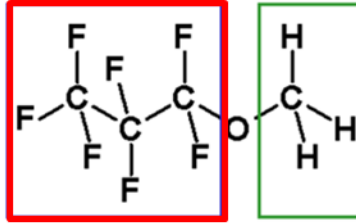
Figure 2-9   Chemical structure for HFE 7000. Highlighted in red is the fluorinated alkane chain and highlighted in green is the methyl group. Together, these groups make it hard for the lone electron pairs of the oxygen to align into a strong dipole moment, thus rendering it a suitable dielectric fluid.

HFEs have beneficial environmental properties - low toxicity, non-flammable, low greenhouse gas contribution, short atmospheric lifespan (compared to hydrofluorocarbons and chlorofluorocarbons) and are non-ozone depleting. The R-O-R' bond makes it susceptible to break-down easily in the environment, and its larger molecular size, compared to many other fluorinated solvents, helps it to readily leave the atmosphere. These qualities make HFEs attractive working fluids for heat transfer applications. With a dielectric constant of 7.4, similar to that of some solid insulators such as neoprene, it is ideal for electronic thermal management. Commercial systems for HFE based thermal management strategies have being tested and implemented in pool boiling applications such as for server farms and closed heat pipes in power thermal management of electric vehicles. HFE 7000 is the smallest of the HFEs and was chosen for study because of its low atmospheric boiling point $T_{sat}|_{@\ 1\ atm} = 34.2\ ^\circ C$.

While the hydrogen in HFEs increase boiling points compared to analogous perfluoroethers, it also facilitates the solvation of hydrocarbons [28]. Plasticizers and additives, found in almost all plastics, can leach into HFEs. For evaporative cooling, aggregation of non-volatile hydrocarbons at the phase change interface can lead to a significant reduction in cooling performance. Therefore, material compatibility has to be considered.

Chapter 3- Experimental Methodology

In this chapter, fabrication of single channel flow boiling prototypes is presented and the development of multichannel device fabrication process plan is discussed.

3.1 Microchannel Flow Boiling Test Samples

The capillary wicking model described in Chapter 2 suggested that for constrained pillar diameter and pitch, maximizing the pillar height would best offset the reduction in surface tension for water-alternative working fluids. Based on microfabrication tradeoffs (*e.g*., balancing high wafer-scale test sample yield while maximizing the pillar height to pillar diameter aspect ratio), a new pillar height for the micropillar array was selected. Cylindrical micropillar array diameters and pitches were dictated by photolithographic masks that were available and was chosen for capillary wicking enhancement during flow boiling of water.

Single channel devices provide clearer insight into the mechanisms behind flow boiling instabilities, and better inform instability mitigation strategies as well as thermal performance enhancement strategies. Importantly, a single channel device can be measured and controlled for mass flux or pressure drop. However, single microchannel flow boiling as a thermal management strategy has limited application. Microchannel flow boiling's usefulness is based upon its scalability, cooling large foot-print areas, leveraging an increased surface area to volume ratio (this can be achieved by having as many single channels in parallel as needed). However, such extension introduces a new class of parallel channel instabilities. Instabilities arise because of the maldistribution of working fluids from feedback between individual channel oscillations. This creates spatially varying pressure and temperature profiles regardless of initially uniform heat and mass flux conditions. Therefore, fabrication of multichannel prototype devices was necessary to demonstrate that the enhancement provided by microstructured pillar arrays was actually useful. For these initial investigations, devices with five parallel channels were fabricated and studied.

Microstructure and smooth monolithic microchannels test devices were fabricated in silicon substrates. Silicon has been extensively used by integrated circuit (IC) and microelectromechanical system (MEMS) communities, and the development and refinement of processes for silicon has been going on for decades. MEMS lithography, chemical etching, thin film deposition, packaging, and metrology were carried out in a class-100 clean room environment at MIT's Microsystems Technology Laboratories (MTL) and the Nanostructures Laboratory (NSL).

3.1.1 Single channel fabrication process

Single, 500 µm square microchannels 1 cm in length were fabricated and studied. The micropillar geometries on the bottom surface of the microchannel were varied, with diameters of 5-10 µm, pitches of 10-40 µm, and heights of 25-75 µm. These micropillar geometries were chosen because: (1) geometries in this range can be well-controlled and are relatively easy to fabricate in silicon (Si), (2) a wide range of capillary pressures can be generated, ending with comparable values at the typical microchannel pressure drop for even some of the lower surface tension fluids. This allows probing the ability to manipulate flow behavior of lower surface tension fluids as the capillary effects may begin to decrease in significance, (3) surface structures are mechanically strong and do not undergo deformation at the highest capillary pressures generated.

Specific micropillar geometries fabricated and tested are shown in Table 3-1. The effect of micropillar pillar pitch to pillar diameter ratio was determined. Closely arranged, thinner pillar arrays had a l/d ratio of 2, are referred to as "dense" pillar arrays for all such configurations (d = 5 µm and l = 10 µm). Wider pillars with a l/d ratio of 4, are referred to as a "sparse" pillar arrays for all such configurations (d = 10 µm and l = 40 µm). Each set of pillar arrays was fabricated at two different heights: h = 25 µm and h = 75 µm, henceforth referred to as "short" and "tall," respectively. Therefore, micropillars had four configurations: (1) tall and dense, (2) tall and sparse, (3) short and dense, and (4) short and sparse.

Table 3-1   Geometric parameters (height, diameter and pitch) of the fabricated single-channel test devices

Device	Height, h (µm)	Diameter, d (µm)	Pitch, l (µm)
Smooth	-	-	-
"Short-dense"	25	5	10
"Short-sparse"	25	10	40
"Tall-dense"	75	5	10
"Tall-sparse"	75	10	40

To investigate the flow boiling enhancement of surface microstructures, single 1 cm long microchannel devices were fabricated. Each microchannel had an integrated, serpentine patterned, thin-film platinum heater (8.6 mm long x 380 µm wide) directly underneath the microchannel to serve as a heat source via Joule heating. The fixed 1.4 mm offset for the start of heaters from the channel inlet was to provide some opportunity for hydrodynamical flow development, and to address some of the thermal spreading within the 500 µm thick silicon substrate that lay between the heater and the bottom of the microchannel (defined as the normally observable channel wall, opposite side of the Pyrex® viewport). Platinum was specifically chosen due to its high linear relationship between resistance and temperature. At four locations along the length of the heater, thin-film resistance temperature detectors (RTDs) were incorporated. Either straddling the heater or interdigitated between the serpentine pattern of the heater (trace of 50 µm), these detectors (also with a serpentine pattern, but with a finer trace of 4 µm) provided a spatial understanding of the heater temperature, *i.e.* spatially varying wall temperature within the microchannel. RTD1 through RTD4 were located along the center of the channel 0 mm, 1.4 mm, 5.7 mm and 10 mm from the inlet of the microchannel, respectively.

Micropillars were etched on the channel bottom surface, either 25 or 75 µm into a 500 µm thick double side polished (DSP) silicon wafer, using deep reactive ion etching (DRIE). Control microchannel samples with no micropillars were also fabricated by skipping this etching step; these will be referred to as "smooth"

channel. With the above-mentioned described fabrication, channel bottom of the smooth surface was aligned in the plane of the tops of the micropillar. The micropillar samples thus had a larger, length-averaged, cross sectional area that increased with increase in the etched pillar height.
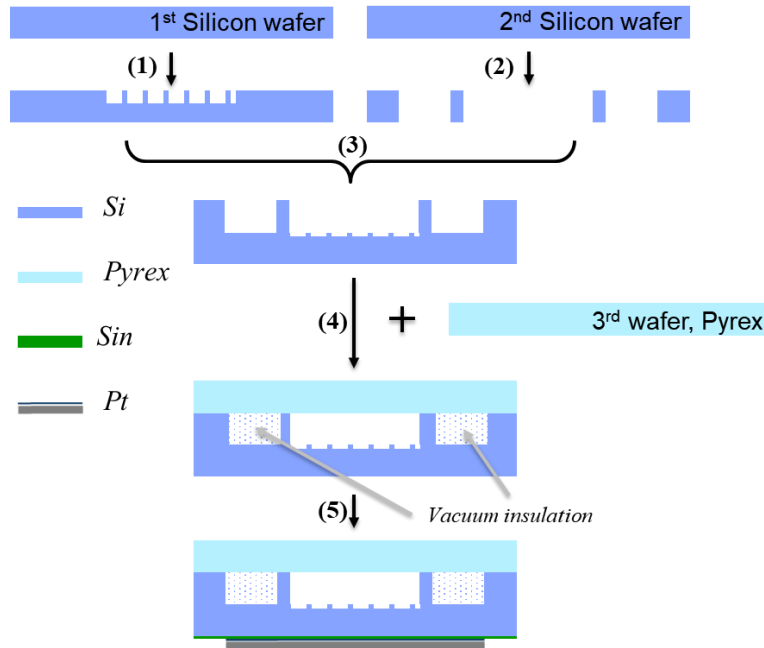
Figure 3-1   Design and fabrication process for single-channel flow boiling devices. (1) Micropillars were etched into a silicon (Si) wafer using deep reactive ion etching (DRIE). (2) Microchannel and insulating vacuum gaps were etched into a separate Si wafer. (3) Wafers were bonded using hydrophilic plasma activated direct Si-Si fusion bonding (not shown); silicon dioxide (SiO_2) was thermally grown, wet etched away, and then regrown. (4) A Pyrex® wafer, pre-etched with inlet and outlet liquid ports (not shown) was anodically bonded in vacuum. (5) A dielectric layer of non-stoichiometric silicon nitride (SiN) was deposited followed by a thin film platinum (Pt) patterned metallization for the proxy heater and resistance temperature detectors (RTDs).

A second 500 µm thick Si wafer was etched through using DRIE to define the channel's side wall. To minimize conduction losses across the test device, two additional closed swathes of silicon were etched out on either side of the microchannel. These pockets in the final device became hermetically sealed vacuum insulation gaps and allowed to better isolate the effect of flow boiling heat transfer in the microchannel. The two Si wafers were then aligned and bonded using hydrophilic plasma activated direct Si-Si fusion bonding. An initial 0.5 µm SiO_2 layer was thermally grown on the Si surface and immediately wet etched

off using hydrofluoric acid. This step was done to smooth out any scalloping that is inherent to the Bosch process used in DRIE. A second 0.5 µm thick SiO_2 layer was thermally regrown for the final surface finish. This provided: 1. higher surface energy to maximize wetting, 2. coating for channel walls, and 3. electrical insulation layer on the backside.

A third and final wafer was wet etched with 3mm fluidic inlet and outlet (I/O) ports. To facilitate optical visualization, this last wafer was made of Pyrex®. Etching was done in buffered oxide etch using a hard mask of polycrystalline silicon. To cover the microchannel, the wafer was aligned and anodically bonded with thermo-compression.

Using Plasma Enhanced Chemical Vapor Deposition (PECVD), a dielectric layer of non-stoichiometric silicon nitride (1 µm thick) was deposited on the bottom (silicon) side of wafers for electrical insulation. Proxy heaters and resistance temperature detectors (RTDs), in 200 nm thick platinum, were deposited by e-beam lithography and patterned metal lift-off using a 20 nm titanium adhesion layer. Heater geometry and dielectric thickness were selected to allow for an upper heater operating condition of 180 V and 0.5 A.
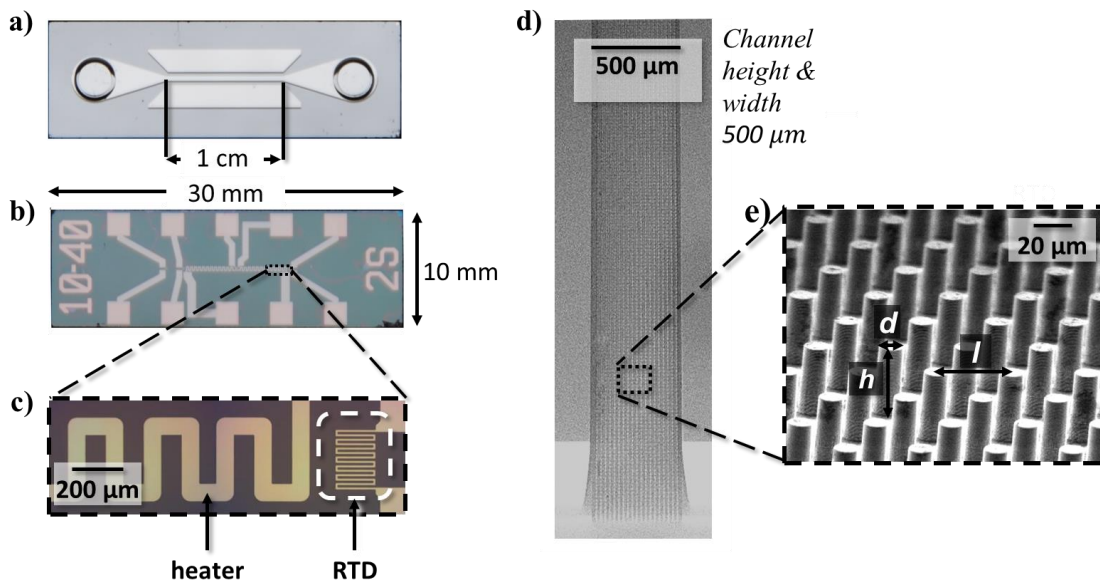
Figure 3-2 Images of representative fabricated single microchannel with micropillar arrays. Optical images of (a) front and (b) backside of a single channel device, (c) shows an inset of the heater and RTD4 metalization on the backside of the test sample, (d) Helium Ion micrograph of the microchannel cross section in the A-A plane, (e) shows magnified view of micropillars.

3.1.2 Multichannel fabrication process

The side walls of the single channel devices were defined by the closed pocket wall of the vacuum insulation gap (shown in Figure 3-2a). The four internal walls that delineate the 5 microchannels from one another were free standing. Following the process plan shown in Figure 3-1, the 5 channels were merged and a single mini-channel device was created. To fabricate multi-channel test samples, the fabrication process was modified as shown in Figure 3-3
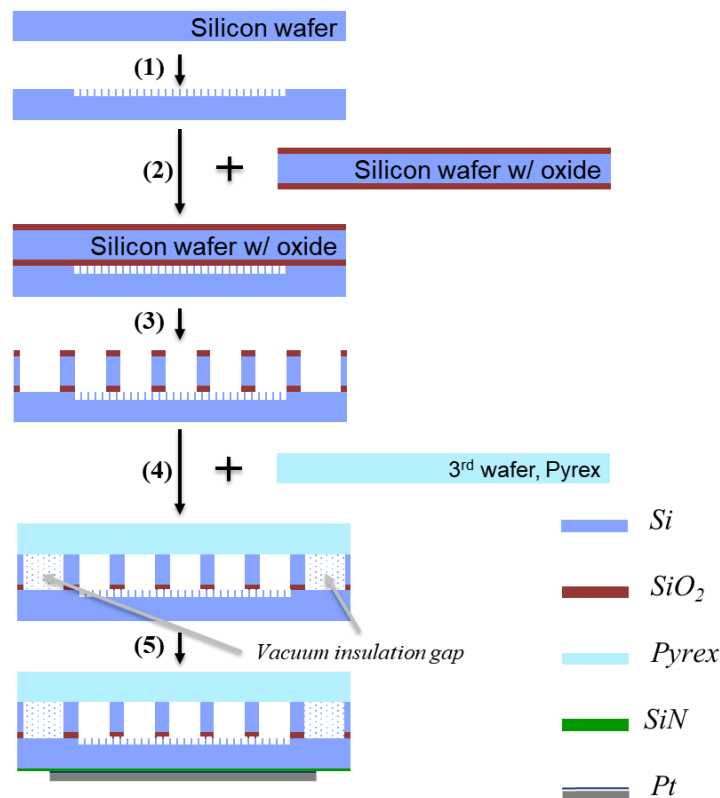
Figure 3-3   Design and fabrication process for multichannel flow boiling devices. (1) Micropillars were etched into a Si wafer using deep reactive ion etching (DRIE), (2) a pristine silicon wafer with a thick oxide layer on both sides was directly fusion-bonded to the micropillar wafer, (3) microchannel and insulating vacuum gaps were etched down to the oxide etch stop, followed by a wet etch in hydrofluoric acid (not shown SiO2 thermally grown, wet etched and then regrown), (4) anodic bonding of a 3rd wafer at vacuum (Pyrex®, Corning) with pre-etched inlet and outlet ports (not shown), (5) a dielectric layer of non-stoichiometric SiN was deposited, followed by a thin film platinum patterned metallization for proxy heater and detectors.

Etching of microchannels after bonding together the silicon wafer stack, ensured that the dividing walls were firmly anchored at all times. To facilitate this change, a pristine polished Si wafer was bonded to the micropillars after 1 µm of SiO_2 was thermally grown. After bonding, the exposed oxide layer behaved as a hard mask for the microchannel/vacuum gap etch. This additional sacrificial layer was needed because the etch was performed on a 2-wafer stack as opposed to a single wafer with a through etch as was done for the original single channel process. The microchannel DRIE etch stopped at the second (buried) oxide layer. This etch stop helped protect the surface and geometry of the critical micropillars. A combination of dry and wet oxide etching was used to remove the remaining SiO_2. The rest of the fabrication process for the multi-channel devices was similar to the single channel process.
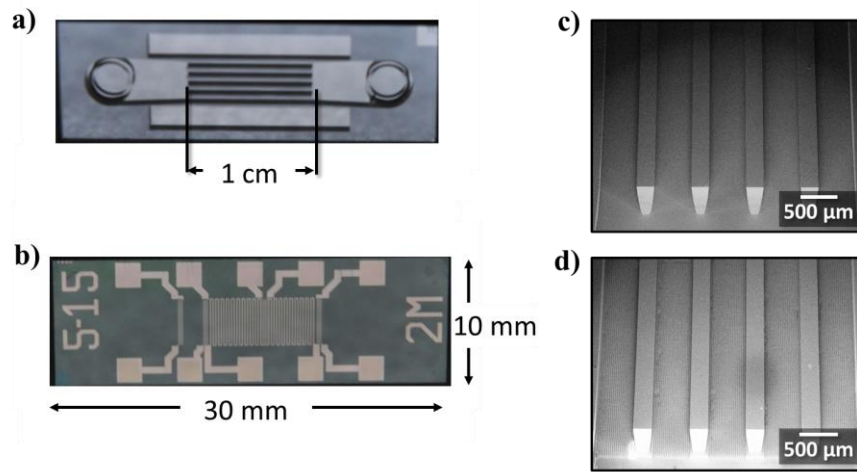
Figure 3-4   Image from a representative fabricated multichannel device. Optical images of (a) front and (b) backside of a multi-channel device. Helium Ion cross section micrograph of a smooth multi-channel (c), and a micropillared multi-channel device (d).

Multichannel devices were only fabricated with a height of 75 µm; results from single channel devices demonstrated that short (25 µm) pillar performed significantly worse than tall (75 µm) pillars with identical pitch and diameter. In order to probe a greater parametric space for the flow boiling enhancement of low surface tension fluids, two additional multichannel devices (medium thin pillars and medium wide pillars) were fabricated and tested with the same intermediate diameter to pitch (solid fraction) ratios (see Table 3-2).

Table 3- 2   Geometric parameters (height, diameter and pitch) of the fabricated multi-channel test devices.

Device	Height, h (µm)	Diameter, d (µm)	Pitch, l (µm)	Solid fraction Φ_s (-)	Surface Area ratio fraction (-)
Smooth	-	-	-	1	1
"dense"	75	5	10	0.196	12.781
"medium thin"	75	5	15	0.087	6.236
"medium wide"	75	10	30	0.087	3.618
"sparse"	75	10	40	0.049	2.473

3.1.3   Fabrication Non-idealities

Probing the importance of capillary wicking required having well-characterized, uniform, and defect-free pillar arrays. Micropillar surface and geometry can be changed by the etch process used to define the micropillars. Figure 3-5a shows a banded defect in the center of every micropillar which resulted from stopping and restarting the Bosch process. Figure 3-5b shows results of a micropillar etch not optimized for prolonged etching needed to achieve high aspect ratios.

The multi-channel fabrication reorders two sequential step of the process and is not preferred. Non-uniformities in dry etch rates were amplified for wafer stacks, especially when multiple oxide layers were present that can charge up and deflect reactive-ions away from their anisotropic intended trajectory. Creating long etch ending near the sensitive micropillars, even with a protective etch stop, was a challenge. Figure 3-5c depicts the uneven etching that occurred.
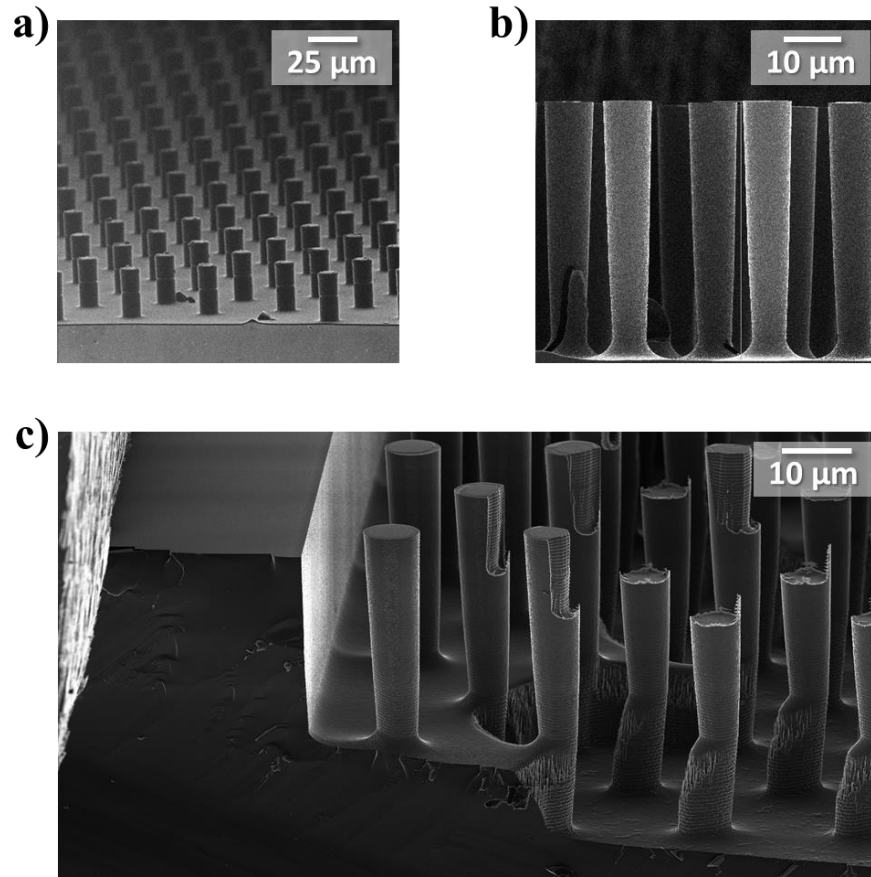
Figure 3-5 Microfabrication non-idealities. Helium ion micrographs of (a) central band defect due to the halting and restarting of the Bosch process, (b) tapered etching at high aspect ratios, (c) masking failure/pillar degradation from very local over-etching of the hard mask and prematurely exposing micropillars.

3.1.4 Device calibration

Photolithography and deposition can lead to variations between wafers, as processing tool performance can be highly sensitive to differences in fabrication conditions or simply change over time. Features designed to be identical on the same wafer can also vary due to spatial differences inherent to processing. Due to these variabilities, every sample needed to be calibrated before a boiling experiment was performed. The custom RTDs were calibrated in a temperature-controlled oven using an ultra-precise Air/Gas Pt100 RTD

sensor as a reference point. Prior to calibration, to avoid resistance drift, samples were annealed at 400°C for two hours. Thermocouples used in the system were also calibrated in a circulating water bath (Lauda Eco, Lauda-Königshofen, Germany) using a Precise Immersion Pt100 RTD sensor as the reference point. Test samples were not immersed in the bath to avoid contaminating them. Instead, resistances of RTDs and heater were measured using cDAQ modules (NI 9216/9217, National Instruments, Austin, TX) designed specifically for RTDs, with nominal resistance range of 10^2 Ω and 10^3 Ω, respectively, and 1 mA current excitation for each channel. The oven was heated, starting from room temperature to at least 120°C, in increments of ~25°C.

At each temperature set point, the oven was allowed to remain for a minimum of 2 hours to reach thermal equilibrium before temperature and electrical resistance data were recorded. A linear regression was performed to calculate the heater and each RTD's temperature as a function of resistance (shown in Figure 3-6). Calibration resulted in less than 0.5 K deviation between the measured resistance and the linear fit.
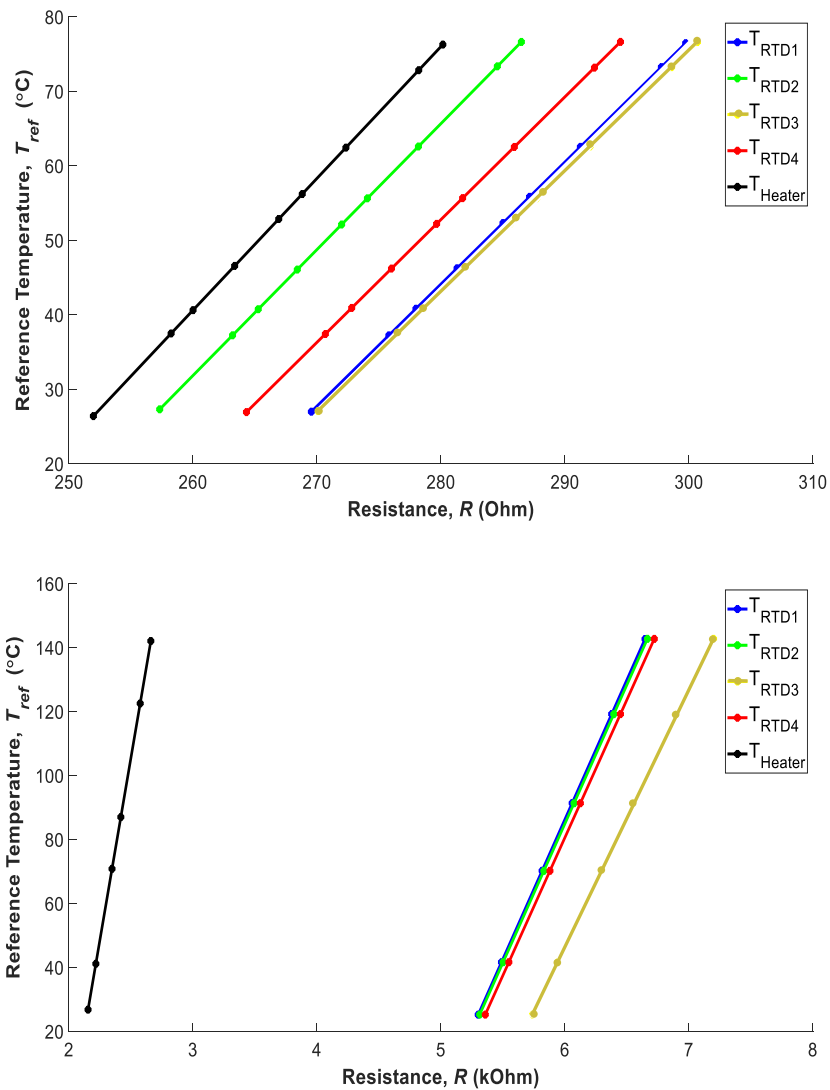
Figure 3-6 Sample calibration results (temperature vs. resistance) of RTDs on (a) single channel device and (b) multi-channel devices. Symbols are the measured data, and lines are linear fits. Each coefficent of determination was minimally 0.99.

The nominal resistance of the single channel RTDs was 280 Ω. The wiring of the heaters for the multi-channel devices used were of the same trace size and pattern. They snaked from beneath the channel on one side of the device, across the die to end beneath the channel on the other side of the device, and covered an area ~16x larger than the single channel. The nominal heater resistance for the multichannel samples were a few kΩ.

3.2 Experimental Setup

A chemically compatible, closed loop test rig to characterize the microchannel flow boiling test devices operating with low surface tension working fluids, was designed and developed (Figure 3-7). Polymeric parts were minimized to prevent leaching of plasticizers into the working fluid; plasticizers are soluble and non-volatile additives that are introduced to tailor material properties and can aggregate on evaporating surfaces. Wherever possible, gaskets, O-rings, and thread seal made of 99.9% indium metal or silver-plated copper were used.
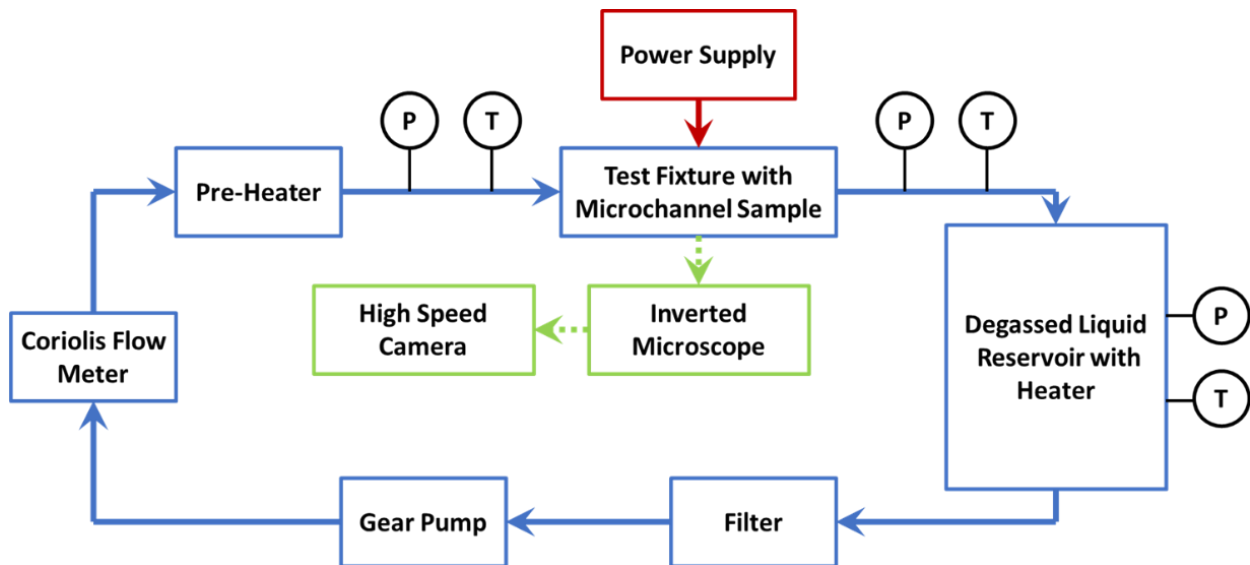
Figure 3-7 Schematic diagram of the custom-made, low surface tension compatible flow boiling loop used in the study. The loop consisted of a degassed liquid reservoir, a microgear (fixed-displacement) pump to provide a constant flow rate, a valve for flow stabilization, pre-heaters to minimize subcooling, a test fixture to interface with the test device, and various sensors. P and T indicate pressure and temperature sensors, respectively.

Throughout the boiling experiment, methanol in the liquid reservoir was maintained in a degassed state and was heated to maintain a nominal pressure in the loop (pressures of 50, 100, and 160 kPa were used). After leaving the reservoir, methanol was passed through a 2 µm inline filter to remove nonsoluble contaminants. To avoid contamination of the working fluid, methanol was then pumped through a loop, using a micro

gear pump (Micropump GA-T23-JFS.E, Idex, Lake Forest, IL). A Coriolis flow meter (M14-AAD-22-0-S, Bronkhorst, Ruurlo, Netherlands) was used to measure mass flow rate. Preheaters upstream of the low thermally conductive Ultem fixture were used to control subcooling of the flow entering the device. The mass flux, G, chosen for this study was nominally 200, 300, and 600 kg/m^2s, with an inlet subcooling of ~1 K. Flow instabilities were expected to be most severe at these low values. For flow stabilization within the loop, a bellows-sealed metering valve (SS-4BMW-VH, Swagelok, OH) was used to create additional hydraulic resistance (at a mass flux of 600 kg/m^2s, this corresponded to a pressure drop in the flow loop of ~10 - 15 kPa for single channel experiments, and ~30 kPa for multichannel experiments), so that instabilities resulting from boiling were salient. A fixed valve position, one full revolution open (predicted flow coefficient of $C_v \cong 0.004$), was used for all experiments. Thermocouples (T type, Omega, Norwalk, CT) and pressure transducers (PX319-030A5V, Omega, Norwalk, CT) were used to monitor loop conditions. Microchannel test devices were placed in an Ultem test fixture that interfaced with the loop. The test fixture was placed in an inverted microscope (TE2000-U, Nikon, Melville, NY) and flow pattern was captured using a highspeed camera (Phantom v7.1, Vision Research) at 4-5000 frames/s.

3.2.1 Working Fluid Degassing

For this thesis, HPLC grade water (HiPerSolv Chromanorm HPLC grade, BDH Chemicals, VWR, Pennsylvania, USA), 99.9% pure HPLC grade methanol (OmniSolv, Milipore Sigma, Darmstadt, Germany), and 99.5% HFE 7000 (trademarked by 3M® as Novec 7000, 3M, Maplewood, MN) were used as working fluids. Noncondensible gasses present in all fluid with appreciable gas solubilities, are known to impact boiling and care was taken to ensure that the pure liquid was never in contact with those gasses. Methanol has a higher solubility for common gasses present in air such as CO_2, O_2, N_2 [67]. With both water and dielectric fluids, dissolved gasses have been shown to increase the heat transfer coefficient, particularly at lower heat fluxes. Dissolved gasses lower the wall superheat needed for partially developed nucleate boiling [68]. Near superheated surfaces the local solubility of dissolved gasses decreases and their

release behaves like a seed bubble triggering nucleation at a lower temperature. Contrary results have also been demonstrated. In order to remove any influence of dissolved gasses on flow boiling performance, which can vary from day-to-day or for sample to sample, the working fluid was always kept degassed. Henry's Law correlates the concentration of a particular gas in solution to the partial pressure of that gas. Until there were negligible amounts of dissolved gasses, pressure of the liquid reservoir was higher than the saturation pressure for the liquid at the measured temperature. Repeatedly superheating the liquid and lowering the pressure, caused gas solubility to plummet, allowing for all gasses to leave the tank at vacuum. This procedure was repeated until the measured pressure converged to the saturation pressure at the temperature of the working fluid.

3.2.2   Experimental Procedure

Calibrated samples were triple solvent-cleaned in acetone, methanol, isopropyl alcohol (IPA) and de-ionized water. Samples were subsequently plasma-cleaned in an oxygen environment (29 W at 300 mTorr) for 60 minutes to remove surface contamination, directly mounted into the sample holder, and isolated from the rest of the loop which was maintained in a degassed state. After pumping down the isolated section of the loop containing the sample to less than 0.5 kPa, the rest of the closed degassed loop was reconnected. After setting the nominal mass flowrate and the desired inlet subcooling temperature, the loop was allowed to reach steady state. The system pressure was adjusted from one steady state to another by heating up the tank using the PID-controlled, silicone rubber fiberglass flexible heater (Omega®) wound around the liquid reservoir. Raising or lowering the temperature set point tank correspondingly raised or lowered the nominal loop pressure. Before starting a new boiling curve, the loop was run, with no input heater voltage, for at least one hour, and a single-phase steady state was verified. To minimize the noise of sensible cooling as much as possible, the device inlet temperature was set by PID to result in a 1 K subcool. This resulted in no more than 2 K subcooling on an average across each heat flux condition. Starting at 0.5 W, the supplied power was doubled until onset of nuclear boiling was achieved. The supplied power was increased in 4 W increments. When nearing the critical heat flux (inferred from temperature response or dry spot size and

longevity visualization), power increments were decreased in order to finely resolve the temperature excursions. Once CHF was reached, the boiling curve data was collected again in reverse, incrementally lowering the heat flux in approximately 4 W reductions offset from the values recorded in the heat up direction of the boiling curve. Approaching the cessation of boiling at the lower heat fluxes, the input power increments were decreased to try to capture with increased resolution the onset of boiling instabilities that result from cycling between single- and two-phase flows. At each power set point, one minute of data was collected after 3 minutes to ensure that steady state had been achieved. A summary of data acquisition streams is presented in Table 3-3.

Table 3-3   Data acquisition hardware, measurement types, and sampling rates for flow boiling experiments

DAQ	DAQ Component	Analog signal	System measurement	Sampling rate
cDAQ-9174	NI-9214	temperature	thermocouple	1 Hz*
	NI-9205	voltage	pressure sensors mass flowrate sensor	1 kHz**
NI-PCI-6289	SCB-68A	voltage	RTD voltage drop***	1 kHz**
Phantom v7.1			high speed visualizations	4-5000 fps

* thermocouple response time and hardware limitations limited rate

** up to 50 kHz sampling possible for this hardware configuration

*** high accuracy, RTD dedicated cDAQ modules have a sampling rate limitation of tens of hertz. For high-speed sampling, high-precision, matched reference resistors were put in series with the RTDs. Measured voltage drop was used to determine each resistance

3.3   Data Processing

Analog data was collected at each steady state power input (*i.e.* heat flux) for the different flow conditions listed in Table 3-4. Figure 3-8a shows schematically, the key temporally resolved variables measured at each steady state operating condition. Figure 3-8b shows the location of the four RTDs used to measure

spatially varying backside temperatures. Even though T$_4$, the temperature measured at RTD4, is the furthest measurement taken downstream, because of heat spreading in the silicon substrate, T$_3$ was found to be the highest. For that reason, it was used directly and indirectly as the reference for much of the data analysis. The standard deviation of T$_3$, σ_{T3}, was shown to be a good indicator for the onset of dryout (see Chapter 4). The local heat transfer coefficient (HTC), is defined in this study in relation to that measurement. Being the highest temperature measurement, this ensured a conservative assessment.
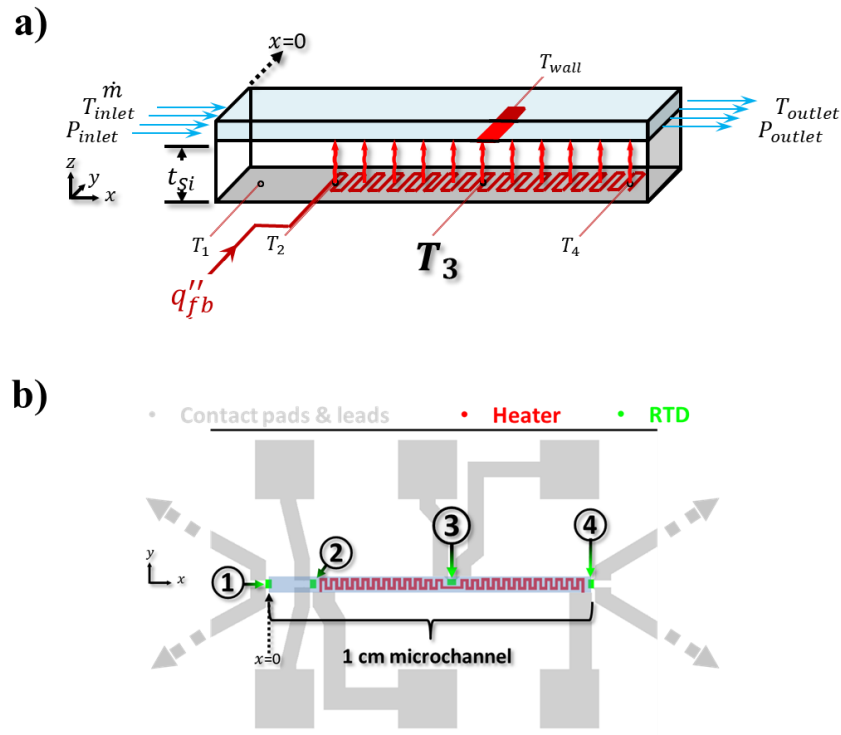
Figure 3-8 Data measurements and reduction. a) Scale schematic for a single channel metallization highlighting the locations of the three RTDs near the microchannel heater and showing the spatially resolved wall temperatures T$_2$, T$_3$, T$_4$. (b) Key temporally resolved dependent variables measured at each steady state operating condition in response to the changing independent variable of input heat flux: i. temperatures at the inlet, outlet, and back side of the microchannel, ii. pressure at the inlet and outlet, and iii. mass flux upstream of the flow boiling device.

Flow boiling heat flux, $q''_{flow\ boiling}$, the key derivative of the dependent variable of each boiling curve, was calculated by dividing the total power supplied to the heater (minus known losses, P_{loss}) from the DC

voltage supply, $Q_{total} = I_{Supply} V_{Supply}$, by the area of the bottom of the microchannel, $A_{footprint} = 500 \, \mu m \times 1 \, cm = 5 \times 10^{-6} \, m^2$. The metallization pattern used for each sample was designed so that the resistance of the leads and contact pads were 5% of total resistance measured on each die. Therefore, only 95% of the power supplied was predicted to have actually reached the microchannel.

Known loss mechanisms for heat being supplied to the microchannel for flow boiling is ohmic heating in the platinum thin film from the contact pads to the actual serpentine heater, as well as conduction losses through the silicon die and into the Ultem® fixture (schematically shown in Figure 3-9a). Though precautionary steps were taken to minimize these conduction losses (*e.g.* use of low conductivity material for the fixture block, insulation of tubing, and incorporation of vacuum insulation gaps within the monolithic silicon device), these losses could not be completely eliminated.
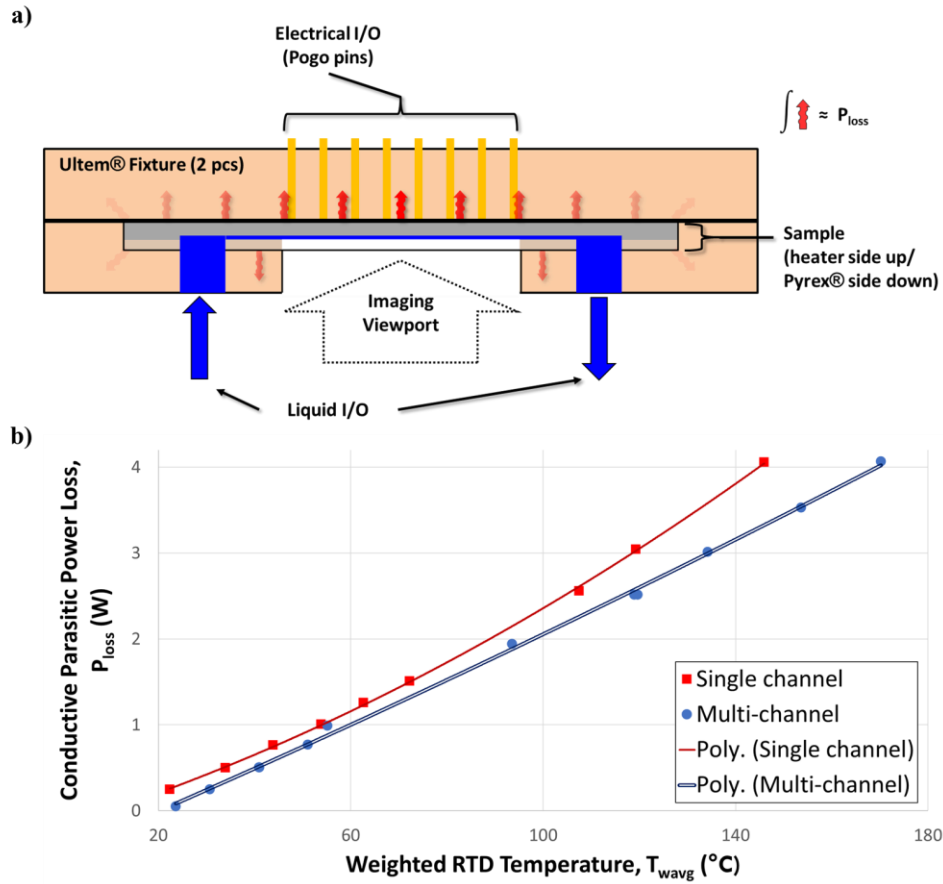
Figure 3-9 Sample holding block and parasitic conduction losses. (a) Schematic (not to scale) of heat flux dissipated by the microchannel device during flow boiling and the inevitable heat loss to the environment, (b) dry calibrated heat loss as a function of average microchannel backside surface temperature T_{wavg} (°C) for single channel devices (red plots) and for multi-channel devices (blue plots). Markers are the measured data; continuous lines are the second order polynomial fits.

$$q''_{flow\ boiling} = \frac{0.95 I_{supply}\ V_{Supply} - P_{loss}}{A_{footprint}}$$

Parasitic conduction losses, P_{loss}, were quantified by determining the steady state power needed to hold a sample, mounted in the testing fixture and piped down to vacuum, at specific temperatures spanning a wide range. A 2nd order polynomial fit (with coefficient of determinization greater than 0.999) was used to define a loss function that accounted for the power unintentionally conducting away from the sample at different temperatures. (see Figure 3-9b). Single channel samples and multi-channel samples had their own loss

functions, due to differences in spreading within the monolithic samples. The loss function defined as $P_{loss} = f(T_{w.avg})$ was found to have the best goodness of fit for the data, as opposed to using the heater temperature T_{heater}, or any one of the RTD measured temperatures. Where $T_{w.avg} = ¼ (T_2 + 2T_3 + T_4)$.

$$P_{loss} = \begin{cases} 1.75 \times 10^{-5} * T_{w.avg}^2 + 2.39 \times 10^{-2} * T_{w.avg} - 0.52 & \text{for a single channel device} \\ 2.41 \times 10^{-5} * T_{w.avg}^2 + 2.12 \times 10^{-2} * T_{w.avg} - 0.45 & \text{for a multihannel device} \end{cases}$$

The inlet subcool, $T_{Subcool}$, was defined as:

$$T_{Subcool} = T_{Channel} - T_{inlet} \cong 1\,K$$

where the saturation temperature of the device $T_{Channel}$ is the saturation temperature for methanol at the average pressure measured at the inlet and outlet of the device:

$$T_{channel} = \begin{cases} \frac{T_{outlet} + T_{inlet}}{2} & \text{for } 1\Phi \\ T_{Saturated\ Methanol}\big|_{@P = \frac{P_{inlet} + P_{outlet}}{2}} & \text{for } 2\Phi \end{cases}$$

The effective local heat transfer coefficient (HTC) was defined as:

$$HTC = HTC\big|_{@x = 5.8\,mm} = \frac{q''}{T_{wall} - T_{Channel}},$$

where T_{wall} is the extrapolated temperature at the bottom of the microchannel, assuming 1-D conduction of the effective heat flux through the Si substrate from centre temperature of the RTD located at 5.8 mm downstream of the inlet. The exit quality (x_{exit}) was calculated as the quality at the outlet, assuming that all of the steady state power accounting for conduction losses was used for sensible cooling to the saturation temperature and then for vaporization:

$$x_{exit} = \frac{\frac{q''_{flow\ boiling} A_{footprint}}{\dot{m}} - c_p T_{Subcool}}{h_{fg}},$$

where $\dot{m}$ is mass flux measured upstream in the flow loop, and c_p and h_{fg} are the liquid specific heat and enthalpy of vaporization of methanol at the given device saturation temperature.

Summary of experimental test conditions for boiling curves collected for this study is presented in Table 3-4.

Table 3-4　Flow boiling loop conditions used in this study

Working fluid	Nominal pressure [kPa]	Mass flux [kg/m²s]	Sample set
~ 1K subcooled Methanol	50	200	Single channel Multi-channel*
	100	200	Single channel
		300	
		600	
	160	200	Single channel

* Due to the high resistance of the multi-channel, an excess of 400 V was needed to be applied to demonstrably reach CHF. This was critical in the regime where the deposited dielectric layer broke down. At higher flowrates, data collected for the boiling curve would become incomplete. At higher pressures, the higher saturation temperatures caused higher heater resistance, and also resulted in incomplete boiling curves.

Chapter 4- Microstructured flow boiling of methanol

In this chapter, I will first discuss the qualitative visual differences in methanol flow boiling behavior in single smooth microchannel, and then compare them to flow boiling behavior in single structured microchannel devices with micropillar arrays. Images and videos of bottom heated surfaces were used to investigate the role of surface structures in annular regime where the capillary wicked thin-film stabilization-based performance enhancement was hypothesized to occur. Differences in flow behavior at lower heat fluxes and earlier boiling regimes were also examined to gain mechanistic understanding of the presence of micropillars using the fluid coolant methanol, a fluid with a significantly lower surface tension than water. Next, thermohydraulic performance of each single-channel sample type was characterized, with an emphasis on critical heat flux (CHF), heat transfer coefficient (HTC), and dryout behavior/boiling stability. Finally, I have compared the different behaviors of structured surface microchannels using the wicking model, described in Chapter 2.

4.1   Visual boiling behavior in smooth microchannels

The development of boiling regimes in the smooth microchannels containing methanol, was markedly different from water flowing through microchannels of similar geometry and mass flowrate [29]. Flow boiling water in a 1 cm long, 500 µm square microchannel with 10 K subcooled water following at a mass flux of 300 kg/m^2s reached a boiling pattern prior to CHF (or upon reaching an excessively high cut-off heater temperature), that alternated between churn flow and annular flow. Figure 4-1 shows the progression of boiling regimes of methanol with increasing heat flux (from left to right) using the same operating conditions, except for subcool which was minimized to cover a larger range of exit vapor qualities.
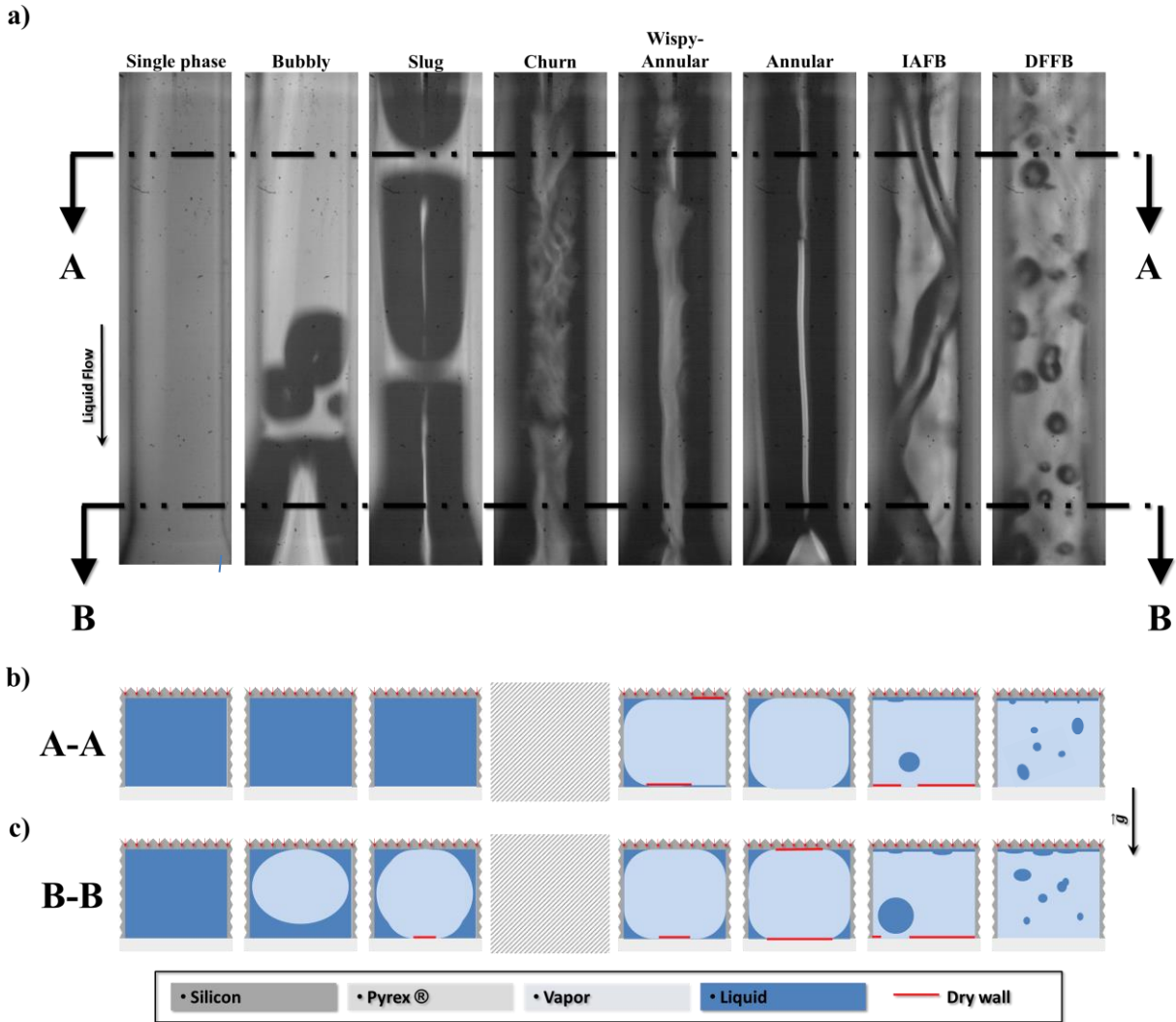
Figure 4-1   Representative flow patterns of methanol flow boiling in a smooth 500 μm square microchannel. a) Photographic representation of each of the boiling regimes observed for the smooth microchannel with ~1 K subcooled methanol and a mass flowrate of $300\,\mathrm{kg/m^2 s}$. Schematic representation of two cross sections taken at b) 2.1 mm from the outlet A-A, and c) 0.94 mm from the outlet B-B. Each schematic shows the wall closest, and parallel, to the heater at the top, and the transparent Pyrex® viewing channel wall at the bottom, as per the experimental conditions, where gravity is point straight down. Schematics shows roughly where vapor and liquid were observed, even if just transiently.   Locally dried out sections of the top and bottom channel walls were defined whenever strong visual confirmation was available. Churn flow had numerous liquid vapor interfaces that translated axially along the channel, making it exceedingly difficult to suggest where/when there was a particular phase of the methanol, and so no schematic was attempted.   For both film boiling regimes, careful observation of the flow behavior confirmed that the out of focus background texture, found behind the dark outlined liquid droplets and threads, is actually a reflection of a liquid film that is traveling adjacent to the Pyrex®, off of the smooth Si heated 'top' surface.

46

Both water and methanol produced alternating regimes of churn flow, wispy-annular flow and annular flow (shown in the 4th, 5th, and 6th columns in Figure 4-1). The most notable visual difference between the boiling behavior of methanol was that, unlike water, methanol developed into Transition Flow/Inverted Annular Film Boiling (IAFB) and Dispersed Film Flow Boiling (DFFB). The liquid film in the annular flow regime would intermittently dry out at the center of the channel bottom. Instead of simply rewetting, as the heat flux was increased, the translating, ruptured, annular-film would start to bead-up and flow like a liquid thread as it traveled down the microchannel to the outlet plenum. Eventually, the liquid would start to detach from the walls and travel in the center of the microchannel. As the heat flux increased, the liquid thread spent more and more time traveling in the center of the channel than touching peripherally the channel wall; the channel wall was left in direct contact with a low thermal conductivity vapor layer. If the liquid were to permanently lift-off and travel only in the core, then the flow would be known as Inverted Annular Film Boiling (IAFB). Due to the viewing angle, there was no discernable way to determine whether the liquid core was in contact with the channel or not. However, the gradual increase in temperatures of the channel, instead of a large thermal runaway, indicated that there was some transient liquid contact with the channel bottom. The abrupt disruption of the liquid core quickly transitioned to a Dispersed Film Flow Boiling (DFFB) mode/mist flow. This change in the observed flow behavior was accompanied with a large temperature excursion (> 30 K). Figure 4-2 shows the progression from IAFB to DFFB.

Interestingly, although the published literature suggests that IAFB results from specific operating conditions, but those operating conditions were not used in the present experiment. Lee and Mudawar (2009) defined microchannel flow boiling as having two different CHF mechanisms: 1. for saturated flow boiling, it is wall dryout at the end of annular flow, and 2. for subcooled flow boiling, it is the Departure from Nucleate Boiling event (DNB); the latter results in an inverted annular flow. Ghiaasiaan (2017) reported that IAFB film boiling behavior was a result of high heat fluxes, high mass fluxes, high subcooling, and/or low vapor qualities [69]. The regime transition shown in Figure 4-1 are not from high subcooling, the key differentiator used by many authors for the horizontal flow boiling annular flow inversion. This is

easily corroborated by the development of significant sections of slug, churn, wispy-annular flow regimes; these are not seen in very subcooled flow boiling.

$\overrightarrow{flow}$

$q'' = 477\ ^W/_{cm^2}$ *Inverted annular flow*

t = 0 ms

t = 4 ms

t = 74 ms

t = 78 ms

t = 129 ms

t = 133 ms

Mist flow
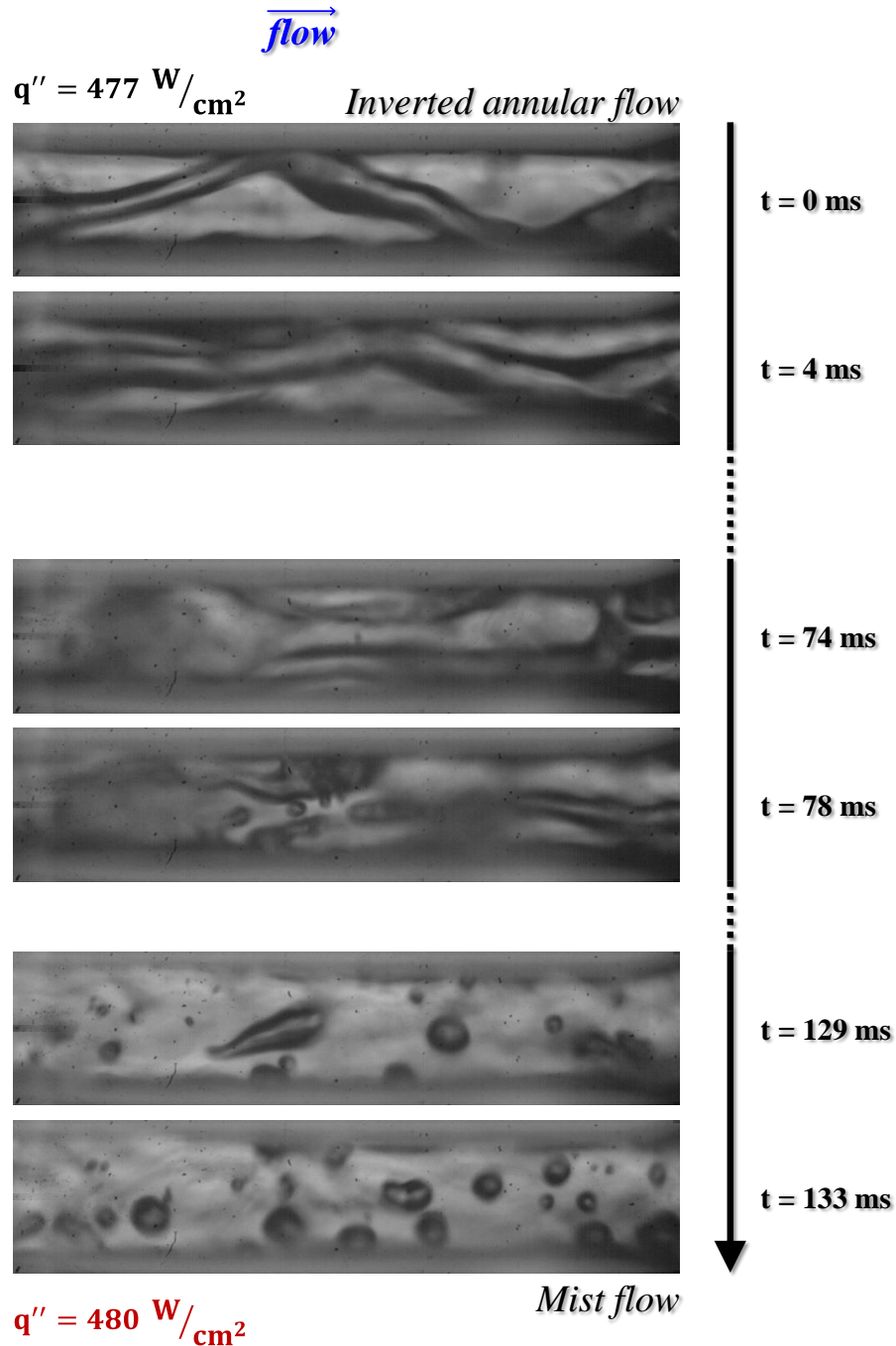
$q'' = 480\ ^W/_{cm^2}$

Figure 4-2   Flow evolution in time for flow boiling of methanol at thermal runaway. Time-lapse images were recorded at the end of smooth microchannel. Thermal runaway triggered between heat fluxes of $q'' = 477\ W/cm^2$ to $480\ W/cm^2$. This resulted in dispersed film flow boiling (mist flow).

4.2 Thermohydraulic characterization of smooth microchannels

The boiling curve for a smooth channel device is shown in Figure 4-3 ($300 \, \text{W/cm}^2$). It is a representative case with a minimal subcooling of ~1 K. The corresponding observed boiling regimes are also shown.
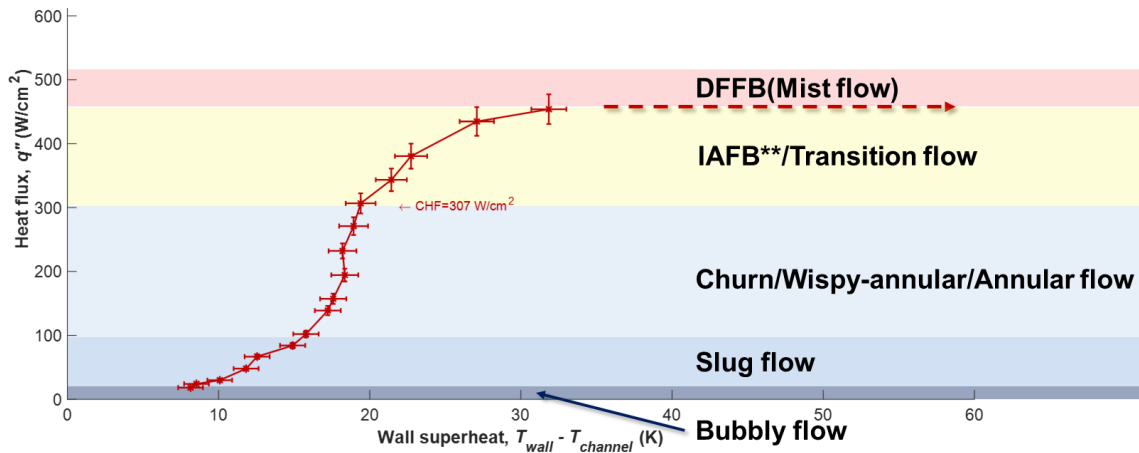
Figure 4-3   Boiling curve (heat flux vs. wall superheat) for methanol in a smooth microchannel. Visually distinct boiling regimes are labeled in the plot. Mass flux, $G = 300 \, \text{kg/m}^2\text{s}$ with an inlet subcool, $\Delta T_{sub} \leq 1$ K.

Additional important metrics helpful in characterizing flow boiling performance of a device are: (1) HTC, (2) standard deviations of the temperature (T_3 measured at the hottest RTD), and (3) pressure drop across the microchannel for each non-transient state/fixed heat flux data point on the boiling curve. The observed flow behavioral change that occurred at ~$300 \, \text{W/cm}^2$, with the onset of transition flow/IAFB, was also seen in the temperature standard deviation σ_{T_3} (Figure 4-4a), the HTC (Figure 4-4b), and pressure drop standard deviation, $\sigma_{\Delta P}$.
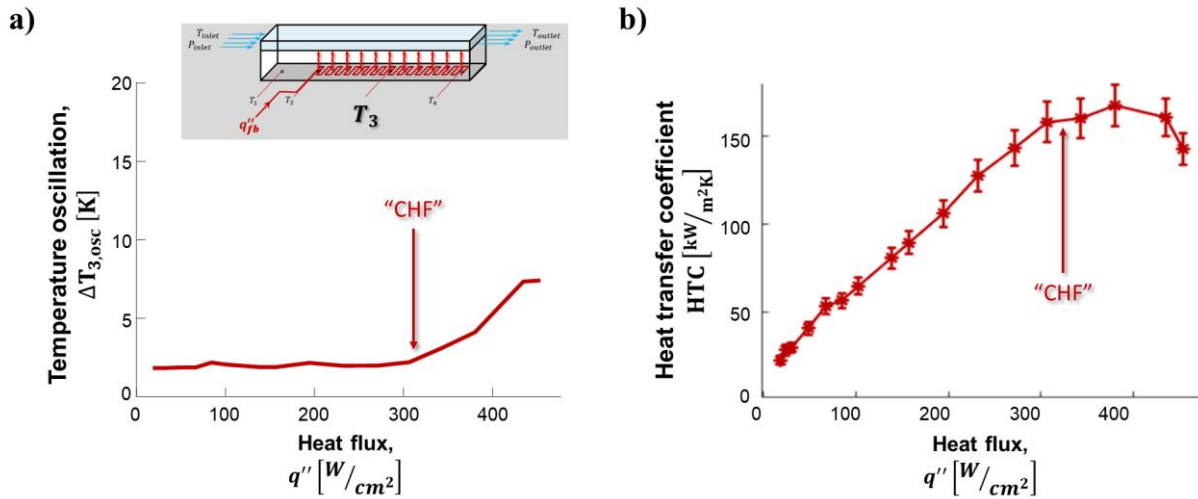
Figure 4-4   Temperature oscillations and HTC as a function of heat flux for boiling in a smooth microchannel. Visual start of inverted annular flow, *i.e.* liquid traveling in the center of the microchannel, is labelled as CHF in each plot. Corresponding to significant dry-outs was noticeably larger temperature swings and plateauing of the HTC. Mass flux, $G = 300 \, \text{kg/m}^2\text{s}$ with an inlet subcool, $\Delta T_{sub} \leq 1 \, \text{K}$.

4.3   Visual boiling behavior in microstructured microchannels

Table 4-1 summarizes key information collected from the high-speed visualizations of boiling in microstructured microchannels.

Table 4-1   Key observations of flow boiling in microstructured microchannels

Microstructured microchannels	
Onset of nucleate boiling	Instability markedly worse for all microstructured samples as compared to the smooth device
Nucleation	At low heat fluxes, nucleation at the side walls is dominant as designed
	At higher heat fluxes, nucleation occurring at the sides of the channel could trigger channel wide dryout events

	At highest heat fluxes, nucleation within the pillar array is evident
	    - Dense pillars eventual become permanently dry, worse for short
	    - Sparse pillars dryout locally from nucleation, but rewet

CHF	Permanently dry center of channels for denser pillar arrays, wicking observed but only a few pillar pitches deep
	Traditional annular dryout observed for sparse pillar arrays

4.4 Characterization of flow boiling methanol in microstructured microchannels

The boiling curves for all four structured samples (microchannel with tall and dense micropillars, microchannel with tall and sparse micropillars, microchannel with short and dense micropillars, microchannel with short and sparse micropillars) and for the smooth sample are shown in Figure 4-5.
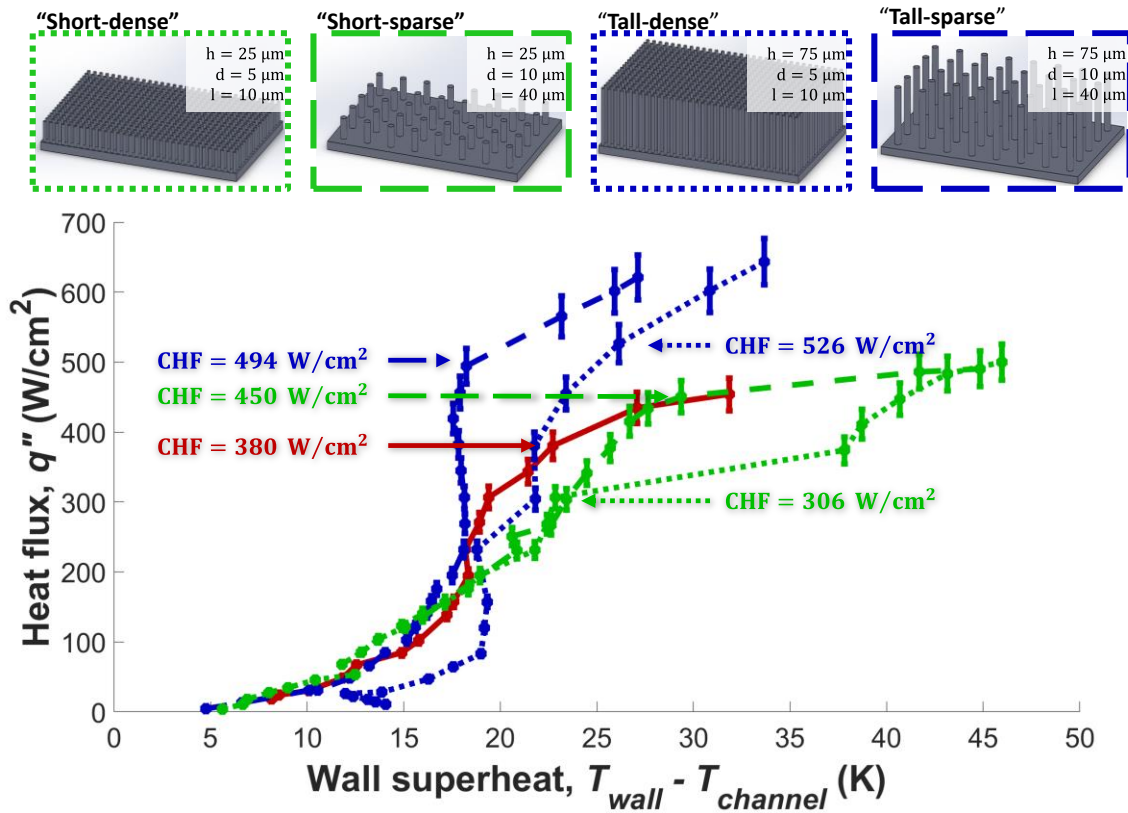
Figure 4-5   Heat flux as a function of temperature rise (boiling curve) of a smooth microchannel (shown in red) and structured surface microchannels with methanol. Mass flux, $G = 300 \, \text{kg/m}^2\text{s}$ with an inlet subcool, $\Delta T_{sub} \leq 1K$. Red solid line, smooth microchannel; blue curves, microchannel with tall micropillars; green curves, microchannels with short micropillars; lines with dashes, sparse micropillars; lines with dots, dense micropillars.

From the five boiling curves shown in Figure 4-5 it is evident that below ~300 W/cm^2, the region where the smooth microchannel had not transitioned to film boiling, micropillar samples are either comparable to

smooth sample, plotted in red, or in the case of tall, densely micropillared samples showed degradation in performance. Observationally, this performance degradation seems to correspond with increased Onset of Nucleate Boiling instability in the microstructured samples, and nucleation events within the microstructures. Above $300\,\mathrm{W/cm^2}$, and after the smooth channel had transitioned to film boiling, the taller micropillared samples, shown in blue, demonstrated performance enhancement over the smooth samples. The shorter samples, shown in green, showed no significant enhancement. And the densely packed short micropillars had an early thermal runaway event at roughly $306\,\mathrm{W/cm^2}$, corresponding to the visual permanent dryout of the center of the microchannel.

Figure 4-6 reinforces the argument that the tall samples had improved performance after the inversion heat flux when compared to that of the smooth sample. At identical heat fluxes the heat transfer coefficient, as defined in Section 3, was measured locally at T3 for structured sample, normalized by HTC for the smooth sample. Another empirical trend seen was the performance difference between the sparse and dense pillars at a fixed pillar height.

4.4.1 Critical heat flux

The critical heat flux for each boiling curve is annotated in Figure 4-5. As was seen in Figures 4-2 and 4-4, CHF for the smooth sample occurred with an inversion of the annular flow, where liquid annulus switched positions with the vapor, previously in the core. There is no obvious indication from the magnitude of the temperature (*i.e.* the wall superheat) alone that CHF had occurred. The pillared samples tended to increase very gradually both the wall superheat and the heat flux dissipated, instead of exhibiting a drastic spike in temperature. Therefore, CHF was defined by the criteria, $CHF \equiv q_i$, where

$$\frac{q_{i+1} - q_i}{(T_{wall} - T_{channel})|_{i+1} - (T_{wall} - T_{channel})|_i} \leq 0.1\,{}^{W}/_{K}$$

and q_i, are only considered if the flow was already in the churn/annular flow regimes. Or simply put, CHF was defined as a heat flux where the slope to the next heat flux of the boiling curve was sufficiently minimal,

and mostly shifted horizontally away from the ordinate, *i.e.* temperature excursion. Besides being a reasonable value based on the shape of the boiling curves, $0.1\,W/K$ was chosen because it was the rate of change for the known departure of nucleate boiling event of the smooth channel.

4.4.2   Heat transfer coefficient

Figure 4-6 shows values of the local heat transfer coefficient, HTC, derived from the local temperature T3 as defined in Chapter 3-3, at a select number of heat fluxes. Each HTC value was normalized to that of the smooth microstructure at the same heat flux. The plot reinforces the argument that the tall samples have improved performance after the inversion heat flux compared to the smooth sample (around $300\,W/cm^2$). Another empirical trend highlighted is the performance difference between the sparse and dense pillars. At a fixed pillar height, sparser pillars in the region of enhancement, exhibited greater enhancement than the denser pillars.
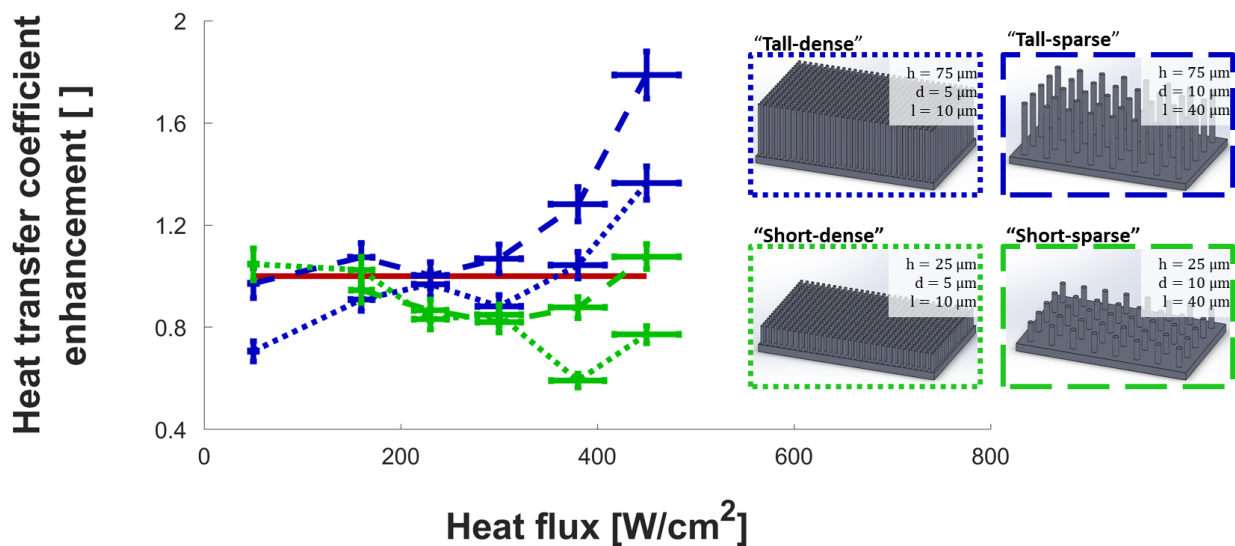

Figure 4-6   Normalized Heat Transfer Coefficient for methanol at $300\,kg/m^2s$. Heat transfer coefficient enhancement as a function of heat flux in a smooth microchannel and structured surface microchannels.

4.4.3 Flow stability

Finally, the stability of the pressure and temperature measurements show sensitivity to transition to film boiling of the smooth sample. After the liquid annulus detached forming a liquid core, the standard deviation of these measurements distinctly increased. This was due to the transient dryout, which caused the temperature to shoot up and eventual temporary rewetting when the liquid core made contact with the liquid, no matter how temporarily. At even higher heat fluxes, the smooth sample might be heated to a temperature above the Leidenfrost temperature, and the standard deviation reversed its trend and started to decrease, due to the fact that it never rewetted and continuously had vapor adjacent to the heated wall.

The microstructured samples, showed a different response from the HTC and CHF enhancements and the pressure oscillations (Figure 4-7b). All these factors were improved for taller micropillars. The temperature oscillations (Figure 4-7a) were improved (lower σ) in the presence of sparely spaced and larger diameter micropillar arrays. Larger pillars spaced further apart maintained a more uniform temperature.

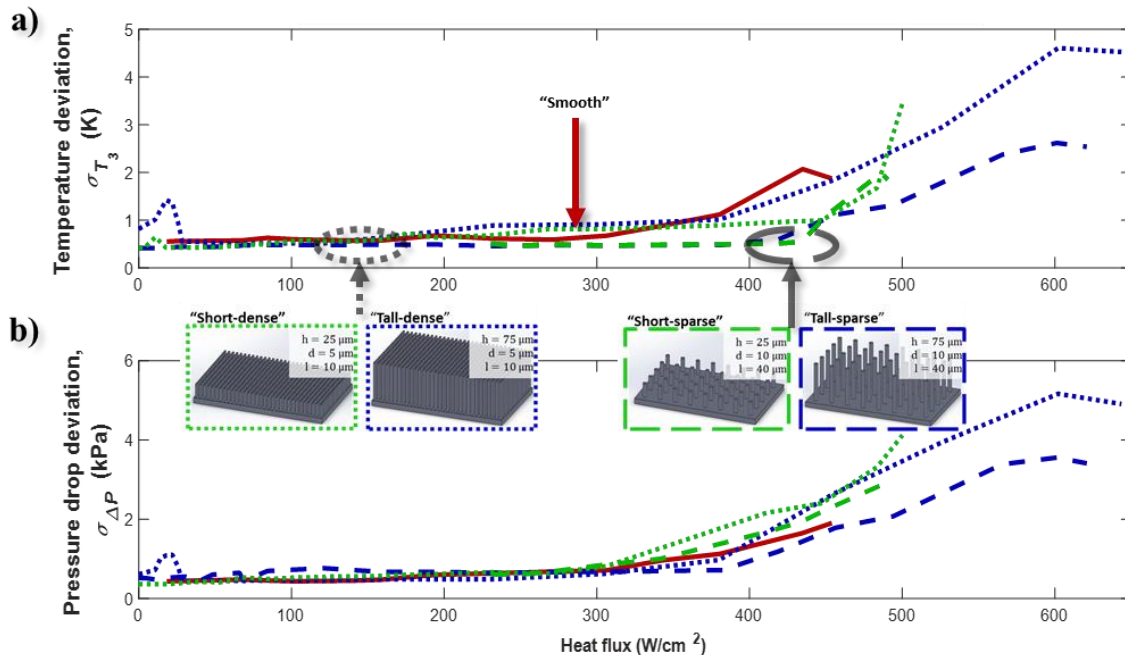**Figure 4-7 Thermohydraulic performance stability as a function of heat flux.** Standard deviations of the a) peak temperature $\left(\sigma_{T_3}\right)$ and b) the pressure drop $(\sigma_{\Delta P})$ across each device at different heat fluxes during the flow boiling of methanol. Mass flux, $G = 300\,\text{kg/m}^2\text{s}$ with an inlet subcool, $\Delta T_{sub} \leq 1\text{K}$.

4.4.4   Pressure drop

The hydrodynamic characteristics of microchannels were studied. As discussed in Chapter 1, high heat flux dissipation with single phase liquid is possible with sufficiently high flow rates of the working fluid. This sort of cooling solution is limited by the excessively high pumping power that would be needed to maintain those high rates through tiny microchannels. It was therefore important to compare heat transfer performance enhancements along with any incurred pumping cost penalties.

Figure 4-8 shows measured time-averaged pressure drop, ΔP, as a function of heat flux q'' for methanol flowing at $300 \, \text{kg/m}^2\text{s}$. The smooth sample performance is shown in red. Pressure drops across all devices were similar within the same order of magnitude. Below $\sim 270 \, \text{W/cm}^2$, additional pressure drops introduced by the surface structures were negligible. At heat fluxes above this value, pressure drops in the structured samples increased. The highest pressure drops for smooth samples occurred at CHF 7.6 kPa. At comparable heat fluxes, the pillared samples had a pressure drop of 9.5-10.8 kPa (a maximum increase of 40%). The pressure penalty was higher for taller structures.

The maximum ΔP at a flowrate of $300 \, \text{kg/m}^2\text{s}$ was 21.5 kPa for the tall, dense pillar array at $q'' = 644 \, \text{W/cm}^2$ (32.2 W). At these conditions, the pumping power needed was very small, $\text{Work}_{\text{pump}} = \dot{m}\Delta P/\rho_l \cong 2.2 \, \text{mW}$, four orders of magnitude smaller than the amount of heat being dissipated.

At lower heat fluxes, structures did not need additional pumping power while they maintained the temperature stability and enhanced heat transfer. These results can be attributed to the liquid-vapor interface only forming menisci within the structures when there was insufficient liquid supply, which is usually at the downstream section of the microchannel. In the devices tested, there was sufficient liquid supply upstream, and majority of liquid was on top of the structures and the structures acted only as surface roughness without introducing any noticeable extra viscous pressure drop. In addition, wicking from the sidewalls to the center of the bottom surface did not contribute to the pressure drop along the microchannel direction.
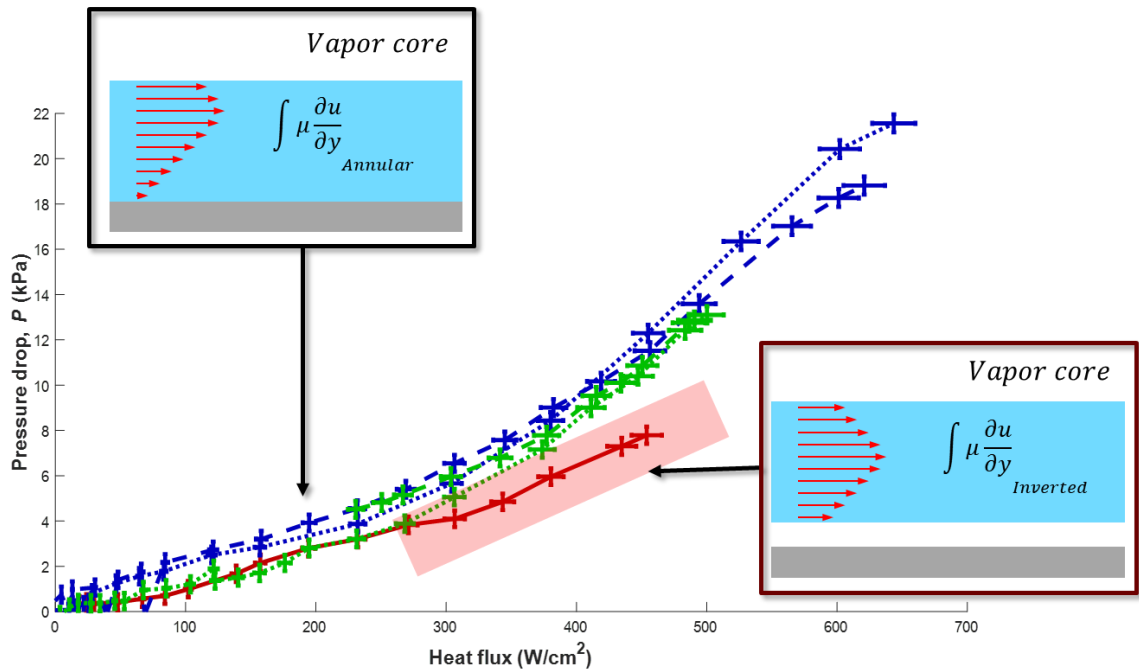
Figure 4-8   Pressure drop for smooth and microstructured single channel flow boiling of methanol at a flowrate of $300 \, kg/m^2 s$ Top left schematic inset of liquid film during annular flow boiling was common to all samples. Bottom right schematic of wall-detached liquid film was observed for the smooth microchannel only. Highlighted in red on the plot, is the pressure drop for the smooth microchannel after detachment was observed. This section of the ΔP vs. q'' plot, was the only significant deviation between the presser drop behavior for all samples.

4.4.5   Study on the effects of mass flux

The critical heat flux enhancements (CHF of a device normalized by the CHF of a smooth device operating at the same flow conditions) for all four microstructured samples are shown in Figure 4-9. As with the initial case for the flow boiling of methanol (Figures 4-5 and 4-6), with a mass flux off $G = 300 \, \text{kg/m}^2\text{s}$, enhancement in the critical heat flux was significant for tall pillared samples, while there was only negligible change for the shorter pillared samples. Also, the maximum CHF enhancement of 85% and 78% occurred at the lowest mass flux of $G = 200 \, \text{kg/m}^2\text{s}$. As the mass flux increased, the enhancement percentage decreased, and by $G = 600 \, \text{kg/m}^2\text{s}$, the enhancement was reduced to 20-40%. For the tall

samples, though only significant at one mass flux, there seemed to be a trend i.e., enhancement was greater for the denser pillar arrays if the height was kept constant.
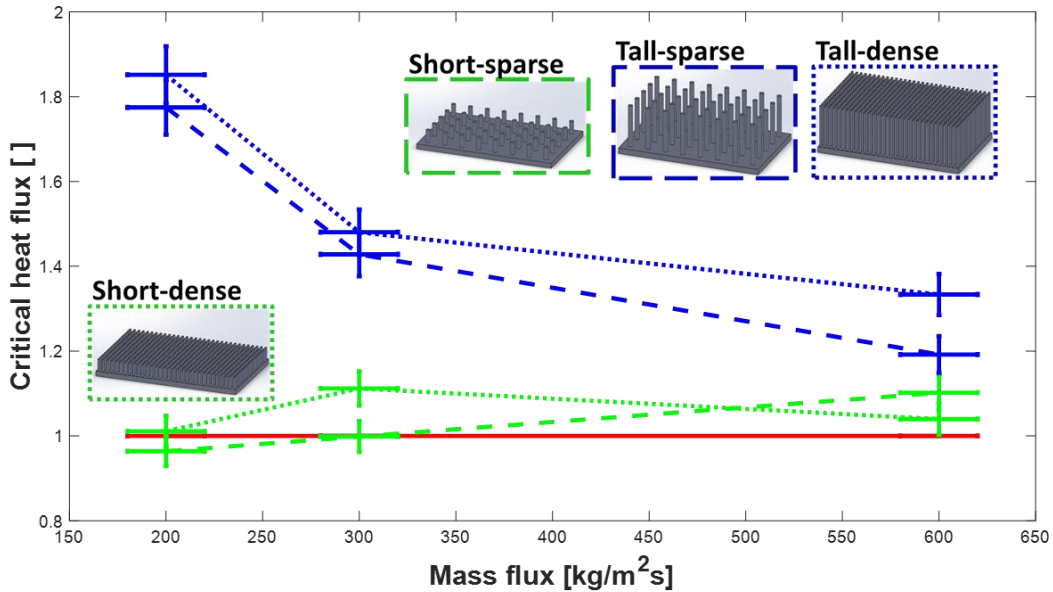
Figure 4-9 Critical heat flux enhancement as a function of three different mass fluxes. Taller pillar samples (plotted in blue) showed significant CHF enhancement, compared to smooth sample, (plotted in red), but this enhancement decreased as mass flux increased. Red solid line—smooth microchannel, blue curves—microchannels with tall micropillars, green—microchannels with short micropillars; lines with dashes—microchannels with sparse micropillars, lines with dots—microchannels with dense micropillars.

4.5 Summary of micropillar effects on single channel flow boiling of methanol

1. Structured microchannel with micropillars are better at heat removal than smooth microchannels only at high heat fluxes.

2. At higher heat fluxes where smooth devices show dry-out, microstructured samples exhibit visually observed liquid films on the heated channel bottom.

3. Smooth microchannels exhibited departure from nucleate boiling at CHF, resulting in inverted annular film boiling.

4. Measured variables for microchannel flow boiling of methanol in a smooth channel confirm transition in flow behavior.

5. Peak (heater center) device temperature started to significantly deviate, due to prolonged dryout, on a time scale long enough to propagate through the substrate.

6. The HTC for smooth device was near its maximum when significant dry-out was observed.

7. Pressure drop after this transition grew at a slower rate with increasing heat flux.

8. Compared to smooth device, onset of nucleate boiling instabilities was greater for microstructured devices.

9. Critical heat flux showed greatest enhancement at lower mass fluxes.

4.6 Interplay of parallel channels during methanol boiling

Since earlier experimental data suggested that methanol enhancement was seen only with taller micropillar arrays, all multichannel structured devices tested had 75 um tall pillars. Also, the kilo-ohm range of the heater resistances, necessitated the operation at the lowest flowrate ($G = 200 \, \text{kg/m}^2\text{s}$) and lowest saturation pressure ($P_{sat} = 50 \, \text{kPa}$). Both operating restrictions helped maximize heat removal through flow boiling and allowed data for a full boiling curve to be collected.

Boiling curves for the three multichannel devices, defined in Table 3-2, are shown in Figure 4-10. The smooth sample, plotted in red, exhibited the same film boiling behavior above a threshold heat flux. This was not seen in any of the microstructured samples. The film boiling inversion occurred at roughly half the heat flux of $\sim 146 \, \text{W/cm}^2$ that was needed for single smooth microchannel. Comparing the three samples, one important thing to note was the more gradual change in temperature values with increasing heat flux, and a significantly less sensitive (shallower) boiling curve. This can be attributed to the design of the heaters which covered all 5 parallel microchannels transversally. This could have averaged out temperature oscillations, absolute temperature readings of dried out channel walls, and made the CHF harder to consistently define. As evident by their overlapping boiling curves within measured error, the multichannel devices with microstructures, identical to the microstructures previously described (tall dense and tall sparse) for the single channel configuration, performed nearly identically and showed enhanced performance over that of the smooth microchannel (at heat fluxes above $\sim 130 - 146 \, \text{W/cm}^2$, at or near the film boiling inversion in the smooth multichannel device). Both devices had a critical heat flux enhancement of over 57%. The sample specifically tested for multichannel operation, plotted in cyan, $[d, h, l] = 10, 75, 30 \, \mu m$, same as the tall, sparse micropillars but with a pitch of $30 \, \mu m$, showed a greater enhancement with respect to the heat transfer coefficient; this sample had an HTC enhancement of 47% compared to the smooth sample (data shown in Figure 4-13).
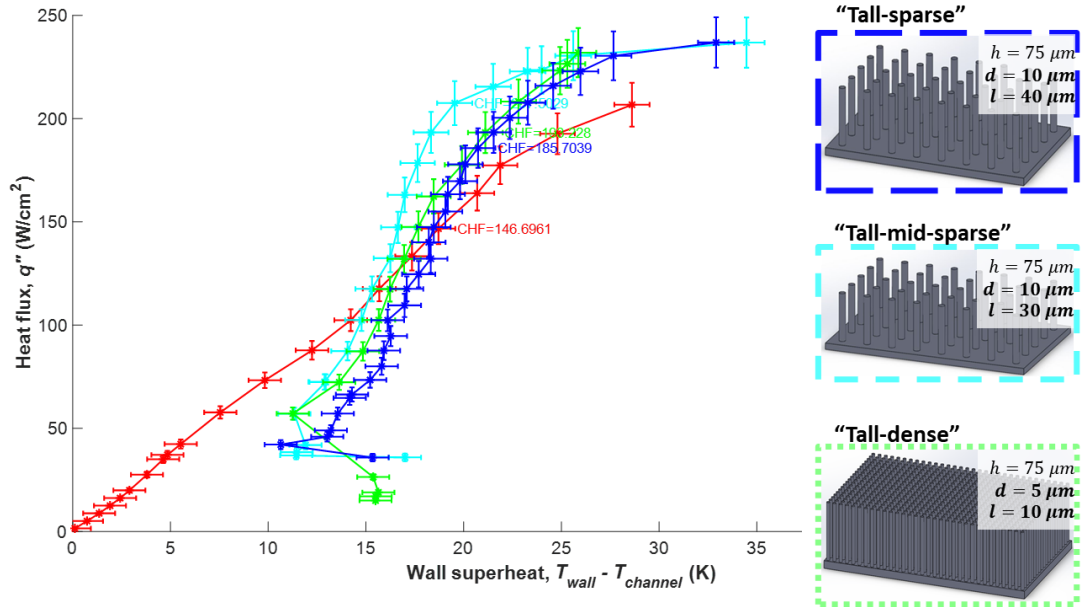
Figure 4-10 Boiling curves for multichannel flow boiling of methanol. Comparison of heat flux as a function of temperature rise for flow boiling in 5-parallel smooth (shown in red) and structured surface microchannels with tall micropillars—sparse (dark blue), mid-sparse (light blue) and dense (green). Mass flux, $G = 200\,\text{kg/m}^2\text{s}$, of methanol, at an inlet subcool, $\Delta T_{sub} \leq 1K$, and a nominal saturation pressure of 50 kPa.
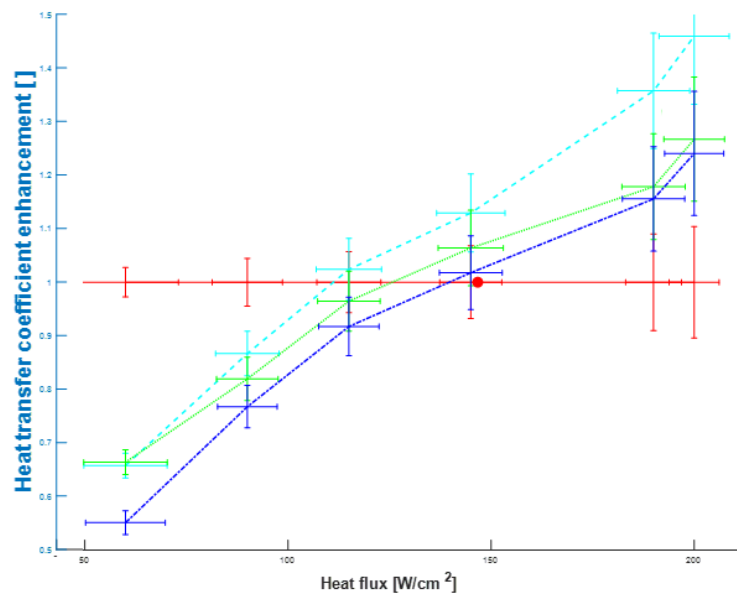
Figure 4-11   Heat transfer coefficient enhancement as a function of heat flux for multichannel devices. Smooth microchannel (shown in red) and structured surface microchannels with tall micropillars (sparse (dark blue), mid-sparse (light blue) and dense (green) distribution). Mass flux, $G = 200\,\text{kg/m}^2\text{s}$, of methanol, at an inlet subcool, $\Delta T_{sub} \leq 1K$, and a nominal saturation pressure of 50 kPa.

60

4.7 Microchannel flow boiling of water and HFE 7000

HFE 7000 experimental results (Figure 4-12) show boiling heat transfer enhancement for the micropillar structured surface (5, 15, 75 µm diameter, pitch, and height, respectively) at a flowrate of 300 kg/m²s and an inlet subcooling of 5 K. HTC enhancement between 15-70% was observed compared to the smooth microchannel flow boiling at heat fluxes below $150 \text{ W/cm}^2\text{K}$. At higher heat fluxes the annular flow stabilization may not be present to offer enhancement over the smooth channel, because the low surface tension fluid did not allow rewetting. At heat fluxes below 60 W/cm^2 pressure drops in both channels were comparable. At higher heat fluxes, the structured channel showed a hydraulic penalty. A CHF enhancement was not observed in the structured channel. Together, these results suggest that capillary flow, at least under some operating conditions, can enhance two-phase heat transfer in microchannels by enhancing the heat transfer coefficient, even when using low-surface tension hydrofluoroethers.
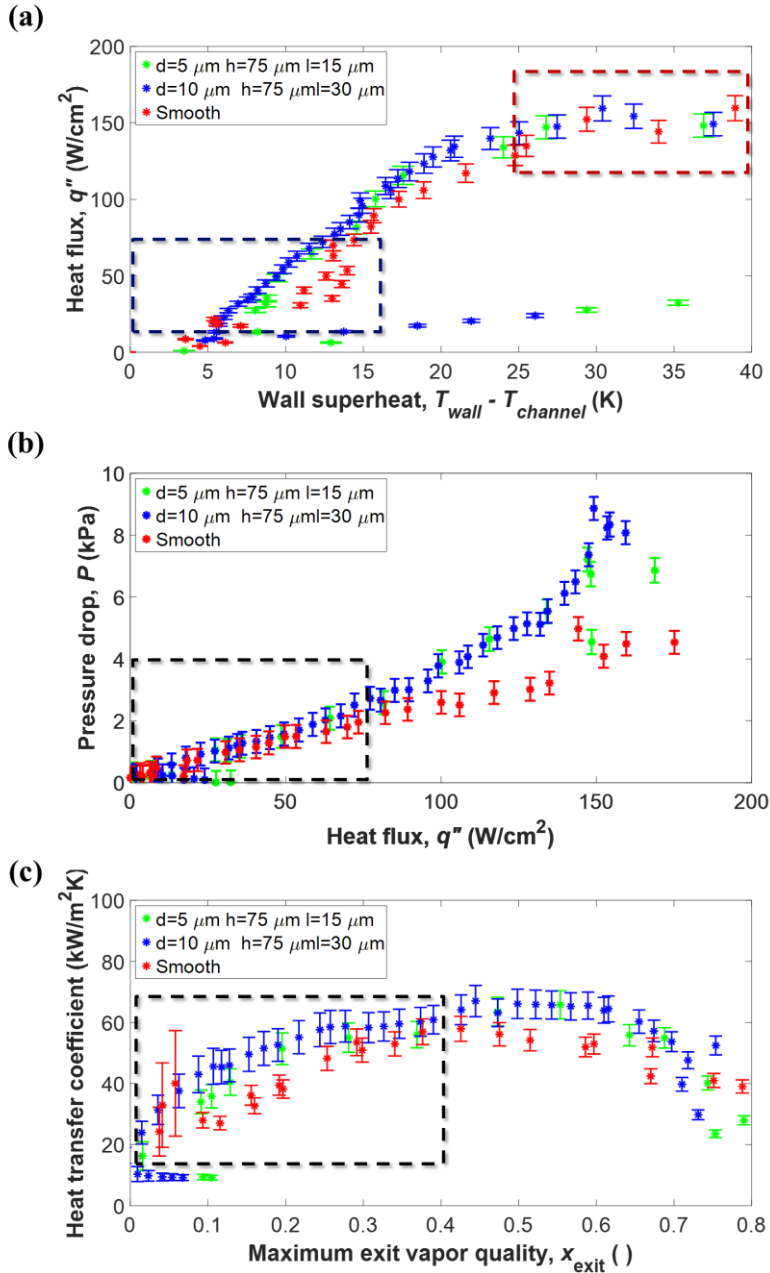
Figure 4-12 Thermohydraulic characterization of single channel flow boiling of HFE 7000. (a) heat flux (b) pressure drop (c) heat transfer coefficient vs. calculated vapor quality at the exit of device, for two devices with tall micropillar microstructures and smooth single channel device (in red); flow boiling pure HFE7000 with a mass flow rate of $300 \ \text{kg/m}^2\text{s}$.

Chapter 5- Mechanistic discussion of flow boiling: comparative fluid performance

5.1 Heat transfer of nucleate boiling

Heat transfer mechanisms available during the ebullition of a single bubble are shown in Figure 5-1.
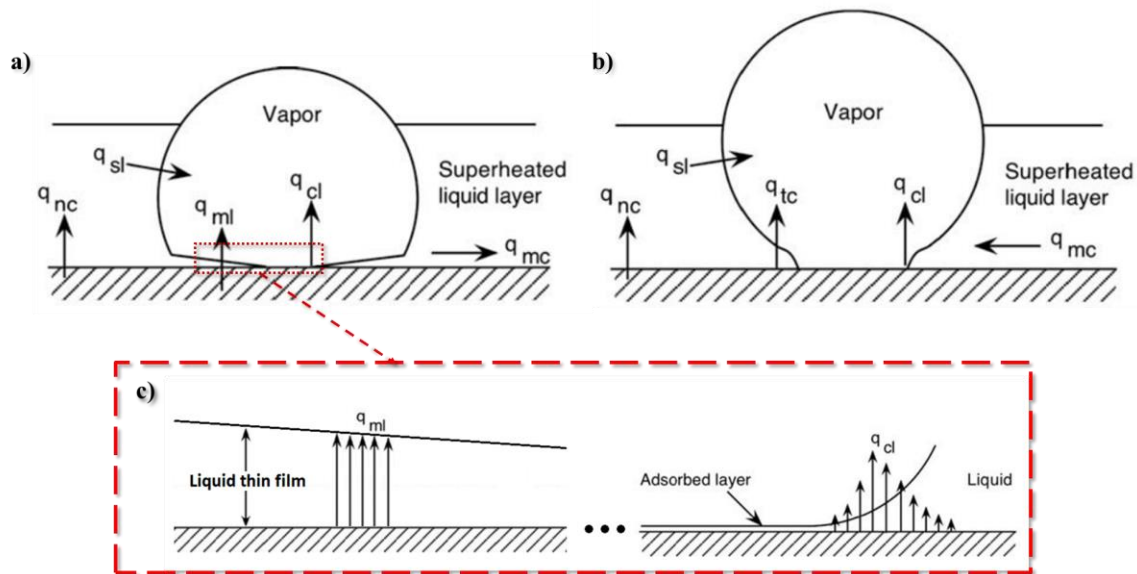
Figure 5-1 **Bubble heat transfer mechanism** during (a) growth and (b) departure. Inset (c) highlights heat transfer through microlayer (q_{ml}) at the three-phase contact line (q_{cl}). (Not shown to scale). Adapted from Kim, 2009 [70].

During bubble growth (shown in schematic Figure 5-1a) and during bubble departure (shown in schematic Figure 5-1b), energy can be added to the bubble and/or dissipated from the wall by:

- natural convection of the liquid, q_{nc}

- evaporation from the superheated liquid (macrolayer), q_{sl}

- thin-film evaporation from below the bubble (microlayer), q_{ml}

- evaporation at the three-phase contact line encircling dry spots, q_{tc}

- microconvection from boundary layer disruption and turbulent mixing, q_{mc}

- transient conduction when dry spots were rewetted/quenched, q_{tc}

The importance of each mechanism has been investigated and debated for many years [70]. Challenges in defining which heat transfer mechanism may be at play and for how long, and correspondingly measured accurately - both spatially and temporally, arise from the microscale, and even nanoscale, nature of boiling.

Recent, experimental work and numerical modeling has helped parse out the relative importance of specific mechanisms during different phases of the boiling process. In particular, micro and nanofabrication advances have made microfluidic MEMS testbeds with high-resolution and high-speed data acquisition. Similarly, advances in visualization methodology, such as high speed optical and infrared imaging, as well as non-contact measurements probing nucleation sites and contact lines, have allowed for better empirical evidence gathering. Kim (2009) summarized many of these findings, and based upon evidence, stated that the predominant mechanism by which heat is removed during single bubble nucleation is from microconvection and transient conduction. [70]. Thin-film evaporation across the microlayer and at the three-phase contact line were of less significance.

Although the above-mentioned studies provide some understanding regarding the mechanism underlying isolated bubble nucleation and ebullition during pool boiling, for practical applications, interaction between bubbles, including wake interactions, and bubble coalescence changes the nature of the heat transfer modes discussed before. Particularly at high heat fluxes, these interactions are what result in limitations, such as the critical heat flux.

Critical heat flux is of utmost importance when it comes to designing and operating systems that use heat-flux controlled boiling. The boiling crisis, *i.e.* the sudden jump in surface temperature that occurs when even momentarily surpassing the heat flux threshold, can result in a catastrophic failure.

Temperature-controlled boiling can only occur in applications when the temperature of the heated solid is strictly limited. This can be satisfied if the heat source itself is a two-phase liquid, and thus at a fixed saturation temperature, or if the heater has a dwindling thermal capacitance and its temperature can only monotonically decrease—something that occurs during quenching. In most industrial boiling applications,

heat flux to the boiler is the controlling variable and is subject to minor perturbations, such as the oxidation rate of a fossil fuel, the criticality of fissile fuel or whether electrical power to an integrated circuit is being drawn during operation. For these applications of heat-flux controlled boiling, determining the critical heat flux, CHF, is crucial when it comes to designing the system, and for setting operational safety limits.

In order to predict CHF values for pool boiling, five different mechanistic models have been proposed: bubble interference, hydrodynamic instability, macro-layer dryout, hot/dry spot, and interfacial lift-off [71]. Figure 5-2 shows schematic representation of each model. The bubble interference model, or critical bubble pack model is depicted in Figure 5-2a. Proposed by Rohsenow and Griffith (2011), this model states that CHF occurs at a heat flux sufficient for isolated bubbles to nucleate so densely that they create a vapor blanket which blocks liquid from flowing onto the heated surface. Their expression for CHF is therefore, derived from activated nucleation site density. Zuber hydrodynamic instability model [72] stated that CHF occurred when the generated vapor traveling perpendicular to the heated surface, reached a critical velocity (see Figure 5-2b). The velocity difference of the upward traveling vapor and the downward traveling far-field/bulk liquid are subject to the Kelvin-Helmholtz instability. The resulting amplitude of the Helmholtz instability would govern the diameter of the vapor column. The pitch between each vapor column can be predicted by the Rayleigh–Taylor instability, resulting from buoyancy of the lower density vapor forming at below the bulk liquid. Columns eventually merge, and create a vapor blanket that prevents liquid from reaching the heated surface.

The hot/dry spot CHF model proposes that the boiling excursion is triggered by the presence of a number irreversible dry spots on the heated surface that can rapidly grow. Examining phenomenological evidence, one of the latest versions of this approach by Jung states that at CHF the radial growth of a dry spot must exceed the heat transfer occurring from the remaining wetted area. This approach results in an expression very similar to Zuber's hydrodynamic model, with an added term for surface wettability. Choi (2016) defined the transition as one requiring two criteria to be met: i) hydraulically- dry spots have to be densely numbered and grow irreversibly to contact one another, and ii) thermally- perimeter of the defined

irreversibly dry spot be above the Leidenfrost temperature. Evidence suggests that this may over-predict CHF since dry spots can become irreversible at temperatures significantly lower than the Leidenfrost temperature.

The macrolayer dryout explanation for CHF is similar to Zuber's hydrodynamic approach, the difference being that instead of requiring a vapor blanket, vapor jets from the heated surface feed into a large hovering bubble. The bubble traps a finite volume of liquid beneath it, defined as the microlayer, and CHF occurs when that evaporation of this layer is faster than the growth and departure of the large vapor bubble. Though this approach has shown some good agreement with predicted CHF and experimental evidence, the underlying description of the system, that of a large hovering bubble fed by vapor columns, has not been observed.

The last approach to CHF is based upon observations of vertical and near vertical boiling. According to this model, near CHF wetting fronts cease to make contact with the solid surface due to the vapor momentum from evaporation, keeping the liquid from making contact and transiently cooling the surface. Figure 5-2e shows the horizontal analogy to this behavior.
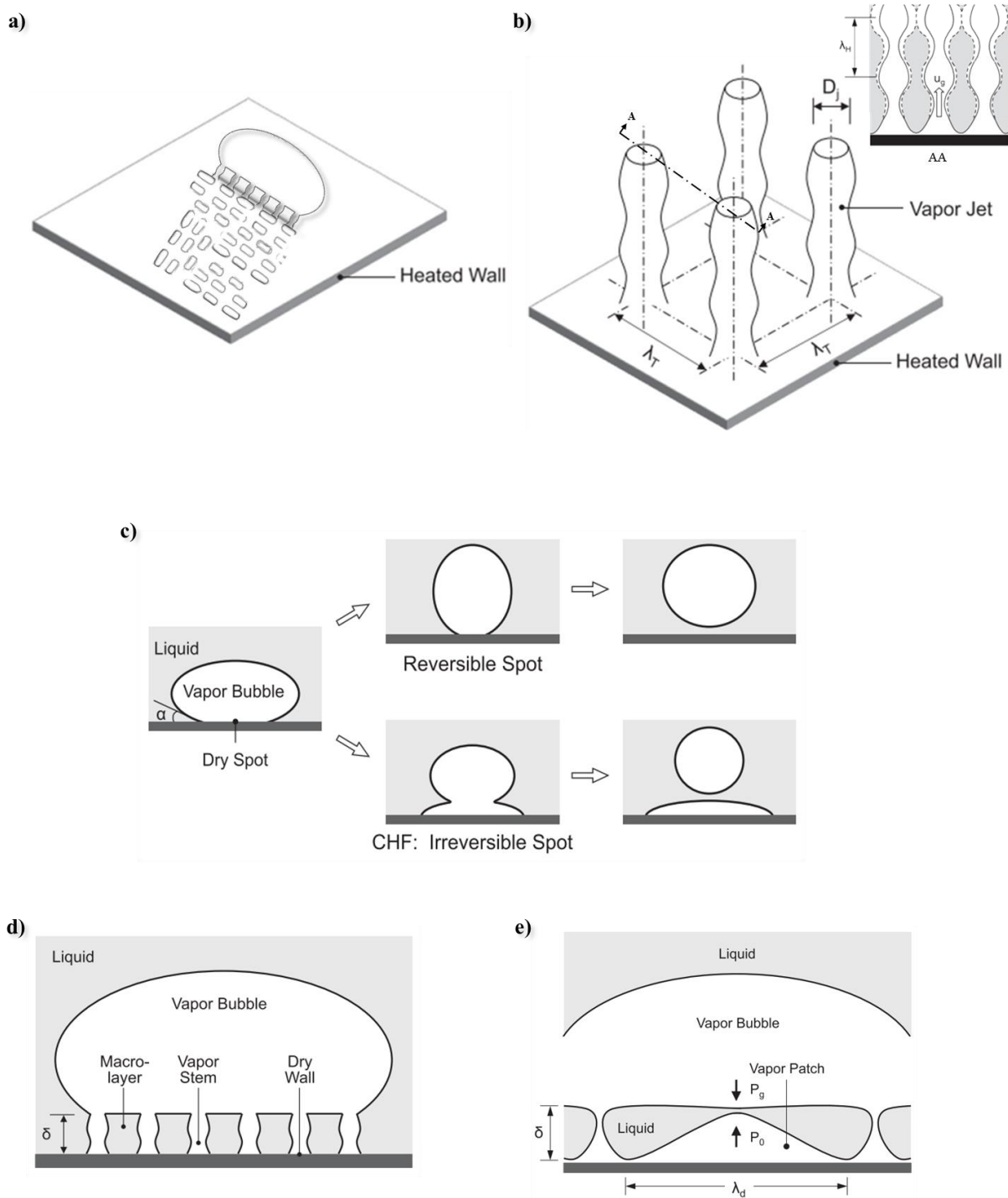
Figure 5-2 Pool boiling critical heat flux mechanisms due to (a) bubble interference, (b) hydrodynamic instability, (c) macrolayer dry-out, (d) hot/dry spot, and (e) interfacial lift-off model. (not shown to scale). Adapted from Liang & Mudawar (2009).

5.2 Flow boiling mechanisms in microchannels

Without agreement on how CHF is brought about in pool boiling, with many arguing for or against each of the above models, consensus for a mechanism for CHF during flow boiling, with the addition of high advection, further complicates mechanistic understanding. Figure 5-3 revisits the microscale flow boiling domains. Differences of note from pool boiling include the additional heat transfer mechanism of a sliding bubble, influences of liquid convection over the heated surface, and the scale limiting hydraulic diameter. Unlike in pool boiling where the bulk liquid could be effectively infinite in thickness, and micro and macro layers might grow somewhat semi-infinitely into that unconstrained space, in microchannels everything stops after D_h.
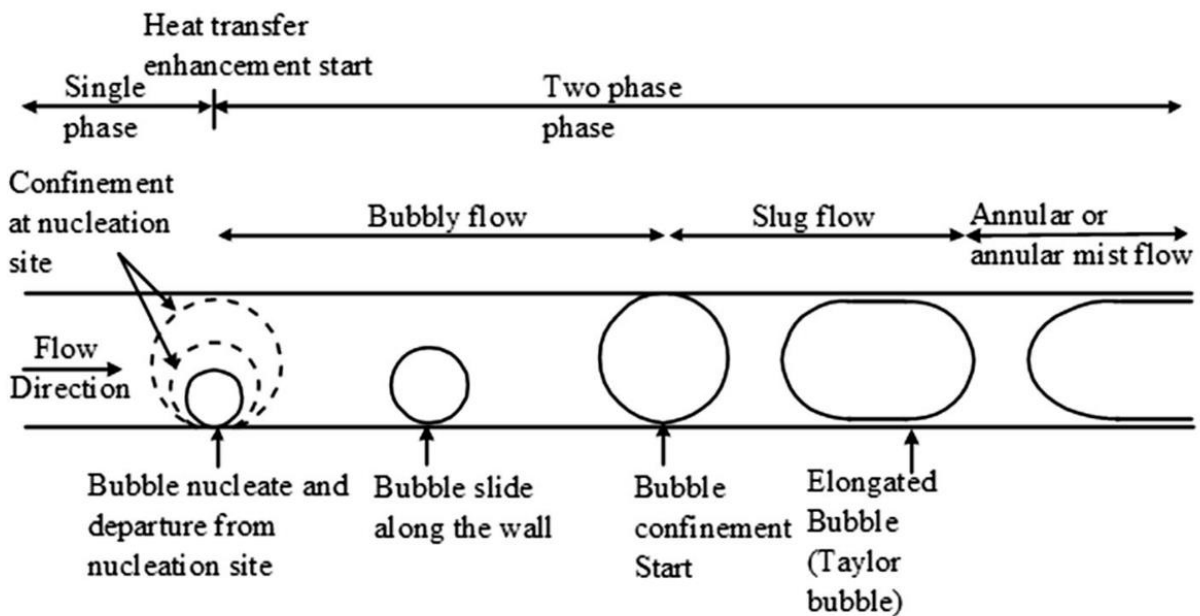
Figure 5-3   Bubble dynamics in microchannel. Adapted from Kadam et. al. (2021).

For flow boiling the thermal runaway can come in two relatively distinct forms, as schematically presented in Figure 5-4. During wall dry-out, the thin liquid film dries up and during departure form nucleate boiling. Formation of a vapor layer impedes efficient boiling, and the liquid core evaporates into the vapor annulus. Lee and Mudawar [18] suggested that saturated flow boiling (with relatively small intlet subcooling or mass

flux) tends to culminate in dry out, while (high) subcooled boiling results in Departure from Nucleate

Boiling, *e.g.* film boiling. Flow conditions alone do not rigorously delineate the two types of CHF, as shown

in this work. DNB can result from minimally subcooled, relatively low mass flux, if certain fluid properties

(low surface tension) and geometries (surface microstructuring, or lack thereof) are met.
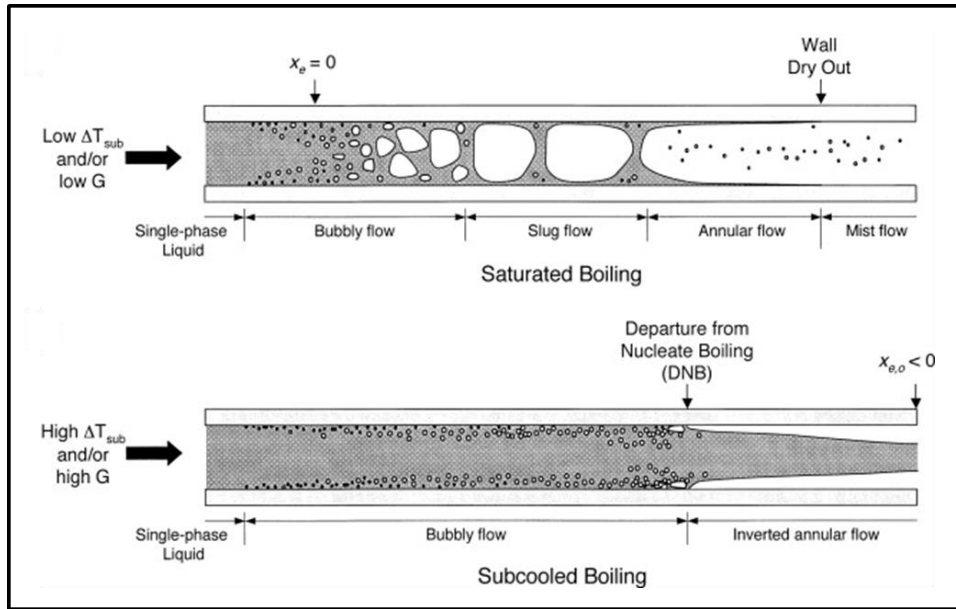
Figure 5-4   CHF classification of flow boiling in uniformly heated channel, as identified by Lee and
Mudawar (2009). (a) dry-out in saturated flow boiling, (b) DNB in subcooled flow boiling [80].

The different mechanisms considered for pool boiling CHF have been mostly extended to flow boiling,

shown in Figure 5-5, but with the addition of fluid advection, and possibly with a different name. Bubble

crowding for flow boiling is the similar to Rosenhow's bubble interference model for pool boiling. The

Boundary-Separation model forms similarly to the hot/dry spot and prevents rewetting. Sublayer dryout

model is similar in premise to the microlayer dryout.
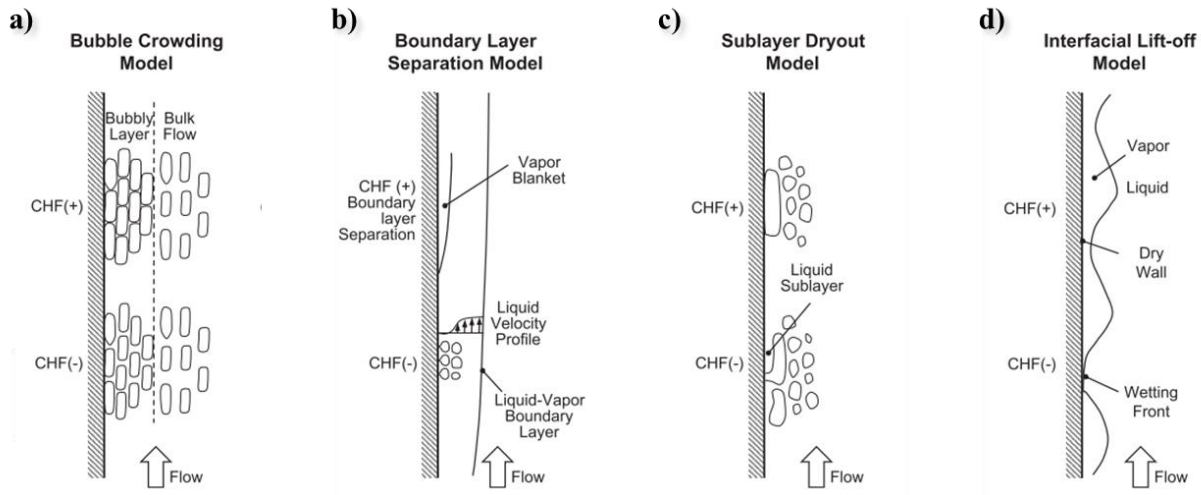
Figure 5-5   Flow boiling critical heat flux mechanisms. (a) bubble crowding, (b) boundary layer separation, (c) sublayer dry-out, and (d) interfacial lift-off model. (not shown to scale). From Konishi & Mudawar (2015).

5.3 Micropillar flow boiling behavior with decreasing surface tension

The various CHF observations for microchannel flow boiling has helped to shed light on the mechanism(s) that might be at play in microstructured microchannels, with an emphasis on the importance of surface tension in the regime at which we can expect CHF to occur. Figure 5-6 schematically summarizes the flow behavior at or/and just beyond CHF for a fixed mass flux of $300 \, kg/m^2 s$, for three working fluids - water, methanol, HFE 7000, in both smooth and microstructured microchannels; behavior described for the micropillars is generically for any pillar sample, as this is a qualitative summary.

Water exhibited typical thin film dryout at the end of the annular flow regime. For the microstructured samples, this regime lasted longer up to a higher heat flux. Methanol in the smooth microchannel exhibited inverted annular flow. There is some uncertainty as to whether the liquid core intermittently made contact with the heated surface or not, similar to the flow-boiling CHF model of interfacial lift-off shown in Figure 5-5d. Microstructred channels near CHF with methanol exhibited no inverted annular flow, and showed

similar dryout behavior as water. One difference was that the transient rewetted state of the micropillars lasted for less time with methanol than for water. In addition, unlike water which can dryout at the center of the channel, methanol started to dryout closer to one side wall. This was probably due to a nucleation event. HFE 7000 demonstrated clear inverted flow for both the smooth and structured samples. HFE 7000 travelled surrounded by vapor and did not appear to make contact with the heated surface. For structured microchannels, some HFE 7000 stayed as liquid within the micropillars and bulk of the liquid traveled in the microchannel as a liquid core.
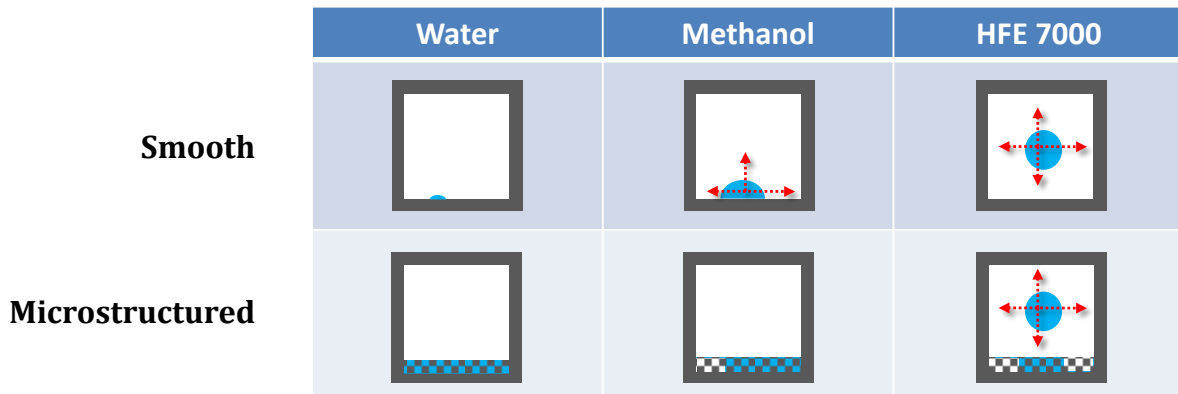
Figure 5-6 CHF/post-CHF flow boiling behavior of three different working fluids with and without micropillars observed in this study

The distinct behavior of the fluid near CHF for each of the working fluids lends credence to the operation of different regimes where certain physics, such as capillarity, might be the predominant determinant factor. To test this belief, scaling analysis was performed for the forces at play in the microchannel.

5.4 Mechanistic understanding of effects

Different mechanistic approaches have been posited to determine CHF values for pool and flow boiling. Understanding the importance of different forces that may be at work during the microchannel flow boiling process, may help better understand CHF and elucidate better strategies to enhance performance.

5.4.1 Scale analysis

Kandlikar et. al. (2013) modified the hydrodynamic instability model, incorporating the effects of heater surface on pool boiling CHF [73], [74], and then extended it to flow boiling [75]. These authors reported that forces acting on the liquid vapor interface in microchannels correlated well with the critical heat flux, and that the scaling of these forces can provide a better understanding of important mechanism(s) at work. Figure 5-7a shows an idealized vapor bubble located in a micro channel, and Figure 5-7b indicates forces relevant to the removal of bubbles [76]. This approach has been shown to be in good agreement with observed experimental results for both water and low surface tension fluids [77].
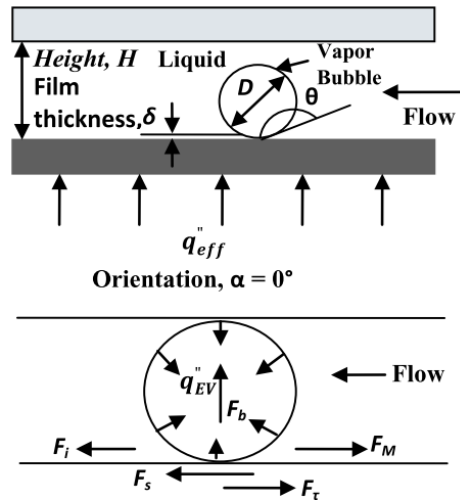
Figure 5-7 Forces acting on a liquid–vapor interface of a growing bubble in a microchannel cross-section (adapted from [81])

Since the relative magnitude of forces is important for determining the mechanism underlying the phenomenon, scaling analysis was normalized over the relative area over which it was acting.

- Buoyancy force, F_{boy}, per unit area is expressed as

$$P_{boy.} \equiv \frac{F_{boy.}}{A_{c,b}} = \frac{(\rho_v - \rho_l)\vec{g}V_b}{A_{c,b}} \approx (\rho_v - \rho_l)\vec{g}d_b$$

72

where V is volume, A_c, is cross sectional area, ρ, is density, and $\vec{g}$ is gravitation acceleration. Subscripts, v, l, and b, refer to vapor properties, liquid properties, and the bubble, respectively. d_b, is approximated by the capillary length, $\delta_c = \sqrt{\sigma/\rho_l \vec{g}}$ of the working fluid.

- Evaporation momentum force per unit area is expressed as

$$P_M \equiv \frac{F_M}{A_i} = \frac{\left(\frac{q''}{h_{lv}}\right)^2 \frac{1}{\rho_v} A_i}{A_i} \approx \left(\frac{q''}{h_{lv}}\right)^2 \frac{1}{\rho_v}$$

where q'' is a representative value of heat flux, 300 W/cm^2, h_{lv}, is the latent heat of vaporization. A_i, cancels out, but is the relevant area near the contact line - the microlayer area under the bubble. For calling purposes, this could also be the capillary length.

- Shear force per unit area is expressed as

$$P_\tau \equiv \frac{F_\tau}{A_c} = \frac{\left(\frac{\mu_l \vec{u}}{d_b} A_{pl}\right)}{A_c} \approx (\rho_v - \rho_l)\vec{g} \cos \varphi\, d_b$$

Where μ_l is the kinmatic viscosity of the liquid.

- Inertia force per unit area is expressed as

$$P_i \equiv \frac{F_i}{(D_H)^2} = \frac{\left(\frac{q''}{h_{lv}}\right)^2 \frac{1}{\rho_v} A_i}{A_i} \approx \left(\frac{q''}{h_{lv}}\right)^2 \frac{1}{\rho_v}$$

and finally,

- Surface tension force per unit area is expressed as

$$P_\sigma \approx \frac{\sigma \cos \theta}{l_c} \sim \frac{\sigma}{l_c}$$

where l_c is the characteristic pore size, which can be approximated by the spacing between pillars.

Figure 5-8 summarizes the scaling of area normalized forces for each of the three working fluids. Only the capillary force, shown as black curves, varied significantly due to wick geometry. The inertial force is shown over a range (in green), due to the three different mass flow rates tested: 200, 300, and 600 kg/m^{2}s. The key argument to be made from this analysis is that for water, the dominant force was capillarity, independent of the micropillar wick geometries or flow conditions being tested. It is important to note that HFE 7000, with the lowest surface tension, had no significant behavior from capillarity. Methanol showed some parity between the two largest forces - capillary and inertial, in the densely packed pillar array. Data

from the sparser pillar array appeared to indicate that any capillary benefits from micropillar wicks disappeared as the characteristic pore size neared 7-8 µm.
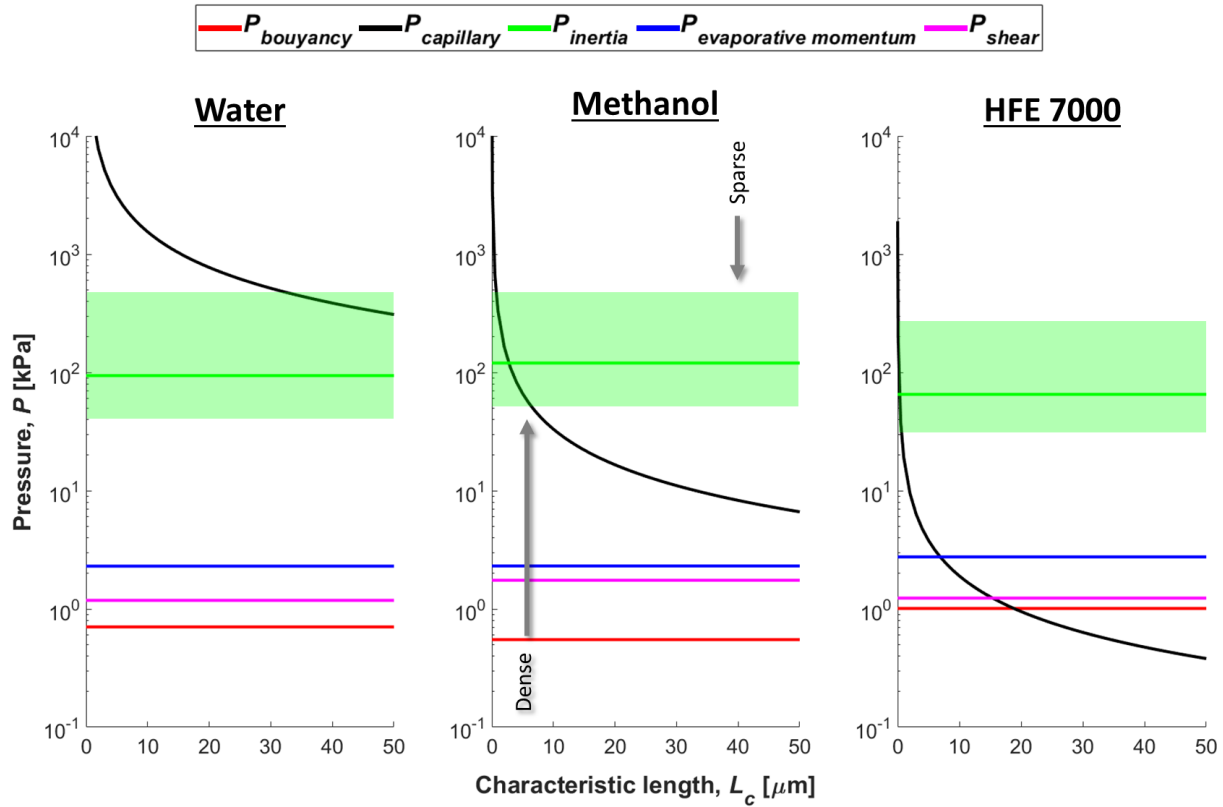
Figure 5-8 Magnitudes of major forces in microchannel compared to surface tension forces generated by a range of characteristic lengths.

5.4.2   Extended surface area

Capillary forces generated by different geometries of micropillar wick structures can influence the flow boiling behavior differently for the three operating liquids. Another explanation for any enhancement to the flow boiling behavior may be due to the extended area of different micropillars, since micropillars are essentially an array of fins that can improve the convective heat transfer to the fluid from the wall. To asses this, the fin effectiveness, ε_f, of smooth and micropillar surfaces were approximated. This value is the ratio of the heat removed from an extended surface area, divided by the heat removed from the same surface if it was planar, with the same driving potential (temperature difference). This analysis assumes: 1) 1-D heat

conduction, 2) no constriction resistance, 3) the high temperature is a set value at the backside of the device, 4) the low temperature is the saturation temperature of the working fluid, 5) and equivalent resistor can be defined for all the thermal resistances that exist in a smooth configuration as well as in a structured configuration, and 6) there is a heat transfer coefficient that is independent of material properties, except for thermal conductivity and is of uniform value—from the flat surface adjacent to the base of the pillars to the circumferential area on each cylinder/pillar.

The heat leaving the smooth surface was modeled as a conduction resistance through the silicon substrate, and a convection resistance to the working fluid in series, with the same area, and expressed as:

$$Q_{smooth} = \frac{\bar{h}k_{Si}WL}{\bar{h}t_{Si} + k_{Si}}(T_{heater} - T_\infty)$$

The structured sample can be modeled with a similar conduction resistance through the silicon substrate, except that its thickness is decreased by the height of the micropillars. In series after the substrate resistance, there were two parallel resistors: 1) a convection resistance from the flat bottom of the wick array to the working fluid, and 2) a conduction convection resistance that represents the array of silicon micropillars. This latter value can be taken as N_f individual pillars in parallel. The N_f is the total base area divided by the pitch squared for the square array of micropillars. Individual fin resistances, R_{fin}, expressed below as a function of m, the fin parameter, and can be calculated from first principles for a constant cross-section, extended area with a finite length, and an adiabatic tip boundary condition, which uses a corrected length, h_c, (which in this case is a corrected pillar height) to be able to model it as adiabatic at its tip. Shown below are schematic representation for the heat traveling through the smooth configuration (Figure 5-11a) and a micropillar array surface (Figure 5-11b), and their equivalent thermal resistor networks.

$$R_{fin} = \frac{1}{kA_c m \tanh mh_c} = \frac{1}{\sqrt{\bar{h}PkA_c} \tanh mh_c}$$

$$R_{finned.Surf} = N_f \parallel R_{fin} = \dfrac{2}{\pi N_f \sqrt{\overline{h} k_{Si} d^3} \, \tanh\left(\sqrt{\dfrac{4\overline{h}}{k_{Si} d}} \, h_c\right)}$$
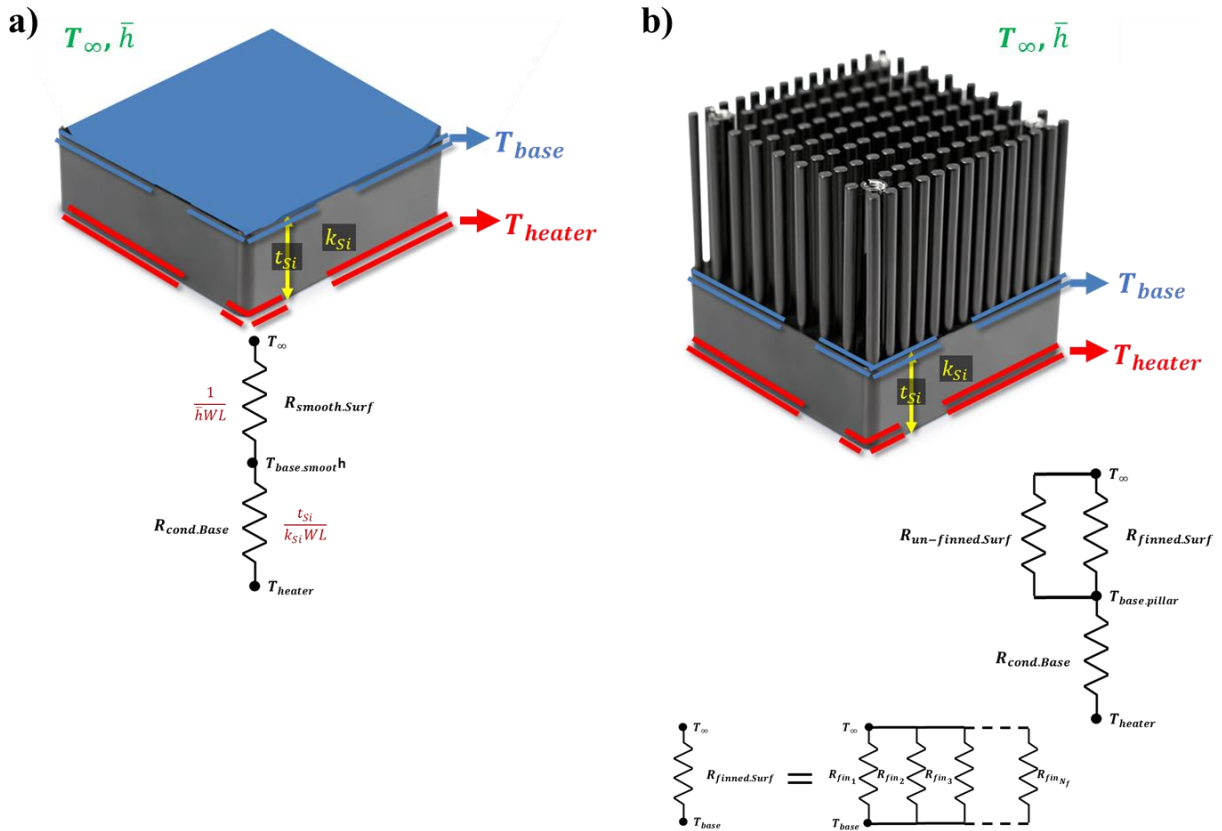
Figure 5-9   Schematic and corresponding thermal resistor network for a 1-D extended surface conduction model for (a) smooth samples, (b) microstructured samples.

As a conservative estimate, the uniform average heat transfer coefficient used in this analysis was $\overline{h} = k_{HFE700}/20$ μm. This represents an equivalent thermal resistor, using a quiescent working fluid that has the lowest conductivity to which the fin dissipates heat, and is a conservative limit. For each geometric configuration, the minimum fin effectiveness has been provided in Table 5-2. Any value over 1, indicates that there is an extended area enhancement for heat dissipation. All geometries listed show such an enhancement, indicating performance changes cannot be explained by extended surfaces alone.

Table 5-1   Fin effectiveness from 1-D conduction model

	$\varepsilon_f = \dfrac{Q_{finned}}{Q_{smooth}}$
Short-dense	3.29
Short-sparse	1.39
Tall-dense	5.03
Tall-sparse	1.96

Chapter 6- Summary and Future Work

6.1 Summary of thesis findings

Microchannel flow boiling has been limited by instabilities that can be successfully mitigated by the addition of surface microstructures (surface modifications), and by using a liquid coolant such as water. Structural modifications of microchannels are thought to contribute to heat flux. The critical heat flux during the flow boiling of water is positively correlated with the capillary-limited thin-film dry-out heat flux. Because water can adequately function only within a limited temperature range, in many microelectronic applications it may not be the ideal fluid for microchannel flow boiling, e.g. in aerospace engineering. Alternatives to water as a working fluid include methanol and hydrofluoroethers such as HFE 7000, an environmental-friendly dielectric fluid. In the present study, thermohydraulic changes from specific surface microstructural changes on intrachip flow boiling were investigated using lower surface tension working fluids (methanol, HFE 7000).

Fabrication of smooth and structured microchannels: Microchannels were fabricated with or without micropillars of two different heights (25 and 75 µm) and two different cylindrical pillar solid fractions (~ 5% and 20%) on the heated bottom wall of silicon test samples. Additional microchannel samples with 75 µm tall pillars or a smooth equivalent were fabricated in a 5 parallel channel configuration.

A custom flow loop for testing flow boiling of multiple working fluids over a range of operating pressures, was designed, constructed, and assembled. Since flow dynamics of two-phase microchannels is tightly coupled with other components, care was taken to ensure instabilities resulting from other components, such as compressibility within the flow loop, were eliminated or minimized. Degassing and preheating of the working fluid was carefully controlled to ensure near saturated fluid entered the microchannel, and that there was no upstream nucleation which could influence flow behavior within the device.

Heat flux in structured vs. smooth surface microchannels: Using methanol as the cooling fluid, in structured microchannels a maximum CHF of 494 W/cm^2 was achieved that was 61% greater than in smooth surface. The presence of micropillars reduced HTC or resulted in no significant change at lower exit quality conditions. Heat dissipation approaching 500 W/cm^2 at a calculated wall superheat of less than 20 K during flow boiling of methanol in microstructured channels, was achieved which suggests that this can be a promising cooling strategy for high power-density electronic systems operating in challenging environments.

Flow boiling in structured microchannel with HFE 7000: HFE 7000 showed minimal to no changes in flow boiling behavior. Only at the lower heat fluxes was any change noticed in the boiling curve, and this was possibly attributed to nucleation on a rougher surface. HTC for majority of boiling curves including up through CHF were identical. Though there was no thermal performance change, behaviorally the presence of micropillars did retain HFE 7000 to some degree, but most of the working fluid still operated in an inverted annular flow. Analysis across working fluids suggests that forces acting on the liquid-vapor interface in microchannels correlates well with critical heat flux, and scaling of these forces contribute to hydrodynamic instabilities. Experimental flow boiling behaviors near CHF were compared for water, methanol, and HFE 7000. As surface tension decreased, the effectiveness of micropillar wicks in preventing the rupture and removal of annular films was reduced. For water, the dominant force was capillarity, independent of the micropillar wick geometries or flow conditions being tested. HFE 7000, with the lowest surface tension, had no significant measured change due to capillarity. Methanol showed some parity between the two largest forces - capillary and inertial, and showed enhancement from capillarity at low mass fluxes. Enhancement disappeared at higher mass flow rates.

6.2　Future Directions

6.2.1　Improved visualization

Understanding the location of liquid- vapor interface needs to be critically examined. Current visualizations were made perpendicular to the heated floor/micropillar array. This projected view can leave a lot of questions as to the nature of the liquid film and/or droplets. Of greatest importance is understanding the wetting behavior. Shown below in Figure 6-1 are liquid droplet in i. Cassie state, ii. Wenzel state, or iii. a hybrid state—a combination of both.
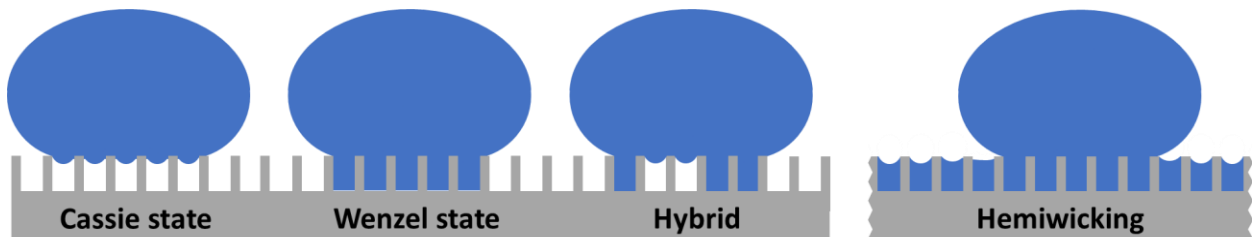
Figure 6-1　Various wetting states on structured surfaces.

Although wetting behavior can be inferred, more accurate alternatives could help in better understanding the thermal hydraulic characterization. One such strategy could involve using IR imaging from the heater side of the device. The presence of working fluid adjacent to the pillar/smooth surface wall could be easily visualized with this approach. Silicon is IR transparent, and all three working fluids used in this dissertation are transparent in the gaseous phase, especially when compared to the liquid phase. Therefore, when vapor is adjacent to the wall, IR imaging would show a cooler surface since the image would capture the temperature of the liquid-vapor interface on the other side of the bubble. The outside of the regime affected by onset of nucleate boiling would be cooler than the heated wall/microchannel heat source temperature. This technique has been used extensively by Kim, Park and Buongiorno [78]. A challenge for implementation is the heater material. In the current study platinum was used. For IR imaging through/past

the heater, the material used must be transparent. One such material would be indium tin oxide (ITO) [78]. Future studies could use indium tin oxide heaters.

6.2.2   Proposed mechanism

Visual observations of micropillar flow boiling of methanol and HFE 7000 showed liquid regions to be wetting the pillar arrays, translating in the downstream direction. The meniscus depinning as the tailend receded, seemed to progress pillar to pillar and at times revealed a secondary meniscus connecting a pillar to the silicon base floor. Based on these observations, the assumption is that liquid slugs are in the Wenzel state. A mechanism of the dryout process is proposed. This is shown schematically in Figure 6-2. The liquid slug translating among the pillar array displays an inverse relationship between translating slug velocity, $\overline{U_{LS}}$, and the heat flux. Modeling the forces acting on these slugs may help in predicting the critical heat flux within these pillar arrays. The forces will dictate the velocity with which the slug can travel through the pillars.
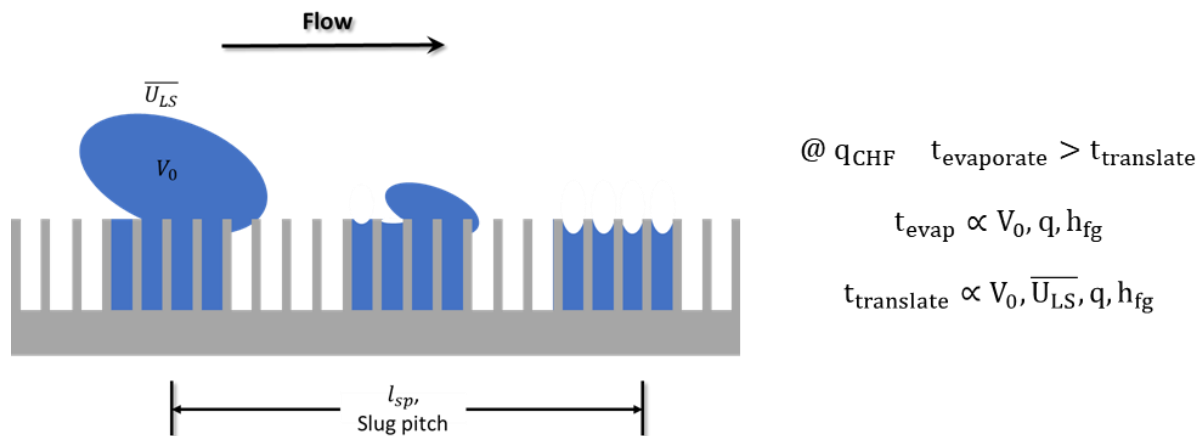
Figure 6-2   Schematic of a translating liquid slug evaporating in the Wenzel state and flow conditions at CHF for this proposed model.

One proposal for CHF is that the time needed to advance the liquid slug, $t_{translate}$, a finite distance, such as the pillar pitch, l, will be greater than the time needed to evaporate the volume of liquid that would be traversing that distance. This model can conceivably incorporate all thermophysical material properties by

carefully defining each force acting on the liquid slug, thereby propelling it, and the shape the liquid slug takes. This model can be tested experimentally using a test section that allows for a finite volume of working fluid to be introduced and then propelled along by shear forces from the gas phase and possibly from non-uniformity in the evaporative momentum force due to contact angle hysteresis. Information obtained from measuring the dryout length as a function of original liquid volume and average heat flux will provide support of the proposed mechanism.

6.2.3   Length scale for very low surface tension fluids

Finally, even though no significant enhancement was found for microstructured microchannels with HFE 7000, the fluid with the lowest surface tension in this study, the conclusion only holds to the geometries investigated here which were in the high single digit micron or higher. Scale analysis indicates that for HFE 7000, submicron length scale capillary structures should be used for capillary dominated flow boiling behavior. Though this approach needs investigated, the long erm commercialization/application of these length scales is suspect. HFE 7000 and other hydroflouroethers are solvents capable of dissolving a vast number of impurities/contaminants, and is used as a cleaning agent for that purpose in the airline industry. For phase change applications, liquids such as HFE 7000 evaporation/boiling from fine scale structures in the nanometer realm, as prescribed for effect capillary driven operation, would be subject to fouling and performance degradation.

References

[1]   A. Bar-Cohen and P. Wang, "Thermal Management of On-Chip Hot Spot," *J. Heat Transfer*, vol. 134, no. 5, p. 051017, 2012.

[2]   P. Ruch, T. Brunschwiler, W. Escher, S. Paredes, and B. Michel, "Toward five-dimensional scaling: How density improves efficiency in future computers," *IBM J. Res. Dev.*, vol. 55, no. 5, pp. 15:1-15:13, 2011.

[3]   J. G. Kassakian and T. M. Jahns, "Evolving and Emerging Applications of Power Electronics in Systems," *IEEE J. Emerg. Sel. Top. Power Electron.*, vol. 1, no. 2, pp. 47–58, 2013.

[4]   K. Joshin, T. Kikkawa, S. Masuda, and K. Watanabe, "Outlook for GaN HEMT Technology," *Fujitsu Sci. Tech. J.*, vol. 50, no. 1, pp. 138–143, 2014.

[5]   Y. Won, J. Cho, D. Agonafer, M. Asheghi, and K. E. Goodson, "Fundamental Cooling Limits for High Power Density Gallium Nitride Electronics," in *IEEE Transactions On Components, Packaging And Manufacturing Technology,* 2015, vol. 5, no. 6, pp. 1–8.

[6]   K. R. Bagnall, O. I. Saadat, T. Palacios, and E. N. Wang, "Analytical thermal model for HEMTs with complex epitaxial structures," *Fourteenth Intersoc. Conf. Therm. Thermomechanical Phenom. Electron. Syst.*, vol. 2, pp. 947–958, 2014.

[7]   H. Chiueh, J. Draper, and J. Choma, "A Dynamic Thermal Management Circuit for System-On-Chip Designs ∗," pp. 175–181, 2003.

[8]   A. Bar-Cohen, "Broad Agency Announcement: Intrachip/Interchip Enhanced Cooling Fundamentals," 2012.

[9]   P. Ruch, T. Brunschwiler, S. Paredes, I. Meijer, and B. Michel, "Roadmap towards Ultimately-Efficient Zeta-Scale Datacenters," in *Design, Automation & Test in Europe Conference & Exhibition (DATE), 2013*, 2013, pp. 1339–1344.

[10]   T. M. Harms, M. J. Kazmierczak, and F. M. Gerner, "Developing convective heat transfer in deep rectangular microchannels," *Int. J. Heat Fluid Flow*, vol. 20, no. 2, pp. 149–157, Apr. 1999.

[11]   M. A. Ebadian and C. X. Lin, "A Review of High-Heat-Flux Heat Removal Technologies," *J. Heat Transfer*, vol. 133, no. 11, p. 110801, 2011.

[12]   D. Liu and S. V. Garimella, "Analysis and optimization of the thermal performance of microchannel heat sinks," *Int. J. Numer. Methods Heat Fluid Flow*, vol. 15, no. 1, pp. 7–26, 2005.

[13]   J. B. Marcinichen, B. P. D'Entremont, J. R. Thome, G. Bulman, J. Lewis, and R. Venkatasubramanian, "Thermal management of ultra intense hot spots with two-phase multi-microchannels and embedded thermoelectric cooling," in *ASME 2013 International Technical Conference and Exhibition on Packaging and Integration of Electronic and Photonic Microsystems InterPACK2013*, 2013.

[14]   Z. Wu and B. Sundén, "On further enhancement of single-phase and flow boiling heat transfer in micro/minichannels," *Renew. Sustain. Energy Rev.*, vol. 40, pp. 11–27, 2014.

[15]   Y. Wang and Z. Wang, "An overview of liquid–vapor phase change, flow and heat transfer in

mini- and micro-channels," *Int. J. Therm. Sci.*, vol. 86, pp. 227–245, Dec. 2014.

[16]   M. E. Steinke and S. G. Kandlikar, "An experimental investigation of flow boiling characteristics of water in parallel microchannels," *J. Heat Transf. Asme*, vol. 126, no. 4, pp. 518–526, 2004.

[17]   P.-S. Lee and S. V. Garimella, "Saturated flow boiling heat transfer and pressure drop in silicon microchannel arrays," *Int. J. Heat Mass Transf.*, vol. 51, no. 3–4, pp. 789–806, 2008.

[18]   J. Lee and I. Mudawar, "Two-phase flow in high-heat-flux micro-channel heat sink for refrigeration cooling applications: Part II - Heat transfer characteristics," *Int. J. Heat Mass Transf.*, vol. 48, no. 5, pp. 941–955, 2005.

[19]   C. Buffone and K. Sefiane, "Investigation of thermocapillary convective patterns and their role in the enhancement of evaporation from pores," *Int. J. Multiph. Flow*, vol. 30, no. 9, pp. 1071–1091, 2004.

[20]   J. L. Plawsky *et al.*, "Nano- and Microstructures for Thin-Film Evaporation—A Review," *Nanoscale Microscale Thermophys. Eng.*, vol. 18, no. 3, pp. 251–269, 2014.

[21]   H. Wang, S. V. Garimella, and J. Y. Murthy, "Characteristics of an evaporating thin film in a microchannel," *Int. J. Heat Mass Transf.*, vol. 50, no. 19–20, pp. 3933–3942, Sep. 2007.

[22]   T. Brunschwiler *et al.*, "Embedded power insert enabling dual-side cooling of microprocessors," in *2015 IEEE 65th Electronic Components and Technology Conference (ECTC)*, 2015, pp. 833–838.

[23]   C. Choi, J. S. Shin, D. I. Yu, and M. H. Kim, "Flow boiling behaviors in hydrophilic and hydrophobic microchannels," *Exp. Therm. Fluid Sci.*, vol. 35, no. 5, pp. 816–824, 2011.

[24]   Z. Edel and A. Mukherjee, "Flow Boiling Dynamics of Water and Nanofluids in a Single microchannel at different heat fluxes," in *ASME 2013 Heat Transfer Summer Conference*, 2013.

[25]   V. V Kuznetsov and A. S. Shamirzaev, "Flow boiling heat transfer of water in microchannel heat sink," *J. Eng. Thermophys.*, vol. 21, no. 1, pp. 28–35, 2012.

[26]   G. Hetsroni, "Boiling in micro-channels," *Bull. Polish Acad. Sci. Tech. Sci.*, vol. 58, no. 1, pp. 155–163, 2010.

[27]   D. Li *et al.*, "Enhancing Flow Boiling Heat Transfer in Microchannels for Thermal Management with Monolithically-Integrated Silicon Nanowires," 2012.

[28]   Q. Li *et al.*, "Enhanced pool boiling performance on micro-, Nano-, and hybrid-structured surfaces," in *ASME 2011 International Mechanical Engineering Congress and Exposition, IMECE 2011*, 2011, vol. 10, no. PARTS A AND B, pp. 633–640.

[29]   Y. Zhu *et al.*, "Surface Structure Enhanced Microchannel Flow Boiling," *J. Heat Transfer*, vol. 138, no. September, pp. 1–13, May 2016.

[30]   A. E. Bergles and S. G. Kandlikar, "On the Nature of Critical Heat Flux in Microchannels," *J. Heat Transfer*, vol. 127, no. 1, p. 101, Jan. 2005.

[31]   S. G. Kandlikar, "Fundamental issues related to flow boiling in minichannels and microchannels," *Exp. Therm. Fluid Sci.*, vol. 26, no. 2–4, pp. 389–407, 2002.

[32]   S. G. Kandlikar, "History, Advances, and Challenges in Liquid Flow and Flow Boiling Heat Transfer in Microchannels: A Critical Review," *J. Heat Transfer*, vol. 134, no. 3, p. 034001, Mar. 2012.

[33]   S. G. Kandlikar *et al.*, "Heat Transfer in Microchannels—2012 Status and Research Needs," *J. Heat Transfer*, vol. 135, no. 9, p. 091001, Jul. 2013.

[34]   A. Koşar, C.-J. Kuo, and Y. Peles, "Suppression of Boiling Flow Oscillations in Parallel Microchannels by Inlet Restrictors," *J. Heat Transfer*, vol. 128, no. 3, p. 251, Mar. 2006.

[35]   C. T. Lu and C. Pan, "Convective boiling in a parallel microchannel heat sink with a diverging cross section and artificial nucleation sites," *Exp. Therm. Fluid Sci.*, vol. 35, no. 5, pp. 810–815, Jul. 2011.

[36]   M. J. Miner, P. E. Phelan, B. A. Odom, and C. A. Ortiz, "Experimental Measurements of Critical Heat Flux in Expanding Microchannel Arrays," *J. Heat Transfer*, vol. 135, no. 10, p. 101501, Aug. 2013.

[37]   M. J. Miner, P. E. Phelan, B. A. Odom, and C. A. Ortiz, "An Experimental Investigation of Pressure Drop in Expanding Microchannel Arrays," *J. Heat Transfer*, vol. 136, no. 3, p. 031502, Nov. 2013.

[38]   A. Mukherjee and S. G. Kandlikar, "The effect of inlet constriction on bubble growth during flow boiling in microchannels," *Int. J. Heat Mass Transf.*, vol. 52, no. 21–22, pp. 5204–5212, Oct. 2009.

[39]   Lian Zhang *et al.*, "Enhanced nucleate boiling in microchannels," in *Technical Digest. MEMS 2002 IEEE International Conference. Fifteenth IEEE International Conference on Micro Electro Mechanical Systems (Cat. No.02CH37266)*, pp. 89–92.

[40]   L. Zhang, E. N. Wang, K. E. Goodson, and T. W. Kenny, "Phase change phenomena in silicon microchannels," *Int. J. Heat Mass Transf.*, vol. 48, no. 8, pp. 1572–1582, Apr. 2005.

[41]   A. Koşar, C.-J. Kuo, and Y. Peles, "Boiling heat transfer in rectangular microchannels with reentrant cavities," *Int. J. Heat Mass Transf.*, vol. 48, no. 23–24, pp. 4867–4886, Nov. 2005.

[42]   C.-J. Kuo and Y. Peles, "Flow Boiling Instabilities in Microchannels and Means for Mitigation by Reentrant Cavities," *J. Heat Transfer*, vol. 130, no. 7, p. 072402, Jul. 2008.

[43]   B. R. Alexander and E. N. Wang, "Design of a Microbreather for Two-Phase Microchannel Heat Sinks," *Nanoscale Microscale Thermophys. Eng.*, vol. 13, no. 3, pp. 151–164, Jul. 2009.

[44]   M. P. David, J. E. Steinbrenner, J. Miler, and K. E. Goodson, "Adiabatic and diabatic two-phase venting flow in a microchannel," *Int. J. Multiph. Flow*, vol. 37, no. 9, pp. 1135–1146, Nov. 2011.

[45]   F. Yang, X. Dai, Y. Peles, P. Cheng, J. Khan, and C. Li, "Flow boiling phenomena in a single annular flow regime in microchannels (II): Reduced pressure drop and enhanced critical heat flux," *Int. J. Heat Mass Transf.*, vol. 68, pp. 716–724, Jan. 2014.

[46]   F. Yang, X. Dai, Y. Peles, P. Cheng, J. Khan, and C. Li, "Flow boiling phenomena in a single annular flow regime in microchannels (I): Characterization of flow boiling heat transfer," *Int. J. Heat Mass Transf.*, vol. 68, pp. 703–715, Jan. 2014.

[47]   F. Yang, X. Dai, C.-J. Kuo, Y. Peles, J. Khan, and C. Li, "Enhanced flow boiling in microchannels

by self-sustained high frequency two-phase oscillations," *Int. J. Heat Mass Transf.*, vol. 58, no. 1–2, pp. 402–412, Mar. 2013.

[48]   S. Shin, G. Choi, B. S. Kim, and H. H. Cho, "Flow boiling heat transfer on nanowire-coated surfaces with highly wetting liquid," *Energy*, vol. 76, pp. 428–435, Nov. 2014.

[49]   S. S. Kim, T. S. Fisher, and J. A. Weibel, "Thermal Performance of Carbon Nanotube Enhanced Vapor Chamber Wicks," in *14th International Heat Transfer Conference*, 2010, pp. 1–8.

[50]   C. Ding, G. Soni, P. Bozorgi, B. D. Piorek, C. D. Meinhart, and N. C. MacDonald, "A flat heat pipe architecture based on nanostructured titania," *J. Microelectromechanical Syst.*, vol. 19, no. 4, pp. 878–884, 2010.

[51]   S. Adera, R. Raj, and E. N. Wang, "Capillary-limited evaporation from well-defined microstructured surfaces," in *ASME 2013 4th International Conference on Micro/Nanoscale Heat and Mass Transfer, MNHMT 2013*, 2013.

[52]   Y. Nam, S. Sharratt, G. Cha, and Y. S. Ju, "Characterization and Modeling of the Heat Transfer Performance of Nanostructured Cu Micropost Wicks," *J. Heat Transfer*, vol. 133, no. 10, p. 101502, 2011.

[53]   G. S. Hwang, Y. Nam, E. Fleming, P. Dussinger, Y. S. Ju, and M. Kaviany, "Multi-artery heat pipe spreader: Experiment," *Int. J. Heat Mass Transf.*, vol. 53, no. 13–14, pp. 2662–2669, 2010.

[54]   D. Ćoso, V. Srinivasan, M.-C. Lu, J.-Y. Chang, and A. Majumdar, "Enhanced Heat Transfer in Biporous Wicks in the Thin Liquid Film Evaporation and Boiling Regimes," *J. Heat Transfer*, vol. 134, no. 10, p. 101501, 2012.

[55]   Q. Cai and C.-L. Chen, "Design and Test of Carbon Nanotube Biwick Structure for High-Heat-Flux Phase Change Heat Transfer," *J. Heat Transfer*, vol. 132, no. 5, p. 52403, 2010.

[56]   K. K. Bodla, J. a Weibel, and S. V Garimella, "Advances in Fluid and Thermal Transport Property Analysis and Design of Sintered Porous Wick Microstructures," *J. Heat Transfer*, vol. 135, no. June, p. 61202, 2013.

[57]   B. Daniels, J. a. Liburdy, and D. V. Pence, "Adiabatic Flow Boiling in Fractal-Like Microchannels," *Heat Transf. Eng.*, vol. 28, no. 10, pp. 817–825, 2007.

[58]   A. Tulchinsky, D. V Pence, and J. A. Liburdy, "Spray cooling heat transfer enhancement and degradation using fractal-like micro-structured surfaces," *ASME/JSME 8th Therm. Eng. Jt. Conf.*, pp. 1–9, 2011.

[59]   T. Semenic and I. Catton, "Experimental study of biporous wicks for high heat flux applications," *Int. J. Heat Mass Transf.*, vol. 52, no. 21–22, pp. 5113–5121, 2009.

[60]   Y. K. Prajapati and P. Bhandari, "Flow boiling instabilities in microchannels and their promising solutions – A review," *Exp. Therm. Fluid Sci.*, vol. 88, pp. 576–593, 2017.

[61]   Y. K. Prajapati, M. Pathak, and M. K. Khan, "Bubble dynamics and flow boiling characteristics in three different microchannel configurations," *Int. J. Therm. Sci.*, vol. 112, 2017.

[62]   R. Xiao, R. Enright, and E. N. Wang, "Prediction and Optimization of Liquid Propagation in Micropillar Arrays," *Langmuir*, vol. 26, no. 19, pp. 15070–15075, Oct. 2010.

[63]   F. Yang, W. Li, X. Dai, and C. Li, "Flow boiling heat transfer of HFE-7000 in nanowire-coated microchannels," *Appl. Therm. Eng.*, vol. 93, pp. 260–268, 2016.

[64]   Y. Zhu, Zhengmao Lu, D. S. Antao, Hongxia Li, T. Zhang, and E. N. Wang, "Model optimization of dry-out heat flux from micropillar wick structures," in *2016 15th IEEE Intersociety Conference on Thermal and Thermomechanical Phenomena in Electronic Systems (ITherm)*, 2016, pp. 372–377.

[65]   S. Adera, D. Antao, R. Raj, and E. N. Wang, "Design of micropillar wicks for thin-film evaporation," *Int. J. Heat Mass Transf.*, vol. 101, pp. 280–294, Oct. 2016.

[66]   A. S. Sangani and A. Acrivos, "Slow flow past periodic arrays of cylinders with application to heat transfer," *Int. J. Multiph. Flow*, vol. 8, no. 3, pp. 193–206, Jun. 1982.

[67]   W. Hayduk and H. Laudie, "Solubilities of gases in water and other associated solvents," *AIChE J.*, vol. 19, no. 6, pp. 1233–1238, Nov. 1973.

[68]   M. Arik, A. Koşar, H. Bostanci, and A. Bar-Cohen, "Pool boiling critical heat flux in dielectric liquids and nanofluids," in *Advances in Heat Transfer*, vol. 43, Academic Press, 2011, pp. 1–76.

[69]   S. M. Ghiaasiaan, "Transition and Film Boiling," in *Handbook of Thermal Science and Engineering*, Springer International Publishing, 2017, pp. 1–51.

[70]   J. Kim, "Review of nucleate pool boiling bubble heat transfer mechanisms," *International Journal of Multiphase Flow*, vol. 35, no. 12. Pergamon, pp. 1067–1076, 01-Dec-2009.

[71]   G. Liang and I. Mudawar, "Pool boiling critical heat flux (CHF) – Part 1: Review of mechanisms, models, and correlations," *International Journal of Heat and Mass Transfer*, vol. 117. Elsevier Ltd, pp. 1352–1367, 01-Feb-2018.

[72]   J. H. Lienhard and L. C. Witte, "An historical review of the hydrodynamic theory of boiling," *Rev. Chem. Eng.*, vol. 3, no. 3–4, pp. 187–280, Dec. 1985.

[73]   S. G. Kandlikar, "A theoretical model to predict pool boiling CHF incorporating effects of contact angle and orientation," *J. Heat Transfer*, vol. 123, no. 6, pp. 1071–1079, Dec. 2001.

[74]   R. P. Rioux, E. C. Nolan, and C. H. Li, "A systematic study of pool boiling heat transfer on structured porous surfaces: From nanoscale through microscale to macroscale," *AIP Adv.*, vol. 4, no. 11, p. 117133, Nov. 2014.

[75]   S. G. Kandlikar, "Heat transfer mechanisms during flow boiling in microchannels," *J. Heat Transfer*, vol. 126, no. 1, pp. 8–16, 2004.

[76]   S. G. Kandlikar, "Scale effects on flow boiling heat transfer in microchannels: A fundamental perspective," *Int. J. Therm. Sci.*, vol. 49, no. 7, pp. 1073–1085, Jul. 2010.

[77]   T. Alam and P.-S. Lee, "Flow Boiling Instabilities in Expanding Microgap Channel," Springer, Cham, 2017, pp. 27–46.

[78]   H. Kim, Y. Park, and J. Buongiorno, "Measurement of wetted area fraction in subcooled pool boiling of water using infrared thermography," *Nucl. Eng. Des.*, vol. 264, pp. 103–110, Nov. 2013.

[79]   Y. Zhu, D. S. Antao, Z. Lu, S. Somasundaram, T. Zhang, and E. N. Wang, "Prediction and Characterization of Dry-out Heat Flux in Micropillar Wick Structures," *Langmuir*, vol. 32, no. 7,

pp. 1920–1927, Feb. 2016.

[80]   J. Lee and I. Mudawar, "Critical heat flux for subcooled flow boiling in micro-channel heat sinks," *Int. J. Heat Mass Transf.*, vol. 52, no. 13–14, pp. 3341–3352, Jun. 2009.

[81]   T. Alam *et al.*, "Force analysis and bubble dynamics during flow boiling in silicon nanowire microchannels," *Int. J. Heat Mass Transf.*, vol. 101, pp. 915–926, 2016.